Design and Implementation of Declarative Crop Modeling Framework

Kyungdahm Yun

A dissertation
submitted in partial fulfillment of the
requirements for the degree of

Doctor of Philosophy

University of Washington

2021

Reading Committee:
Soo-Hyung Kim, Chair
Elizabeth Van Volkenburgh
David H. Fleisher

Program Authorized to Offer Degree:
School of Environmental and Forest Sciences

University of Washington

Abstract

Design and Implementation of Declarative Crop Modeling Framework

Kyungdahm Yun

Chair of the Supervisory Committee:
Dr. Soo-Hyung Kim
School of Environmental and Forest Sciences

Crop modeling is a process of translating quantitative knowledge on crop growth into a computer program that simulates the growth *in silico*. From a software engineering perspective, crop modeling has suffered from a legacy built decades ago when early crop models appeared. Many crop models have been developed in imperative programming approaches striving for high performance, but frequently suffered from error-prone code and technical debts left behind. In this study, we propose a new declarative modeling framework named Cropbox written in Julia programming language to support developing crop models in a concise form equipped with useful abstractions commonly required in modeling. With an insight that a crop model is essentially an integrated network of generalized state variables, the framework provides various primitives for representing variables and systems as well as functions essential to modeling workflow. The modeling workflow based on Cropbox was used to create and illustrate its applications in crop modeling at different levels of organization and complexity. The first application was phenology modeling for building an ensemble model to predict flowering time based on various existing approaches. Extracting common patterns in the models and developing reusable interface for simulation, visualization, and calibration motivated an idea of a new modeling framework. The second application was a coupled gas-exchange model which combines two models for biochemical photosynthesis and empirical stomatal conductance with an additional link to an energy balance equation. The model implemented in Cropbox framework provided the same functionality as an existing model written in C++ with less code and a more flexible interface in terms of parameter management and output visualization. To demonstrate the capability of the model, we evaluated two stomatal conductance modeling approaches and applied them to replicate the observed behavior of transgenic plants from the literature. The last application was a whole-plant crop simulation model for garlic (*Allium sativum*) translated from an existing C++ model aimed at simulating leaf development and growth. The new model was expanded and improved to simulate biomass and yield with an emphasis on whole-plant carbon budget. The model was evaluated with three datasets for analyzing effective planting dates as a climate adaptation strategy in South Korea under future climate conditions projected by different greenhouse gas emission scenarios. The Cropbox framework can support development of conventional crop models but also show potential for incorporating other approaches like functional-structural plant modeling (FSPM) as briefly illustrated by a 3D root structure growth model for switchgrass (*Panicum virgatum*). With a domain-specific language and unified interface specifically designed for crop modeling, the Cropbox framework will become a useful tool for research and teaching in this field.

TABLE OF CONTENTS

Page

List of Figures . . . iii

List of Tables . . . v

Chapter 1: Declarative Modeling Framework . . . 1
- 1.1 Introduction . . . 1
- 1.2 Design . . . 4
- 1.3 Applications . . . 22
- 1.4 Conclusions . . . 32

Bibliography . . . 33

Chapter 2: Application I: Phenology Model . . . 36
- 2.1 Introduction . . . 37
- 2.2 Materials and Methods . . . 39
- 2.3 Results . . . 52
- 2.4 Discussion . . . 61
- 2.5 Conclusions . . . 66

Bibliography . . . 67

Chapter 3: Application II: Coupled Gas-Exchange Model . . . 75
- 3.1 Introduction . . . 76
- 3.2 Materials and Methods . . . 78
- 3.3 Results . . . 98
- 3.4 Discussion . . . 108
- 3.5 Conclusions . . . 114

Bibliography 116

Chapter 4: Application III: Garlic Model 122
    4.1 Introduction 123
    4.2 Materials and Methods 125
    4.3 Results 132
    4.4 Discussion 142

Bibliography 147

LIST OF FIGURES

Figure Number Page

1.1 A fundamental concept of Cropbox modeling framework 5
1.2 An architecture of Cropbox modeling framework 6
1.3 Net photosynthesis rate of a C_4 leaf simulated by LeafGasExchange.jl . 23
1.4 Leaf development simulation for garlic by Garlic.jl 26
1.5 Rendering of 3D root structure by CropRootBox.jl for switchgrass 31

2.1 Overview of phenology model evaluation process 50
2.2 Observed vs. predicted flowering dates 53
2.3 Comparison of individual models 54
2.4 Comparison of individual and ensemble models 55
2.5 Comparison of ensemble models 57
2.6 Predicted full bloom dates of cherry in Washington, D.C. 58
2.7 Full bloom dates of Yoshino cherry projected under future climate scenarios . 59
2.8 Full bloom dates of Kwanzan cherry projected under future climate scenarios 60

3.1 System diagram of the gas-exchange model 87
3.2 Snippet of model code implementing energy balance process. 88
3.3 Script for running a coupled gas-exchange model 93
3.4 Script for calibrating parameters for the gas-exchange model 94
3.5 Script for generating Figure 3.9b 95
3.6 Fitting SPAD measurement to leaf nitrogen content 97
3.7 Evaluation of the gas-exchange model with two stomatal conductance submodels 99
3.8 Sensitivity of parameters related to nitrogen dependence 101
3.9 Stomatal conductance between BB and MED 102
3.10 Net photosynthesis rate between BB and MED over C_a 103
3.11 Net photosynthesis rate between BB and MED over T_a 104
3.12 Net photosynthesis rate by BB and MED under nitrogen or water stress . . . 106
3.13 Net photosynthesis rate by BB and MED under nitrogen and water stress . . 109

3.14 Gas-exchange simulation replicating Kubien et al. [2003] 115

4.1 Partitioning coefficients per development stage 127
4.2 Geographic locations of Gosan and Jeju in South Korea 132
4.3 Simulated green leaf area for dataset D1 133
4.4 Simulated biomass allocation for dataset D1 135
4.5 Simulated leaf development for dataset D1 136
4.6 Simulated green leaf area under two temperature zones 137
4.7 Simulated biomass allocation for dataset D3 138
4.8 Yield estimation for Gosan 139
4.9 Optimal planing dates estimated for Gosan and Chuncheon 140
4.10 Yield estimation for Chuncheon 141

LIST OF TABLES

Table Number Page

3.1 Variables declared in the coupled gas-exchange model. 88
3.2 Parameters and constants used in the coupled gas-exchange model. 91
3.3 Default environmental condition for the coupled gas-exchange model. 98
3.4 Variables and parameters for replicating experiment by Kubien et al. [2003]. 112

ACKNOWLEDGMENTS

I would like to express sincere appreciation to my supervisor Dr. Soo-Hyung Kim for his guidance and patience through a long journey of my graduate study. His experience and knowledge gave me a lot of motivation and inspiration not only for what I have done so far, but also what I'm planning to do in the next step. 'Cropbox' is indeed the name he came up with when we started brainstorming the idea of making a modern crop modeling framework.

I would also like to thank my committee members. Dr. Elizabeth Van Volkenburgh was always kind, but very critical about anything plant science. Dr. David Ford kept me thinking about the concept of modeling from the ground up. Dr. David Fleisher provided valuable feedback from his expertise in crop modeling. Dr. Jevin West encouraged me to continue working across computer science and biology as he had once done.

I am deeply grateful to the funding received from Korean Society of Agricultural and Forest Meteorology (KSAFM), Department of Energy (DOE) Advanced Research Projects Agency – Energy (ARPA-E), United States Department of Agriculture – Agricultural Research Service (USDA-ARS), and Rural Development Administration (RDA) in South Korea.

I would like to extend my sincere thanks to Dr. Kyung Hwan Moon for sharing his vision and passion on agricultural science. Finally, I shouldn't forget to mention Dr. Jin Il Yun who first introduced me to the world of computer a long time ago and ultimately led me to the field of crop modeling.

And my special thanks go to the current and former members as well as friends of Plant Modeling and Ecophysiology Lab: Hyungmin "Tony" Rho, Jennifer Hsiao, Johanna Cantillo, Marian Hsieh, Hannah Kinmonth-Schultz, Arthur Hsin-Wu Hsu, Man Marcaida III, M Stuke, Darshi Banan, Beomseok Seo, and Kiwoong "Samuel" Lee.

DEDICATION

to my beloved family
Hyunok and Yujun

Chapter 1

DECLARATIVE MODELING FRAMEWORK

Abstract

Crop modeling is a process of translating quantitative knowledge about crop growth into a computer program that simulates the growth *in silico*. Therefore crop modeling inherently becomes a software engineering problem. Many crop models have been developed in imperative programming approaches with high running performance, but then consequently suffered from error-prone code and technical debts left behind. In this study, we propose a new declarative modeling framework named Cropbox to support writing crop models in a concise form yet with little loss in generality. With an insight that a crop model is essentially an integrated network of generalized state variables, our framework provides various primitives for representing variables and systems as well as several functions essential to modeling workflow. We discuss the capability of the framework with practical applications commonly found in conventional crop modeling, such as a coupled leaf-gas exchange model and a whole-plant garlic growth model and also with a potential expansion to a functional-structural plant modeling (FSPM) approach demonstrated by a 3D root structure growth model.

1.1 Introduction

Crop modeling is inherently a software engineering process where the model which is a final outcome can be limited by various technical implications. Computer platforms and programming tools available at times have shown a strong influence on the development of crop models in history.

Early crop models from Wageningen University were developed on CSMP (Continuous

System Modeling Program) language which was a simulation language designed for continuous time domain where problems were represented by differential equations. CSMP was based on the idea of clear separation between groups of variables involved in numerical integration [Brennan and Silberberg, 1968, Caskie and Mason, 1972]. Rate variables represent changes of certain quantities during a small time step. State variables hold quantities at each time point integrated by the rate variables as integrands.

Once the language became obsolete with arrival of new computer platforms in the 1980s, an attempt to replace CSMP was conceived to continue development of crop models and FSE/FST came out as a result. FSE (Fortran Simulation Environment) was a framework equipped with domain-specific simulation features similar to CSMP on top of a general programming language emerging at the time called FORTRAN [van Kraalingen and de Vries, 1990, van Kraalingen, 1991, 1995]. FST (Fortran Simulation Translator) was a companion tool providing a transition layer for existing models written in CSMP syntax [Rappoldt and van Kraalingen, 1996, van Kraalingen et al., 2003]. Variables were still declared in separate sections in the code to distinguish rate and state variables. An order of calculation within the section was automatically determined by sorting out the dependency of variables involved. In addition to the model specification mainly describing a set of differential equations, modelers also needed means of running the models and evaluating the outcomes. For a complete simulation workflow, FSE/FST provided model driving statements in order to support setting up parameters, including time step and output format, and producing graphical plots. As a domain-specific simulation language implemented on Fortran, FSE/FST became widely adopted for developing varieties of crop models. For example, DSSAT (Decision Support System for Agrotechnology Transfer) was once ported FSE/FST framework and the internal model structure established at the time largely remains to date [Jones et al., 2003]. With the advent of recent technological shifts, FSE has also inspired new simulation frameworks implemented on different programming languages. PCSE (Python Crop Simulation Environment) was an attempt to reimplement existing crop models written for FSE in a dynamically typed language Python which could be more suitable for interactive simulation [de Wit et al., 2019]. WISS (Wageningen Integrated Systems Simulator) was a recently announced simulation framework developed in Java language with a similar objective in mind [van Kraalingen et al., 2020].

System dynamics is an approach to understand emergent behavior of complex systems by linking simple primitives like stock and flow [Forrester, 1961]. Mathematically, a system dynamics model consists of a set of differential equations similarly to continuous system simulation languages. Stock, or originally called level, represents a quantity accumulated or integrated over time. Flow represents a change of stock per time which is essentially the same concept as the rate variable described above. Incoming flow and outgoing flow are explicitly identified as separate entities to clearly show interactions between variables. System dynamics models can be visualized by a diagram with its own set of unique symbols for representing stock and flow. Quantities used in the model are often accompanied by proper units of measurements which are useful for validating model equations. The basic concept of system dynamics was established throughout revisions of the DYNAMO (DYNAmic MOdels) language in the 1960s [Forrester, 1961] and later evolved by other platforms. STELLA (Systems Thinking, Experimental Learning Laboratory with Animation) started as an implementation of DYNAMO for the Macintosh computers in the 1980s and provided a graphical user interface supporting model development directly in the form of stock–flow diagrams [Richmond, 1985]. Many ecological models were implemented on STELLA [Costanza et al., 1998, Costanza and Gottlieb, 1998, Costanza and Voinov, 2001]. Simile is a visual modeling environment primarily based on the concept of system dynamics with additional features of an object-based paradigm suited to spatial and individual-based modeling [Muetzelfeldt and Massheder, 2003].

A role of the crop modeling framework from a software development perspective has been discussed multiple times in the past. An early review suggested that a modeling framework should provide common services essential for implementing a model such as state variable integration and event handling [van Ittersum et al., 2003]. Other common features included a graphical user interface and a standard format for handling data input and output. By separating core simulation logic from other supporting code, models would become more independent and modular for better reuse. A later review revisited the state of crop modeling development to reveal that many long-standing problems were still present after a decade of progress in the field [Holzworth et al., 2015]. Crop models still relied on legacy code written in procedural languages which might not be the best paradigm for implementing scientific models. A standard model interface and internal structure with smaller units of computation aggregated to form a large model was suggested with an emphasis on documentation and testing. A recent review led to a similar conclusion that crop modeling should follow best practices established in software engineering such as adopting domain-specific structures and functions and clear separation of code between model equations and the user interface [Janssen et al., 2017].

In this paper, we propose a new crop modeling framework named Cropbox that allows the models to be expressed in a domain-specific language akin to mathematical model equations where each variable is declared with an explicitly stated intention in relation to other variables. Model developers can write model specifications in a declarative form with no direct need for control flow management as in procedural languages. The framework then takes this high-level model specification and automatically generates lower-level code in a host language after analyzing dependency graphs between variables. Model developers and users are provided with built-in features not limited to running simulation of the model, configuration management, evaluation with common metrics, calibration of parameters, visualization of output results, and manipulation of interactive plots. A core concept and architecture of the framework will be discussed with a few applications taking advantage of different aspects of the framework.

1.2 Design

A core idea of Cropbox modeling framework is to let crop modelers describe their model in a succinct declarative language similar to mathematical equations and let the framework automatically generates a low-level host code that modelers can interact with for a common

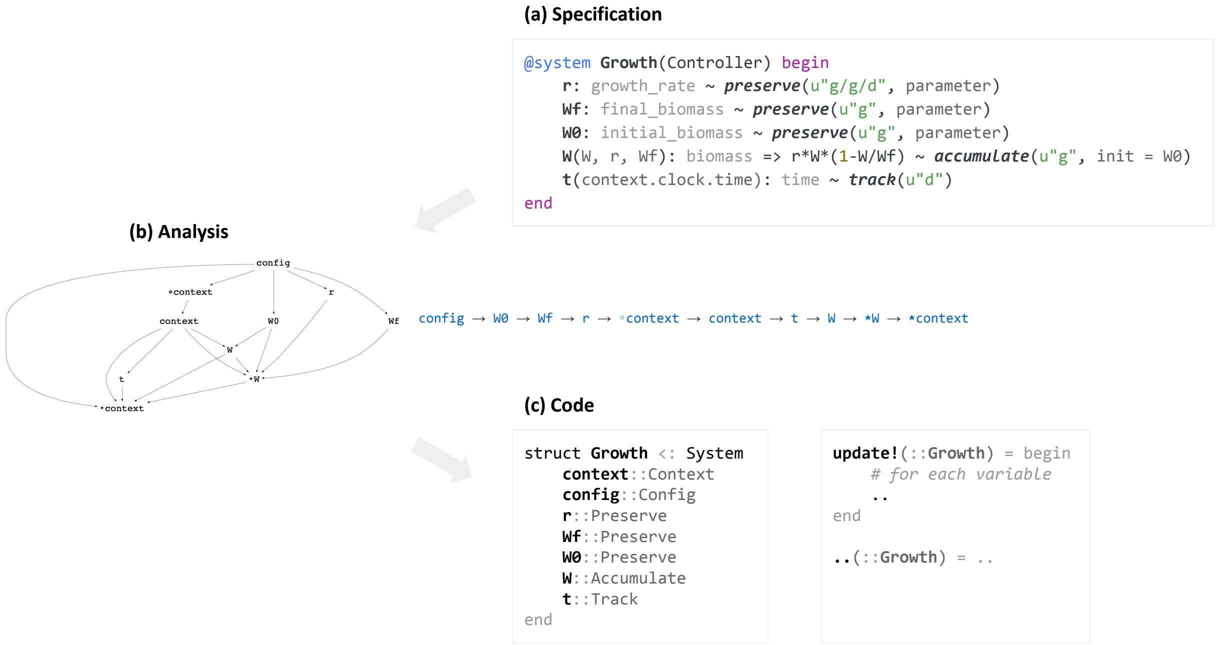

(a) Specification

```
@system Growth(Controller) begin
    r: growth_rate ~ preserve(u"g/g/d", parameter)
    Wf: final_biomass ~ preserve(u"g", parameter)
    W0: initial_biomass ~ preserve(u"g", parameter)
    W(W, r, Wf): biomass => r*W*(1-W/Wf) ~ accumulate(u"g", init = W0)
    t(context.clock.time): time ~ track(u"d")
end
```

(b) Analysis

config → W0 → Wf → r → ∘context → context → t → W → ⋆W → ⋆context

(c) Code

```
struct Growth <: System
    context::Context
    config::Config
    r::Preserve
    Wf::Preserve
    W0::Preserve
    W::Accumulate
    t::Track
end
```

```
update!(::Growth) = begin
    # for each variable
    ..
end

..(::Growth) = ..
```

Figure 1.1: A fundamental concept of Cropbox modeling framework. The framework takes a model specification (a) in declarative domain-specific language and emits host code (c) written in Julia programming language after internal dependency analysis (b) for variables and systems. Model developers then interact with automatically generated model code via several functions provided for simulation, evaluation, calibration, and visualization workflow.

modeling workflow (Figure 1.1).

System is a unit of model component that contains a list of variable declarations. *Variable* is a unit element of the model with a specific *state* associated with a certain behavior. The framework takes a model specification and generate host code based on an existing type system of the host language which is used for creating an instance of the generated type. The framework provides a few *functions* around the generated types to support common modeling workflows. A *configuration* object may be also used for settings parameter values. The Cropbox modeling framework is built on these core elements to support crop model

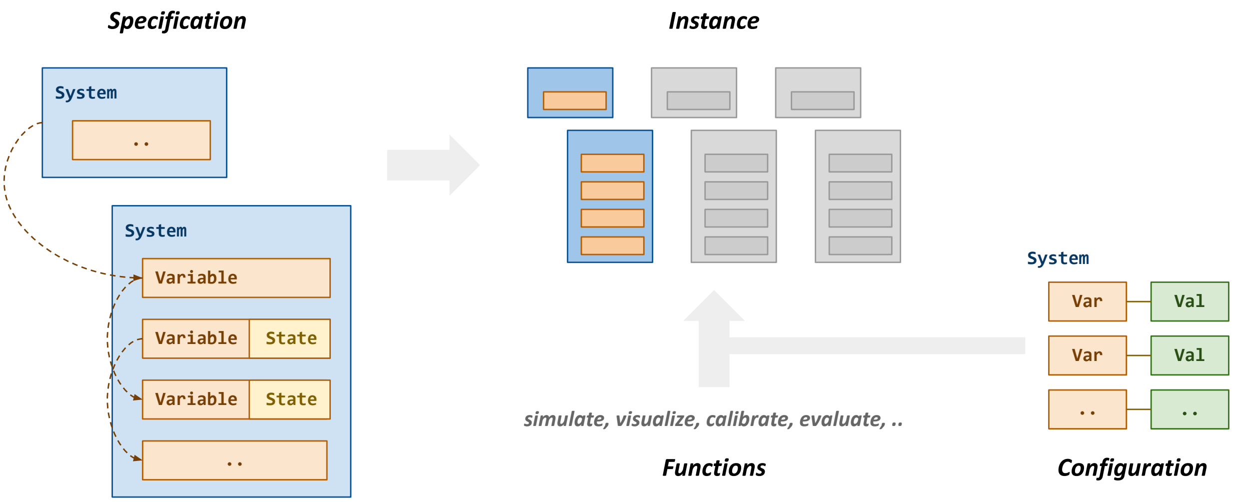

Figure 1.2: An architecture of Cropbox modeling framework depicting core elements. A model *specification* for a *system* contains a list of *variable* declarations. Variables may have specific *states* associated with intended behaviors. An instance of another system may be referred through a non-state variable. The specification for a system is like a mold for casting goods which are hereby called *instances* of the system. One or more system instances may be created with an optional *configuration* for customizing parameter values. Model developers and users then interact with the instances via built-in *functions* supporting a common modeling workflow including simulation, visualization, calibration, and evaluation.

development and application (Figure 1.2). More information about the underlying architecture will be explained in the following sections, starting from a smaller concept like variable and associated states, moving to a larger concept of system and configuration, and finally explaining workflow functions implemented around these concepts.

1.2.1 Variable

A model in the Cropbox framework is represented by relations between variables. Variable is a unit element of modeling that denotes a value determined by a specific operation relying on other variables. The framework provides more than a dozen of predefined operations ranging from a simple constant value assignment to a mathematical equation to a specialized computational code. Operation is internally called *state* in terms of generalizing and expanding the notion of *state variable* as often mentioned in mathematical modeling. State variable, in an original strict term, captures a state of integration upon a dynamic variable with regards to a time variable. In broad terms, we assume more types of state exist to conveniently describe how a model should work in multiple aspects. Associating a single type of predefined operation with each variable gives model developers freedom from needing to understand technical details of how an operation is implemented under the hood and instead focus on what kind of value a variable should keep to describe a desired aspect of the model. Such a clear separation between a high-level model representation and low-level computer code is a core idea of the Cropbox modeling framework. Model developers are encouraged to think around variables as appearing in mathematical equations which they want to translate into a computer model.

Syntax

A state variable in Cropbox is declared in a minimal form like `name ~ state` that indicates a variable named `name` is associated with a state named `state`. Most variables may have additional descriptions inside the body as in `name => body ~ state` that indicates a variable `name` associated with state `state` has a declaration body in the place of `body`. Depending on the associated states, the body can include a simple value, equations calculating a new value, or regular function calls incurring side effects. When multiple lines of statements are needed, a block enclosed by `begin` and `end` keywords may be used. When other variables are required to be referred inside the body, such dependent variables are listed as arguments of variable name as in `name(args...) => body ~ state`. Similarly, state-specific options, called tags, may appear as arguments of state name as in `name => body ~ state(tags...)`. Commonly used tags include unit specifier (`unit` or `u".."`), parameter indicator (`parameter`), and clamping range (`min`, `max`). Variables may opt to have an alias which often has a longer descriptive meaning than the original name which is encouraged to be kept short for convenience in reference from other variables. An internal data type can be also specified following the name of state as in `state::type` when default floating point type is not enough, for example, when strict integer type is needed for counting. Note that a state is not mandatory for variable declaration as regular variables are also allowed in a form like `name => body` or `name => body ~ ::type`. Such non-state variables are often used for referencing another system to access variables declared inside.

States

There are currently 18 kinds of state implemented in the framework. Some variables describing essential building blocks of a model are more common than others more specialized to handle unique but complex tasks. Here we provide a brief overview on common states used for variable declaration.

preserve is used when the value of a variable should be kept constant with no further modification after initial assignment. Hence it is often used for declaring a parameter variable where its initial value can be set via a configuration object supplied with the onset of simulation. Non-parameter constant variables may also appear depending on model specification, for example, to freeze a value from a certain time point and lower computational cost since no update is required for each time step in contrast to other kinds of variables like track as discussed later.

```
r: growth_rate => 0.05 ~ preserve(u"d^-1", parameter)
```

In this example, a variable named `r`, also referred to `growth_rate`, has the default value of $0.5\,\mathrm{d}^{-1}$ which does not change during simulation. Since it is tagged as `parameter`, the value could be replaced by other values via configuration at initialization.

track is for tracking a result of a computation as often done in an update loop in conventional model code. For each time step, a model equation coded in the variable declaration body is evaluated and saved for use by other variables. Note that assignment of value can happen only once per time step as determined by the framework and no manual assignment at an arbitrary point of computation is allowed as with procedural programming. This *declarative* aspect of the framework is to prevent any logical errors due to premature or incorrect order of variable assignments which can happen frequently in model development. For example, two variables declared to track each other with a circular reference would be easily caught by the framework during the model analysis phase before code generation while they would still remain valid statements in general programming languages resulting in a subtle bug hard to discover unless something happens with the output to indicate an obvious error.

```
SLA(area, mass): specific_leaf_area => begin
    area / mass
end ~ track(u"cm^2/g")
```

In this example, a variable named `SLA`, also referred to `specific_leaf_area`, is calculated by two other variables `area` and `mass`. For every time step, the variable will be updated with a new value from calculation. Since the calculation depends on values from other variables, dependent variables `area` and `mass` are updated before updating `SLA`.

accumulate represents integration of differential, or more precisely, difference equations over time. The numerical integration is equivalent to the Euler method with a fixed time step since other advanced numerical methods relying on variable time steps are not compatible with the discrete nature of some variables like produce. In Cropbox, any kind of variable can become an integrating variable or corresponding time variable without explicit distinction such as influence, intermediate variable, and parameters in system dynamics. Declaration body for the accumulate variable dictates how an accumulation rate is calculated. As the framework is equipped with native support for unit conversion and validation, the units of a rate variable must conform to the units of an integrated variable. For example, for accumulation of biomass in the unit of g, the rate calculation must result into a unit with a time component such as $\mathrm{g\,d^{-1}}$. Calculation of rate is done at the end of each time step, but actual accumulation occurs in the beginning of the following time step to ensure a newly updated value is not accidentally leaked to external access at the end of previous time step. For convenience, a similar kind of variable named capture is also provided to allow tracking of rate values calculated for each time step.

```
LTA(r = LTAR_max, β = BF.ΔT): leaf_appearance => begin
    r * β
end ~ accumulate(when = leaf_appearing)
```

In this example, a variable named `LTA`, also referred to `leaf_appearance`, increases by the rate calculated with other variables, `LTAR_max` and `BF.ΔT`. For convenience, the latter two variables are referred by shorter names, `r` and β, inside the declaration body. Initial value of variable is implicitly assumed to be 0 when no `init` tag is used. The use of `when` tag indicates that accumulation should only happen when `leaf_appearing` is true.

flag is basically the same as track but explicitly typed for boolean values, true and false. In addition to tracking a conditional value for each time step, the flag variable can be easily composed with other flag variables for making a new conditional expression like `appeared & !removed` on the fly to indicate a condition when something is appeared but not removed yet. Triggering different computation pathways depending on such a flag is quite common in crop models especially backed with complex phenology in developmental stages.

```
leaf_appeared(i = N_initiated, a = N_appeared) => begin
    0 < i <= a
end ~ flag
```

In this example, a variable named `leaf_appeared` is updated with the result of comparison between numerical values including other variables, `N_initiated` and `N_appeared`. For convenience, the two dependent variables are referred by aliases, `i` and `a`, inside the declaration body. The result should be a boolean value which is either `true` or `false`.

drive pulls value from a time-series data source which can be a simple vector or a column from a tabular data frame. Depending on the type of specified index variable which often coincides with a default time or calendar date variable, new values are pulled from the source every time step. In other words, the **drive** state declares a *driving variable*, hence the name. When the data source is in a data frame, **provide** can be used to layer down a convenient interface for loading from external files, handling index columns, and automatic unit conversion from column names.

```
Ta: air_temperature ~ drive(from = s, by = :Tair, u"°C")
```

In this example, a variable named `Ta`, with a long alias referred to `air_temperature`, is pulled *from* a data frame store named `s` *by* the index column named `Tair`. The unit of column should be in °C as specified by the unit string literal `u"°C"`.

Aside from the basic kinds of variable introduced so far that are more frequently used in a general model development, some variables are reserved for abstracting specialized tasks often complex enough to implement from scratch.

bisect constructs a loop for iteratively solving a numerical equation between variables. With a lower and upper boundary of the variable to be solved given in the declaration, the framework would automatically generate a proper control flow structure for implementing an iterative solver. When multiple equations are dependent on each other and declared with more than a single **bisect** variable, dependency analysis should be able figure out a correct order of iterative solving implemented in a nested control structure. A typical example can be found in the implementation of coupled gas-exchange model where solving intercellular CO_2 level (C_i) determined by an empirical relationship between biochemical photosynthesis and stomatal conductance models. Energy balance equation may be solved via additional bisect variable internally relying on C_i that led to a nested loop generated in the host code.

```
Ci(Ca, Ci, A_net, gvc): intercellular_co2 => begin
    Ca - Ci == A_net / gvc
end ~ bisect(min = Cimin, upper = Cimax, u"μbar")
```

In this example, a variable named `Ci`, also referred to `intercellular_co2`, is determined by numerically solving a steady-state equation constructed with a few other variables. As the bisection method requires a boundary of solution, `min` and `max` tags are set via corresponding variables named `Cimin` and `Cimax`. The solution of equation saved to `Ci` is in the unit of µbar.

solve is another kind of variable for solving a system of equations when the target equation is symbolically solvable to produce an analytical solution. Since actual analysis for solving equations occurs during the code generation phase and only the solution represented in a new fixed form is included in the generated code, impact on runtime performance should be kept minimal. An example can come from stomatal conductance model to solve leaf surface humidity (H_s) which is a key variable for linking biochemical photosynthesis model.

```
J(I2, Jmax, θ): electron_transport_rate => begin
    a = θ
    b = -(I2 + Jmax)
    c = I2 * Jmax
    a*J^2 + b*J + c == 0
end ~ solve(lower = 0, upper = Jmax, u"μmol/m^2/s")
```

In this example, a variable named `J`, also referred to `electron_transport_rate`, is determined by solving a quadratic equation declared inside the body enclosed in a block between `begin` and `end`. A symbolic solution of the quadratic equation is derived during the code generation phase and an actual value of solution is computed runtime with the current values of dependent variables, `I2`, `Jmax`, and θ. Since quadratic equations can have two different solutions, a boundary of solution is additionally specified via `lower` and `upper` tags to chose a more likely solution.

produce supports instantiation of a new system during runtime to allow dynamic expansion of overall model structure which is an important feature differentiating functional-structural plant models (FSPM) from conventional crop models with a rather static structure. We used produce to build a 3D root structure growth model for switchgrass (*Panicum virgatum*).

```
R(R, N, wrap(RT0)): roots => begin
    [produce(Root; RT0) for i in (length(R)+1):N]
end ~ produce::Root[]
```

In this example, a variable named `R`, also referred to `roots`, contains a list of system instances dynamically produced runtime. `produce()` inside the declaration body is a function to create a new instance of system for produce variable. In this particular example, new instances of `Root` is *produced* for each time step if the total number of instanced stored in `R` is less than the total number set by `N`. A constructor for `Root` system accepts a keyword argument named `RT0` to receive a variable holding a transformation matrix. Note the use of `warp()` function to pass a reference to the variable, not a value of variable, to ensure any changes in the matrix can propagate down the hierarchy of root structure.

1.2.2 System

System is a unit of model component that contains a collection of variables declared with metadata as described above. Variables declared within a system must have a linear order of computation which is automatically determined by dependency analysis during the code generation phase. If any inconsistency resulting in a cyclic dependency was found, an error would be thrown. A system can be viewed as a class in object-oriented programming in which its definition is like a blueprint that can imprint an instance of a system where actual states of the variables are maintained. Any model declared in Cropbox first needs to have its underlying systems instantiated before running the simulation.

In a complex model, a system can be composed of other systems as mix-ins in a sense that the system *has* the same declarations of variables copied from other systems. For example, a gas-exchange model is defined by a system named `LeafGasExchange` that may be composed of multiple components such as `C3Photosynthesis`, `StomataBallBerry`, `EnergyBalance` and the likes. Composition is a primary way of supporting modular model development in Cropbox. If needed, a mix-in component declared as a part of an existing system can be substituted with another mix-in in a new system declaration to facilitate a plugin architecture. A new system built by composition has all the variables declared in constituting mix-in components, but the system itself is not recognized as any of them in the type system. In other words, an instance of new system composed by mix-ins cannot be directly plugged in a place where the variable was declared with a type of any mix-ins listed.

When polymorphism is needed in a specific modeling task, a system can optionally have a base type which is inherited by the new system. In other words, a new system *is* essentially a kind of parent system in a sense that the type of child system is inherited from the type of parent system. For example, in root structure modeling, different types of root segments may be inherited from the same `BaseRoot` system sharing common declaration of variables like length and angle, and each system would be declared as a subtype of `BaseRoot` , namely `PrimaryRoot`, `FirstOrderLateralRoot`, and `SecondOrderLateralRoot`, to model a specific behavior of growth for each root type. Without an explicit declaration of base type, systems are all inherited by an abstract `System` type by default in Cropbox. Inheritance is therefore useful for making a set of common interfaces around a hierarchy of custom system types. The root structure model would rely on produce variable for dynamically generating instances of inherited systems and then would implement custom features such as rendering of 3D structure represented by each root segment system.

Context

Every system has an internal variable named `context` which is a non-state variable referencing to an instance of the `Context` system. Context serves two critical purposes in simulation: time and configuration management.

```
@system Context begin
    context ~ ::Nothing
    config ~ ::Config(override)
    clock(config) ~ ::Clock
end
```

`Clock` system referred by the `clock` variable in `Context` keeps track of a few time-related variables, namely `init`, `step`, `time`, and `tick`. `time` is a variable declared as advance which is a variable state similar to accumulate but tailored for keeping time. `time` accumulates from an initial value `init` by an interval value `step` for each update call that governs an overall time frame of simulation. Without custom configuration, `time` starts from 0 hour and increases by 1 hour interval that assumes hourly simulation of crop models. `tick` is another time variable keeping the same time frame by just counting the number of updates. Thus `context.clock.time` or `context.clock.tick` is often used as an index of data frame storing simulation output and as the x-axis of a plot visualizing such output. Most of the time, a single instance of context is shared between multiple systems under a homogeneous time frame. Adopting a heterogeneous time frame for a certain group of systems is then allowed by assigning an instance of context with an independent clock configuration to them.

`Config` referred by the `conig` variable in `Context` is not a system, but a configuration object structured as a nested dictionary or hash table to store user-defined parameter values as a triplet of system – variable – value. A parameter value specified in configuration is plugged into a preserve variable with `parameter` tag during initialization of the variable.

```
:S => (;
    a = 1,
    b = 2,
)
```

In this example, a configuration object contains parameter values for system named `S` which includes two variables named `a` and `b`. The two variables will be set to 1 and 2, respectively, when the system is initialized with this configuration object.

The framework supports a couple of handy operations around a configuration object to facilitate a large scale simulation, *i.e.*, in temporal and spatial domains. A new configuration object may be created by merging two or more existing configurations. Since a parameter value referring to the same variable of a certain system would be overridden by a value from later configuration, Cropbox encourages organizing a set of small pieces of configuration to assemble a large one. Helper functions are also provided to populate multiple configuration objects from a range of values assigned for a specific parameter. For convenience, `@config` macro provides operator-based syntax to support complex operations like merge and expansion of configuration in a relatively simple statement.

Controller

An instance of context and configuration provided to a new instance of a system usually comes from a parent system that owns a variable referring to the system and thus initiates an instantiation of it. However, since there would be no parent system for the first system getting instantiated, context and configuration need to be supplied elsewhere.

```
@system System begin
    context ~ ::Context(override)
    config(context) => context.config ~ ::Config
end
```

`Controller` is a built-in mixin to avoid such initiation issues by creating its own instance of `Context` to be shared by other systems derived from the controller. A system constructor such as `instance()` and other functions relying on it such as `simulate()` and `visualize()` accept a `Config` object passed through a keyword argument (`config`) to allow overriding parameters. Therefore at least one and usually only one system is designated to possess `Controller` as the final element in the mixin list. The system augmented with `Controller` is what model users expect to primarily interact with in their workflow.

```
@system Controller begin
    config ~ ::Config(override)
    context(config) ~ ::Context(context)
end
```

1.2.3 Implementation

Cropbox modeling framework is written in Julia language and publicly available as a package named CROPBOX.JL with an open source license [Cropbox.jl]. Julia is a relatively new language with a strong focus on scientific computing that often demands high performance while also benefitting from features of dynamic programming languages [Bezanson et al., 2017]. Especially, dynamic code expansion using macros allowed implementation of the framework in a domain-specific language with semantics covering the concept of system and variable in a surface syntax readily supported by Julia language.

A system is defined with `@system` macro followed by a block containing variable declarations with syntax described above When this macro is expanded, the framework generates code for defining a new **`struct`** for the system and several internal functions around it. Each variable becomes a field in the **`struct`** wrapped with corresponding `State` type equipped with variable-specific code generation logic. The new **`struct`** is defined to be a subtype of `System` or an optional base type as specified in the declaration for inheritance purposes.

During macro expansion, the framework keeps track of all variables declared in the system and creates a dependency graph based on dependent variables listed in the declarations. Topological sorting algorithm is then applied to the dependency graph to figure out a linear order between variables. For example, if variable `b` depends on variable `a`, update code for `a` must execute before updating `b` to prevent premature access to an old state of `a` from previous time step. A determined variable ordering is used in code generation to properly lay down variable handling logic in system initialization and update functions.

Some variable kinds may rely on a more fine-grained control of update timings. For example, the **accumulate** variable has to calculate a new rate for the next time step by the end of the current time step while this new rate should not be assigned to the accumulated value for the current time step. These two operations, accumulate by a rate from last time step, and calculating a new rate for the next time step, are internally split into *main* and *post* steps which become two separate nodes in the dependency graph. Any reference to this variable makes two dependence edges to both nodes while *post* node has a dependent edge on *main* node. A deliberate separation between the two nodes ensures calculation of a new rate take place after finishing updates of all other variables relying on this variable. The **bisect** variable uses a similar mechanism with two steps, *pre* and *main*, to form a loop implementing iterative updates of solution. For an uncommon circumstance where per-system level control flow using steps is not enough, the framework provides per-context level hooks called stages to allow inserting code before or after updating all systems under the same context. The **produce** variable relies on three stages, *pre*, *main*, and *post*, to instantiate a new system before any other variables can see it at the beginning of a time step while passing necessary information for instantiation to the next time step. Note that these technical details are not necessarily exposed to model developers and abstracted away by the use of declarative syntax.

1.2.4 Workflow

Cropbox provides several core functions to support a typical workflow for crop model simulation. The `simulate()` function accepts a system generated with the `@system` macro to run dynamic simulation over multiple time steps until a certain stop condition is met while inspecting the current state of running systems for each time step to extract variables of interest into a tabular data frame.

```
simulate(Garlic.Model;
    config = Garlic.Examples.AoB.KM_2014_P2_SR0,
    stop = "calendar.count",
)
```

The stop condition (`stop`) can be simply a total number of updates or time period suffixed with a proper time unit such as hour and day. If more sophisticated control is needed, a dedicated **flag** variable can be declared in the model and passed as a stop condition. For maximum flexibility, any function accepting an instance of system to implement a custom logic for checking stop condition can be also used.

For models relying on external parameters, the configuration option (`config`) can accept either a single configuration object or a list of multiple configurations. In the latter case, multiple iterations of simulation for each configuration object will be conducted and the output will contain a result aggregated from each simulation. Multithreading can be enabled for maximizing performance on a multi-core processor.

With an output stored in a common format of data frame, users can proceed with further analysis and visualization on their own by using any data science packages in Julia. Cropbox also has the `visualize()` function to allow plotting a few types of graph from a list of variables declared in the system. The name of variable in a symbol (*e.g.* `:A_net`) or a full path of variable in a string with enclosing system names (*e.g.* `"LeafGasExchange.ModelC4MD.A_net"`) are used for indicating horizontal and vertical axes of the graph.

```
visualize(ModelC4MD, :Ci, [:A_net, :Ac, :Aj];
    config = ge_base,
    xstep = :Weather => :CO2 => 10:10:500,
    kind = :line,
)
```

Multiple variables of similar units and scales can be specified via a grouping option (`group`) to draw multiple lines of variables (*e.g.* `A_net` and `A_gross` at the same time) with distinct colors and labels for visual comparison.

In the Jupyter notebook environment, interactive exploration of plots can be possible with the `manipulate()` function similar to `visualize()` but extended with a list of value ranges for parameters controlling the shape of graphs. An interactive user interface is rendered in the notebook for each parameter with a slider widget that users can employ to freely change a parameter value. A change in the slider would trigger a new simulation running under the hood and a new plot redrawn on the fly.

```
manipulate(ModelC3BB, :T, :A_net;
    config = ge_base,
    parameters = (
        :Weather => :PFD => 0:100:2000,
    ),
    xstep = :Weather => :T_air => 0:1:45,
    group = :Weather => :CO2 => [1000, 400, 250],
    xlim = (0, 45),
    ylim = (0, 35),
    kind = :line,
)
```

When an optimal set of parameters is needed, the `calibrate()` function supports parameter fitting using a global optimization method. The optimization method attempts to find a best fit set of parameters under a given observation dataset and given boundaries of parameter values. The observation dataset should be organized in a similar structure to the output data frame so that there exists a mapping between variables for observation and model estimation. Variables can be categorized into *index* or *target* depending on their role in the mapping. Index variables become index columns when two datasets are joined for comparison and usually consist of time components int the case of dynamic simulation models. Target variables are non-index variables that are subject to evaluation of fitness.

```
calibrate(ModelC3BB, obs, obs_configs;
    index = [
        :PARi => :PFD,
        :CO2S => :CO2,
        :RH_S => :RH,
        :Tair => :T_air,
        :Press => :P_air,
    ],
    target = [:Photo => :A_net, :gs],
    parameters = (
        :StomataBallBerry => (;
            g0 = (0, 1),
            g1 = (0, 10),
        ),
    ),
)
```

For convenience, the `evaluate()` function provides several evaluation metrics like RMSE (root mean square error) and Nash-Sutcliffe model efficiency using the same interface as `calibrate()`.

```
evaluate(obs, est;
    index = :measuring_date => :date,
    target = :bulb_dry_weight => :bulb_mass,
    metric = :ef,
)
```

All workflow functions are supported on the Jupyter notebook environment which is well suited for running existing models for explanatory research. For developing a model as a Julia package structured with more than a single file, developers may prefer a conventional development environment based on a code editor and REPL (read-eval-print loop). Cropbox was developed to support an entire modeling and simulation workflow running under a terminal-oriented environment. For example, `dive()` function allows inspection of the current state of a system instance by navigating enclosed variables using keyboard shortcut in REPL. Plots can be still rendered in a legible format using a set of text letters without heading to a notebook.

1.3 Applications

1.3.1 Coupled Gas-Exchange Model

A coupled gas-exchange model is an important building block of any crop model for a precise assessment of carbon assimilation under diverse environmental conditions which are often hard to capture with empirical approaches. Our implementation of a coupled gas-exchange was based on an existing model written in C++ and later expanded to become a part of maize (MAIZSIM) and garlic models [Kim and Lieth, 2003, Kim et al., 2006, Hsiao et al., 2019]. The model was then reimplemented with the Cropbox framework in Julia and recently used to compare behavior of stomatal conductance sub-models integrated with a coupled gas-exchange model for a C4 leaf [Yun et al., 2020] (Figure 1.3).

The original model was coded in a monolithic class that contained all parameters and variables in a single location. Variables were updated via explicit calls to several functions representing sub-models such as stomatal conductance and energy balance. These functions were written carefully to calculate new values of each variable in a correct execution order. There were iterative solvers implemented in two locations, one for obtaining intercellular CO_2 (C_i) and the other for adjusting leaf temperature. Tracking iterations and updating respective variables had to be coded explicitly inside the loop [Kim and Lieth, 2003]. Some

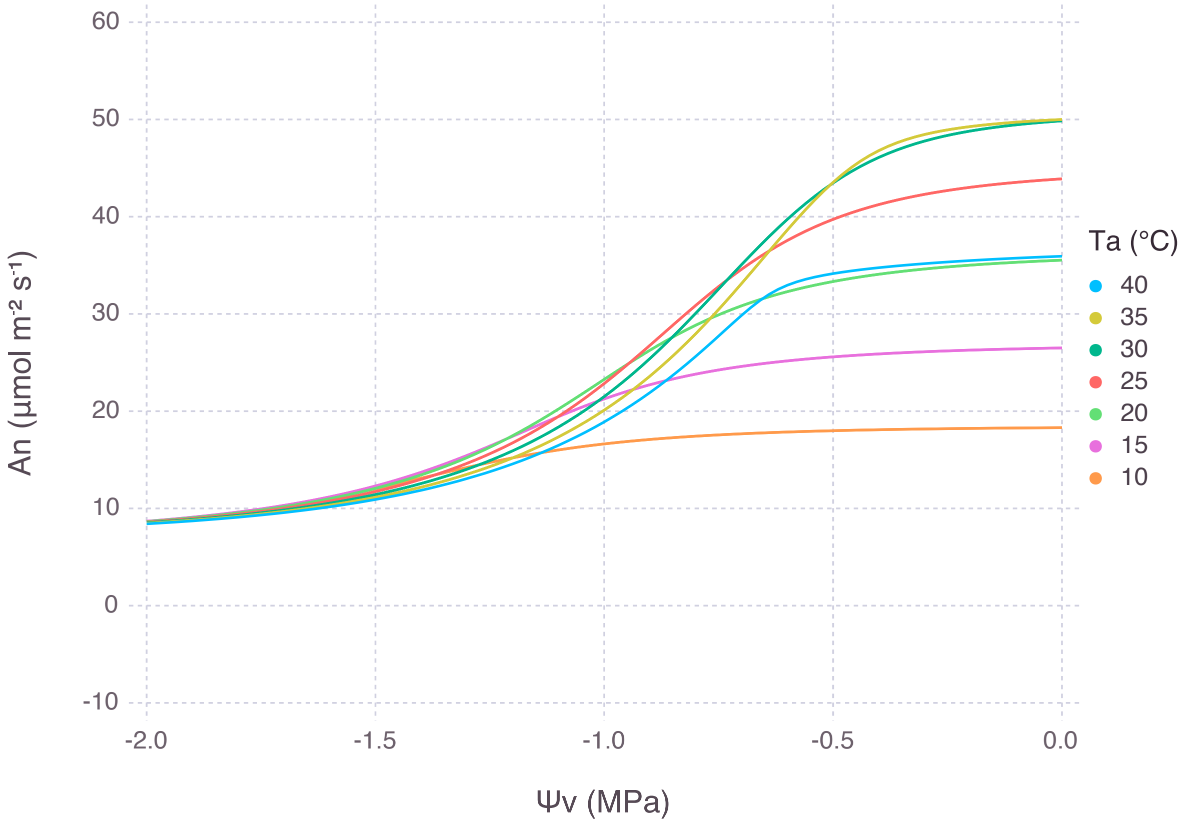

Figure 1.3: Net photosynthesis rate of a C_4 leaf simulated by LeafGasExchange.jl under diverse combinations of air temperature (T_a) and leaf water potential (Ψ_v). Relative strength of water stress was dependent on temperature which was a primary factor determining a potential rate of photosynthesis.

parameters were stored in a separate structure to allow customization before running the model. Output variables were available via instance methods and a few of them were saved in a file after simulation was done, but further analysis and visualization would require external tools.

The reimplemented model using Cropbox, released as the LeafGasExchange.jl package, had a modular structure with more than 30 small systems representing a consolidated aspect of the gas exchange process and its hierarchy. For example, three different stages of limitation in C_3 biophysical photosynthesis were divided into separate systems, namely `C3c`, `C3j`, `C3p`, for representing enzyme-limited, electron transport-limited, triose phosphate-limited pathways, respectively. Then `C3` system was composed with these components to provide net photosynthesis rate (`A_net`) and related outputs by comparing rates calculated from different pathways. Variables were declared with explicit units such as $\mu\mathrm{mol}\,\mathrm{m}^{-2}\,\mathrm{s}^{-1}$ for net photosynthesis (`A_net`) and $\mathrm{mol}\,\mathrm{m}^{-2}\,\mathrm{s}^{-1}\,\mathrm{bar}^{-1}$ for stomatal conductance (`g_s`). Difference in scaling between units like µmol and mol were automatically handled via implicit conversion triggered on variable updates.

A complex control structure introduced to implement a iterative solver in the original model was replaced by the bisect variable. Bisection method is slow to converge but is guaranteed to find a solution if one exists within a given boundary unlike faster methods occasionally failing under a certain condition such as low atmospheric CO_2 concentration. In the case of solving an energy balance equation, adoption of the bisection method allowed removal of leaf temperature linearization relying on Taylor expansion [Paw U and Gao, 1988]. As a result, the code became more intuitive that looked exactly the same as the original energy budget equation ($R_n = H + \lambda E$).

```
ΔT(R_net, H, λE): temperature_adjustment => begin
    R_net == H + λE
end ~ bisect(lower=-5, upper=5, u"K", evalunit=u"W/m^2")
```

Manually solving a quadratic equation for relative humidity at leaf surface (H_s) based on an empirical relationship between photosynthesis and stomatal conductance was replaced by the `solve` variable to generate code for an identical symbolic solution during macro expansion.

```
hs(g0, g1, gb, An, Cs, RH): humidity_surface => begin
    gs = g0 + g1*(An*hs/Cs)
    (hs - RH)*gb == (1 - hs)*gs
end ~ solve(lower = 0, upper = 1)
```

Cropbox supports selection of arbitrary output variables instead of a fixed set as in the original model that allows model developers and users freely to look into any variables of interest by running simulation with corresponding `target` variables. In the original model, adding new output variables requires modification of source code followed by recompilation which can easily interrupt exploratory workflow. With extended features and added usability, LeafGasExchange.jl (version 0.1.0) was written in 407 lines of Julia code which was 40% smaller compared to the original standalone model written in 680 lines of C++ code.

1.3.2 Garlic Growth Model

A crop model is an integrated collection of multiple building blocks such as phenology development and structural growth based on carbon assimilation and allocation. A process-based garlic model for hardneck garlic was based on the coupled gas-exchange model reviewed above with canopy-level scaling and other necessary processes to describe whole-plant growth [Hsiao et al., 2019]. The original model written in C++ was reimplemented in Julia using Cropbox framework and released as Garlic.jl package (Figure 1.4).

The original model was composed of 16 classes representing plant structure and relevant biophysical processes. In the reimplemented model, they were expanded into more fine-grained 63 systems to cover the same functionalities. For example, a single class implementing a coupled gas-exchange model was translated into 14 systems as illustrated in the

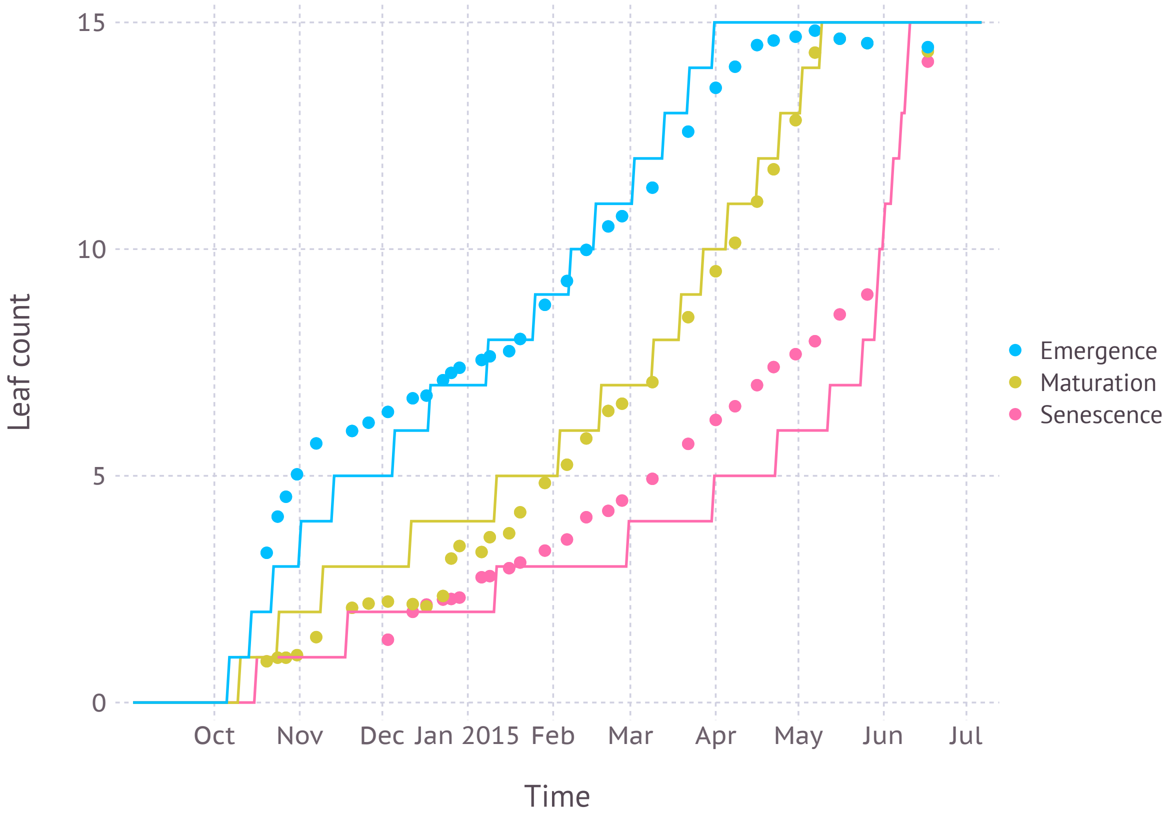

Figure 1.4: Leaf development simulation for garlic (*Allium sativum* 'Shantang Purple') by GARLIC.JL and compared with observed field data. This figure is a reproduction of Fig. 3A from Hsiao et al. [2019] using the same dataset and parameters.

previous section. Systems were placed under directories named **morphology**, **phenology**, **physiology**, **atmosphere**, and **rhizosphere** according to their roles in the model.

For **phenology**, a single class for tracking development in the original model was split into a set of small systems by consolidating each phenology stage into a separate system. Such reorganization of code into a smaller unit increases cohesion of each system by grouping interdependent variables while enforcing a boundary between unrelated variables. A fine-grained organization of systems also entails a similar hierarchy of configuration which effectively groups enclosed parameters into a more specific categories with better identifiability.

morphology contains systems describing the physical structure of the plant where leaf was given most details due to its importance in dictating overall growth of the plant. Each individual leaf is described by a single instance of Leaf system with its own tracking of elongation and lifecycle according to thermal time accumulation. An instance of an enclosing nodal unit is dynamically created and added runtime via the produce variable. Aside from leaves, systems for other structures and processes are static in a sense that no addition or removal of instances occurs once systems are initialized at the beginning of the simulation as for the static architecture of typical crop models.

Some variables need to aggregate values from multiple instances of a dynamic system. For example, total leaf area in `Area` mixin system in **physiology** would be a sum of leaf area from individual leaf instance inside a nodal unit. Such aggregate variables can be declared with an aggregate syntax using index key on produce variable.

```
leaf_area(x = NU["*"].leaf.area) => begin
    sum(x)
end ~ track(u"cm^2")
```

`leaf_area` variable is declared in `Area` mixin for calculating total leaf area by summing up individual leaf areas from all nodal units (`NU["*"]`). Each nodal unit has a `leaf` which is an instance of `Leaf` system and each leaf has a variable `area` for tracking leaf area growth over time. `sum()` is a standard Julia function for calculating the sum of all elements in a collection. `NU["*"].leaf.area` returns a collection of leaf area from individual leaves.

physiology contains several mixins for `Plant` system which encompasses all other systems in the package. Notable mixins include `Area` for tracking total leaf area, `Mass` for tracking biomass of each plant structure, `Count` for leaf counting. `Photosynthesis` is a mixin for scaling up leaf-level `GasExchange` to canopy-level by incorporating a sunlit and shaded leaf approach with canopy radiation calculated via `Radiation` mixin. The `Garlic.Model` system which is a primary system that users interact with is indeed `Plant` with `Controller` added for making the system instantiable.

For running multiple simulations with the original model, dedicated Python scripts had to be written for running the model with template-based configuration files and for aggregating results from parsing output files. With Cropbox, `simulate()` and `@config` provides a uniform interface regardless of model implementations that the new garlic model no longer had to rely on custom script files. Albeit with more features, GARLIC.JL (version 0.1.16) was written in 1987 lines of Julia code which was smaller than 2750 lines of C++ code written for the original garlic model (version 0.1.10).

1.3.3 3D Root Structure Model

Although Cropbox modeling framework was originally designed for developing conventional crop models with a rather static structure as seen with examples above, the framework itself does not preclude uses for more dynamic models often evidenced by functional-structural plant models (FSPM). A major difference with such structure-oriented models compared is the sheer amount of dynamically produced structures interconnected to describe an important aspect of plant growth which is often difficult to capture by empirical models dealing with a more approximated structure. As structures are dynamically generated during simulation, the framework must provide a means to handle addition of a new instance of the system at a proper timing compatible with how other variables work as briefly explained with the internals of produce variable relying on three stages. Support for aggregation via a special syntax also help with managing a large number of systems in a consistent way.

Implementation of a 3D root structure growth model was based on an algorithm proposed by CRootBox [Schnepf et al., 2018]. With multiple types of roots depending on branching order, a strain of each root type consists of multiple root segments. With our implementation named CropRootBox.jl, a root type corresponds to a system and a root segment is then represented by an instance of a certain system. Like individual leaf production in the garlic model, each root segment is produced from another root segment when the accumulated length of connected segments exceeds a certain threshold specified by a parameter. For randomness in the growth, parameter values are given with standard deviations (*i.e.* `:S => :a => 1.0 ± 0.1`) and the actual values are sampled from corresponding normal distributions on initialization. As new root segments can be added in two variations, axial growth and lateral branching, two separate produce variables were used. For interoperability between different root types, 'BaseRoot' which contains all necessary parameters and state variables as well as branching transition table is inherited by concrete subtypes of each root such as `PrimaryRoot` and `FirstOrderLateralRoot` systems.

The current position of a root segment is calculated with a chain of transformation matrices. Local transformation matrix is determined by the length of elongated segment (`l`) and branching angle from parent segment, namely axial angle α and radial angle β . For a current position vector (`cp`) in a global coordinate system, global transformation matrix (`RT1`) is obtained by multiplication of local transformation matrix (`RT`) and previous global transformation matrix of parent segment (`RT0`). A reference to the variable holding global transformation matrix (`RT1`) is passed down to subsequent systems by overriding a track variable itself pointing to the parent transformation matrix (`RT0`) rather than by mere copying of matrix values in order to ensure any changes made in parent system, such as translation vector change due to root elongation, automatically propagates down to child systems so that global transformation matrices (`RT1`) in child systems receive proper updates for each time step.

```
RT0: parent_transformation ~ track::Transformation(override)

RT(nounit(l), α, β): local_transformation => begin
    T = Translation(0, 0, -l)
    R = RotZX(β, α) |> LinearMap
    R ∘ T
end ~ track::Transformation

RT1(RT0, RT): global_transformation => begin
    RT0 ∘ RT
end ~ track::Transformation

cp(RT1): current_position => begin
    RT1(Point3f0(0, 0, 0))
end ~ track::Point3f0
```

Once the simulation is over, a network of more than thousands of root segments could be produced as a result. For rendering root structure in 3D space, a custom Julia function was written to collect a list of meshes generated from each root segment by recursively visiting systems with `Rendering` mixin which worked as a trait without further variable declarations. A collected list of 3D mesh can be used to make an interactive 3D visualization directly launched from Julia session or export to a VTK file for further processing with external programs (Figure 1.5).

CropRootBox.jl (version 0.1.2) was written in 356 lines of Julia code. For a comparison, CRootBox (as of Nov 6, 2019) was written in 4610 lines of C++ code with additional Python bindings but came with more complete built-in features like segment analysis. Note that CropRootBox.jl was never intended to be a full reimplementation of CRootBox, but built as a proof of concept for applying FSPM approach within the Cropbox framework. For this purpose, CropRootBox.jl showed a potential to fill the gap between conventional crop modeling and FSPM within the same framework. Future work will be focused on supporting custom functions with fewer boilerplate codes by providing a more intuitive interface for matching and aggregating multiple instances of systems stored in the `provide` variable.

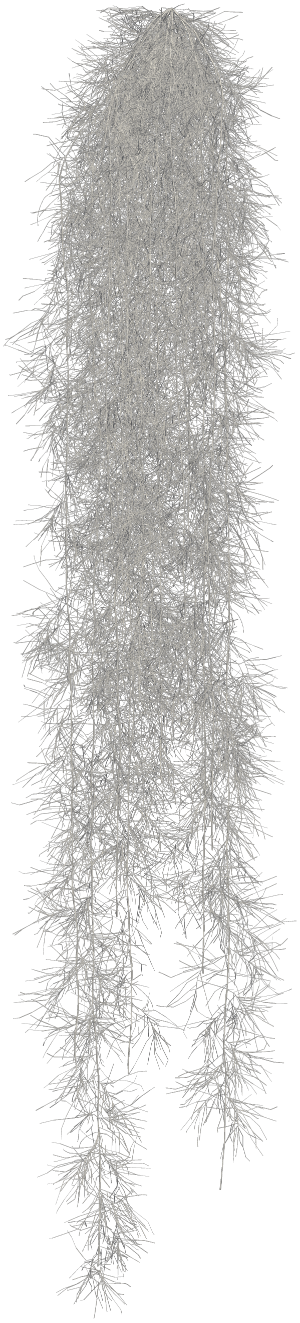

Figure 1.5: Rendering of 3D root structure simulated by CropRootBox.jl for switchgrass (*Panicum virgatum*). Three root types were modeled by corresponding systems and a large number of instances of these small root segments were dynamically generated during simulation via `produce` variable.

1.4 Conclusions

Cropbox modeling framework is capable of implementing various aspects of crop modeling in concise forms compared to conventional approaches. Model development often involves lots of technical details that seemingly look trivial at first, but then turn out to be hampering, especially when trying to implement simulation models from scratch without relying on any framework. A declarative approach using domain-specific language (DSL) adopted by the Cropbox framework minimizes the amount of implementation details exposed to model developers. Model developers only need to focus on the meaning of variables and relationships to other variables instead of how such variables are implemented. Surface language available to the developers are deliberately limited to avoid unintended side effects from incorrect mutation of variables and control flows. The framework instead takes charge of the complexity by automatically generating necessary code based on dependency analysis and specific requirements pulled from variable declarations. With such details hidden from a model representation, an underlying logic behind model equations suddenly becomes more transparent and helps users understand the model better. Model code generated by the framework is still a valid Julia **`struct`** type that warrants extension via custom functions accepting said types. For example, users can make a wrapper function to use custom optimization methods with an instance of the Cropbox system. Similarly, a rendering function for root structure was implemented as an extension to Cropbox systems utilizing an existing mesh rendering library for Julia. Utilizing existing infrastructure from a Julia data science stack on Jupyter notebook to Python and R library bindings can improve productivity of crop modeling workflow. Such usability as a DSL is an advantage of Cropbox over other tools with limited access to a general programming workflow.

BIBLIOGRAPHY

Jeff Bezanson, Alan Edelman, Stefan Karpinski, and Viral B. Shah. Julia: a fresh approach to numerical computing. *SIAM Review*, 59(1):65–98, 2017.

R D Brennan and M Y Silberberg. The System/360 continuous system modeling program. *Simulation*, 11(6):301–308, 1968.

R E M Caskie and R E A Mason. Some Design Features Of Continuous System Modelling Program III. *INFOR: Information Systems and Operational Research*, 11(2):125–139, 1972.

R Costanza and S Gottlieb. Modelling ecological and economic systems with STELLA: Part II. *Ecological Modelling*, 112(2-3):81–84, 1998.

R Costanza and A Voinov. Modeling ecological and economic systems with STELLA: Part III. *Ecological Modelling*, 143(1-2):1–7, 2001.

R Costanza, D Duplisea, and U Kautsky. Ecological modelling and economic systems with STELLA. *Ecological Modelling*, 110(1):1–4, 1998.

Cropbox.jl. `https://github.com/cropbox/Cropbox.jl`.

Allard de Wit, Hendrik Boogaard, Davide Fumagalli, Sander J C Janssen, Rob Knapen, Daniel van Kraalingen, Iwan Supit, Raymond van der Wijngaart, and Kees van Diepen. 25 years of the WOFOST cropping systems model. *Agricultural Systems*, 168:154–167, 2019.

Jay Wright Forrester. *Industrial Dynamics*. M.I.T. Press, Cambridge, MA, 1961.

Dean P Holzworth, Val Snow, Sander J C Janssen, Ioannis N Athanasiadis, Marcello Donatelli, Gerrit Hoogenboom, Jeffrey W White, and Peter Thorburn. Agricultural production systems modelling and software: Current status and future prospects. *Environmental Modelling and Software*, 72:276–286, 2015.

Jennifer Hsiao, Kyungdahm Yun, Kyung Hwan Moon, and Soo-Hyung Kim. A process-based model for leaf development and growth in hardneck garlic (*Allium sativum*). *Annals of Botany*, 124(7):1143–1160, 2019.

Sander J C Janssen, Cheryl H Porter, Andrew D Moore, Ioannis N Athanasiadis, Ian Foster, James W Jones, and John M Antle. Towards a new generation of agricultural system data, models and knowledge products: Information and communication technology. *Agricultural Systems*, 155(C):200–212, 2017.

James W Jones, Gerrit Hoogenboom, Cheryl H Porter, Kenneth J Boote, W D Batchelor, William D Batchelor, L A Hunt, P W Wilkens, U Singh, A J Gijsman, and Joe T Ritchie. The DSSAT cropping system model. *European Journal of Agronomy*, 18(3-4): 235–265, 2003.

Soo-Hyung Kim and J. Heinrich Lieth. A coupled model of photosynthesis, stomatal conductance and transpiration for a rose leaf (*Rosa hybrida* l.). *Annals of Botany*, 91 (7):771–781, 2003.

Soo-Hyung Kim, Richard C. Sicher, Hanhong Bae, Dennis C. Gitz, Jeffrey T. Baker, Dennis J. Timlin, and Vangimalla R. Reddy. Canopy photosynthesis, evapotranspiration, leaf nitrogen, and transcription profiles of maize in response to co_2 enrichment. *Global Change Biology*, 12(3):588–600, 2006.

R Muetzelfeldt and J Massheder. The Simile visual modelling environment. *European Journal of Agronomy*, 18(3-4):345–358, 2003.

Kyaw Tha Paw U and Weigang Gao. Applications of solutions to non-linear energy budget equations. *Agricultural and Forest Meteorology*, 43(2):121–145, 1988.

C Rappoldt and Daniel van Kraalingen. The Fortran Simulation Translator FST version 2.0. Introduction and reference manual. In *Quantitative approaches in systems analysis Quantitative approaches in systems analysis Quantitative approaches in system analysis*, number 5, pages 1–178. AB-DLO, 1996.

Barry Richmond. STELLA: Software for bringing system dynamics to the other 98%. In *International Conference of the System Dynamics Society*, pages 706–718, 1985.

Andrea Schnepf, Daniel Leitner, Magdalena Landl, Guillaume Lobet, Trung Hieu Mai, Shehan Morandage, Cheng Sheng, Mirjam Zoerner, Jan Vanderborght, and Harry Vereecken. CRootBox: a structural-functional modelling framework for root systems. *Annals of Botany*, 121(5):1033–1053, 2018.

Martin K van Ittersum, P A Leffelaar, H van Keulen, M J Kropff, L Bastiaans, and J Goudriaan. On approaches and applications of the Wageningen crop models. *European Journal of Agronomy*, 18(3-4):201–234, 2003.

D. W. G. van Kraalingen, M. J. Rob Knapen, A. de Wit, and H. L. Boogaard. WISS a Java continuous simulation framework for agro-ecological modelling. In *Environmental Software Systems. Data Science in Action*, pages 242–248, 2020.

Daniel van Kraalingen. The FSE system for crop simulation. In *Simulation Reports CABO-TT*, number 23, pages 1–77. 1991.

Daniel van Kraalingen. The FSE system for crop simulation, version 2.1. In *Quantitative approaches in systems analysis*, number 1, pages 1–58. AB-DLO, 1995.

Daniel van Kraalingen and F W T Penning de Vries. The FORTRAN version of CSMP MACROS (Modules for Annual CROp Simulation). In *Simulation Reports CABO-TT*, number 21, pages 1–145. 1990.

Daniel van Kraalingen, C Rappoldt, and H H van Laar. The Fortran simulation translator, a simulation language. *European Journal of Agronomy*, 18(3-4):359–361, 2003.

Kyungdahm Yun, Dennis Timlin, and Soo-Hyung Kim. Coupled gas-exchange model for c_4 leaves comparing stomatal conductance models. *Plants*, 9(10):1358, 2020.

Chapter 2

APPLICATION I: PHENOLOGY MODEL

Abstract

Predicting phenology, the timing of developmental events, is critical for understanding how plants respond to the changing climate. Many prediction models have been developed during the last decades, but their use has been limited because of incomplete understanding of internal processes and lack of observation datasets needed for calibration and validation. Dependency on species and locations further complicates the model selection procedure which is an essential part of phenology predictions. To overcome the limitations raised by using a single model, we propose a multi-model ensemble that simplifies model selection and provides competitive performance. We hypothesize that 1) no single individual model consistently outperforms the others and 2) an ensemble model performs equally as or better than any individual models. Nine individual models based on the concept of thermal-time accumulation and their ensembles were cross-validated with 137 datasets of four temperate woody species collected from multiple locations and years in the United States and South Korea. Non-parametric tests concluded that the performance of a simple mean ensemble model was as good as the best individual model and outperformed the others. Differences between individual models were not statistically significant. The use of ensemble, however, does not preclude any bias in the interpretation caused by characteristics of the underlying models. When the ensemble was classified into groups: 1) with and 2) without chilling components, to assess spring phenology of flowering cherry species in the long-term projections, the predictions of two ensemble groups diverged considerably under RCP8.5 scenario. Our results suggest that a simple ensemble model can be a good phenology prediction tool for avoiding the pitfalls of model selection and reducing inherent uncertainties in climate change

studies, but also highlight the importance of implementing the underlying mechanisms of key physiological processes into individual models used in an ensemble.

2.1 Introduction

Temperature dictates phenology, the timing of developmental events, in plants. The relationship between temperature and plant phenology has been widely characterized by a thermal-time approach such as growing degree days. Thermal-time based phenology models are incorporated in terrestrial ecosystem models for predicting carbon and water balances at the regional and global scales in response to past and future climate scenarios [White et al., 1997, Sitch et al., 2003, Krinner et al., 2005]. For example, the vegetation dynamics determined by leaf phenology from leaf flushing to senescence accounts for much of the variabilities and uncertainties in large scale ecosystem models [Richardson et al., 2013]. Therefore, improving phenology models is critical for better predictions of global carbon and water cycles in climate change studies. In addition to the importance of leaf phenology in understanding vegetation dynamics, flowering phenology signifies developmental events that are important ecologically, evolutionarily, agriculturally, and culturally. For example, the bloom times need to be synchronized with the phenology of insect pollinators for successful reproduction and fruit production [Parmesan and Yohe, 2003, Gezon et al., 2016]. In ornamental species, the bloom time is a key consideration for plant selection in urban ecosystems especially for private and public gardens as well as cultural festivities and social events that require significant planning efforts to maximize public appreciation, engagements, and economic success [Chung et al., 2011, Miller-Rushing et al., 2007]. Similarly, accurate predictions of phenology are crucial for comprehensive crop simulation models because of the temporal dependency of developmental events in coordination with the physiological processes determining crop growth and their response to environmental stresses dictating crop yield and quality. Crop phenology also provides keys for making crop management decisions and forecasting agricultural market supply and demand.

Many models have been suggested for predicting plant phenology. A majority of the phenology models are built upon the thermal-time concept. Among these, most widely used is the growing degree days approach (GDD) that predicts the phenological events with respect to thermal accumulation above a base temperature [Richardson et al., 1975]. Conceptually similar approaches include the chilling and forcing model (CF) and the Days Transferred to Standard Temperature model (DTS). CF accounts for a two-step process to enter and release endodormancy through satisfying chilling requirement before heating units accumulate to trigger bud-burst and other phenological events in perennial species [Cesaraccio et al., 2004, Chung et al., 2011]. DTS calculates the rate of development at a given cardinal temperature which is nonlinearly described unlike GDD and CF [Ono and Konno, 1999, Hur et al., 2014]. Another approach using a simplified beta function is similar to DTS in that it calculates the developmental rate of a phenological event per unit time, but also incorporates a potential delay in warmer than optimal temperatures due to heat stress [Yan and Hunt, 1999]. The beta function approach has been adopted in crop simulation models for field crops such as maize, rice, and potato [Kim et al., 2012, Kumudini et al., 2014, Yin et al., 1995, Fleisher et al., 2006] while its use has been limited in tree phenology models. A unified model was also proposed to generalize chilling and forcing parameters for describing the response of bud growth to temperature [Chuine, 2000].

Individual models have their strengths and weaknesses depending on the processes, environmental conditions, and types of species or cultivars being simulated. An alternative approach to overcome the limitations of individual models is to use multi-model ensembles for improving predictability and quantifying uncertainties. Ensemble modeling has been used in many disciplines including biological, agricultural, and climate sciences [Mylne et al., 2002, Tao et al., 2009, Tebaldi and Knutti, 2007]. Specifically, the need for multi-model ensemble approaches for modeling crop-climate interactions has been emphasized [Rötter et al., 2011]. Recent regional and global crop modeling studies demonstrated that multi-model ensembles show better performance overall than individual models in predicting yields of multiple staple crops such as maize, wheat, and rice [Asseng et al., 2013, 2015, Bassu et al., 2014, Martre et al., 2015]. Some studies have tried to predict phenological events using an ensemble of climate change scenarios [Cook et al., 2010, Migliavacca et al., 2012, Jeong et al., 2013]. However, to our knowledge, few studies, if any, have examined an ensemble approach of multiple phenology models.

The objective of this study was to assess the ability of multi-model ensemble approaches to improve accuracy and minimize uncertainties in phenology predictions. We first evaluated the performance of existing individual models to test if any single model would outperform the rest. Then we constructed a multi-model ensemble to test whether the ensemble can better predict the flowering phenology than the individual models. Finally, we applied the ensemble to predict the flowering time in response to future climate scenarios and evaluated if an ensemble of existing phenology models could be an adequate solution for climate change studies. Nine phenological models with optimized parameter estimates were used to test the individual performance: growing degree (GD), sigmoid function (SF), beta function (BF), days transferred to standard temperature (DTS), fixed thermal period (TP), chilling and forcing (CF), sequential (SM), parallel (PM), and alternate model (AM). Five full bloom date observation datasets of cherry, apple, peach, and pear trees from multiple locations were used for parameterization and validation.

2.2 Materials and Methods

2.2.1 Observation Dataset

We compiled a large set of phenological observation data that recorded full bloom dates (FBD) of four deciduous fruit tree species from multiple locations in the United States and South Korea. Each observer might have a slightly different definition of FBD for its own use, but usually declared full bloom when more than half of the flowers were in blossom. Although the growth of fruit trees can be subject to management practices, we assumed flowering was less prone to human activities and thus driven mostly by climate variables only.

The corresponding meteorological observations were obtained from the nearest available weather stations to each location. The phenology models required temperature records in an hourly time step. When the records were missing or limited to a sub-daily resolution in some legacy datasets, such as 3 or 6 hour intervals, the existing points were linearly interpolated to generate an hourly time series.

Apple

USDA Appalachian Fruit Research Station (AFRS) collected FBD of 22 apple (*Malus pumila*) cultivars from 1997 to 2007 in Kearnesyville, WV. The closest weather station was located at Eastern West Virginia Regional Airport which is 10 km northwest of the research station.

Flowering Cherries

National Park Service (NPS) of the United States provided FBD of two flowering cherry cultivars, *Prunus* × *yedoensis* 'Yoshino' and *Prunus serrulata* 'Kwanzan', collected from Tidal Basin at Washington, D.C. from 1991 to 2010. The corresponding weather data was collected from Reagan National Airport located at 4 km south of the park.

Korea Meteorology Administration (KMA) provided FBD of another cherry variety *Prunus serrulata* var. *Spontanea* collected from 1975 to 1994 at 13 locations. The locations ranged from 33.51 to 37.75 N in latitude, 126.38 to 129.03 E in longitude, and 20.45 to 85.8 m in altitude. The weather record was available from on-site stations.

Peach and Pear

Rural Development Administration (RDA) of South Korea provided phenological and meteorological datasets for peach (*Prunus persica*) and pear (*Pyrus pyrifolia*) observed from 1981 to 2010 at 50 stations in South Korea. The locations ranged from 33.24 to 38.25 N in latitude, 124.6 to 130.8 E in longitude, and 2.2 to 772.5 m in altitude.

2.2.2 Phenology models for FBD predictions

We classified the phenology models into two groups. One group predicts the progression of phenological events as a function of temperature forcing (i.e., heat accumulation) during the current growing season. The second group of models considers the effects of temperature accumulation separately for chilling and forcing. The chilling portion is intended to account for the dormancy requirements in temperate trees. Within each group, variations exist between individual models with respect to how the forcing and chilling effects are implemented.

Forcing-only models

Growing Degrees (GD) The Growing Degree Days (GDD) is one of the most widely used models to describe a linear growth rate dependent on temperature forcing above a certain base temperature. When the weather records are limited to daily time scale, GDD often interpolates diurnal temperature from daily maximum and minimum temperatures, resulting into some variants of the method [Bonhomme, 2000, McMaster and Wilhelm, 1997]. We used growing degree hours (GDH) with hourly records to avoid such interpolation, but still described its parameters in daily scale for comparison with existing model parameters. Equation 2.1 represents our growing degree (GD) model with three parameters.

$$
\begin{aligned}
\Delta_h &= \begin{cases} \frac{1}{24}(T_h - T_b) & \text{if } T_h > T_b \\ 0 & \text{otherwise} \end{cases} \\
\sum_{h=H_s}^{\hat{H}-1} \Delta_h &< R_d \leq \sum_{h=H_s}^{\hat{H}} \Delta_h
\end{aligned}
\tag{2.1}
$$

The degree of thermal units Δ_h above a base temperature T_b stacked up towards a forcing requirement R_d in daily scale to reach full bloom date (FBD). The accumulation began at the starting date of simulation H_s expressed in hourly scale.

Sigmoid Function (SF) Instead of a linear response function in Equation 2.1, this model uses a sigmoid function to better describe the non-linearity of growth response to temperature accumulation [Fu et al., 2012]. Equation 2.2 shows a model with an additional parameter: temperature sensitivity (S_t).

$$\begin{aligned} \Delta_h &= \frac{1}{24}\Big(\frac{1}{1+\mathrm{e}^{S_t(T_h-T_b)}}\Big) \\ \sum_{h=H_s}^{\hat{H}-1} \Delta_h &< R_d \leq \sum_{h=H_s}^{\hat{H}} \Delta_h \end{aligned} \tag{2.2}$$

Beta Function (BF) The development rate of plants often continues to increase up to a certain temperature, but then declines at supra-optimal levels. A function of the beta distribution is suitable to describe such a curved response [Yin et al., 1995, Yan and Hunt, 1999]. Uni-modality of the beta function ensures maximum growth at the optimal temperature. This non-symmetrical shape allows the model to describe a gradual incline in phenological response to temperature that is followed by a rapid decline. Equation 2.3 represents a beta function with four parameters: maximum (T_x), and optimal (T_o) temperatures as well as starting date (H_s) and forcing requirement (R_d). Other parameters included in the original function were not used; maximum growth rate (R_x) was set to unity as it could be arbitrarily scaled relative to the requirement; minimum temperature (T_n) was assumed to be zero.

$$\begin{aligned} r_h &= R_x(\frac{T_x-T_h}{T_x-T_o})(\frac{T_h-T_n}{T_o-T_n})^{\frac{T_o-T_n}{T_x-T_o}} \\ \Delta_h &= \begin{cases} \frac{1}{24}r_h & \text{if } r_h > 0 \\ 0 & \text{otherwise} \end{cases} \\ \sum_{h=H_s}^{\hat{H}-1} \Delta_h &< R_d \leq \sum_{h=H_s}^{\hat{H}} \Delta_h \end{aligned} \tag{2.3}$$

Days Transferred to Standard Temperature (DTS) Given that biological events are essentially driven by chemical reactions, one could express forcing as a temperature dependent reaction rate based on the Arrehenius equation. Days transferred to standard temperature (DTS) is a modified equation with a factor weighted by standard temperature to better describe phenological observations [Ono and Konno, 1999]. Equation 2.4 represents DTS model with four parameters: standard temperature (T_s), temperature sensitivity rate (E_a), forcing requirement (R_d), and starting date (H_s). The unit of temperature values (T_h and T_s) was in Kelvin scales unlike the degree Celsius used in other models. The gas constant (R) is 8.314 J K^{-1} mol^{-1}.

$$\begin{gathered}\Delta_h = \frac{1}{24}\mathrm{e}^{\frac{E_a(T_h - T_s)}{R \cdot T_h \cdot T_s}} \\ \sum_{h=H_s}^{\hat{H}-1} \Delta_h < R_d \leq \sum_{h=H_s}^{\hat{H}} \Delta_h\end{gathered} \tag{2.4}$$

Thermal Period Fixed Model (TP) Thermal period fixed model (TP) is similar to GD except that the forcing is accumulated over a fixed time period [Nizinski and Saugier, 1988, Fu et al., 2012]. If the forcing period exceeds the threshold, the last date will be chosen to predict a full bloom (FB). If the period is less than the threshold, the next period moving one day forward would be investigated again until a satisfying period is found. Equation 2.5 represents the model with four parameters: base temperature (T_b), forcing threshold (R_d), starting date (H_s), and period length (D_n).

$$\begin{gathered}\Delta_h = \begin{cases} \frac{1}{24}(T_h - T_b) & \text{if } T_h > T_b \\ 0 & \text{otherwise} \end{cases} \\ R_d \leq \sum_{h=\hat{H}_s}^{\hat{H}_s+24D_n} \Delta_h\end{gathered} \tag{2.5}$$

Two-step models

Chilling and Forcing (CF) Cesaraccio et al. [2004] split up dormancy break into two distinctive steps, rest and quiescence, that required the same amount of chilling and subsequent anti-chilling accumulation in the opposite direction. Later this model was extended to predict FBD coming after bud burst [Chung et al., 2009, 2011]. Equation 2.6 represents our adaptation of this chilling and forcing (CF) model with three parameters: temperature threshold (T_c), chilling (R_c) and forcing (R_f) requirements. Unlike other forcing-only models, the starting date was implicitly set to October 1st of the previous year. Earlier dates are unlikely to impact model behavior much because the air temperature in September and before are mostly higher than the threshold (T_c), resulting in little or no chilling effect.

$$
\begin{aligned}
T'_h &= \begin{cases} T_h & \text{if } T_h \geq 0 \\ 0 & \text{otherwise} \end{cases} \\
\Delta_h &= \frac{1}{24}(T'_h - T_c) \\
\Delta^{\mathtt{C}}_h &= \begin{cases} \Delta_h & \text{if } \Delta_h < 0 \\ 0 & \text{otherwise} \end{cases} \\
\Delta^{\mathtt{F}}_h &= \begin{cases} \Delta_h & \text{if } \Delta_h > 0 \\ 0 & \text{otherwise} \end{cases} \\
\sum_{h=H_s}^{\hat{H}_0-1} \Delta^{\mathtt{C}}_h &> R^{\mathtt{C}}_d \geq \sum_{h=H_s}^{\hat{H}_0} \Delta^{\mathtt{C}}_h \\
\sum_{h=\hat{H}_0}^{\hat{H}-1} \Delta^{\mathtt{F}}_h &< R^{\mathtt{F}}_d \leq \sum_{h=\hat{H}_0}^{\hat{H}} \Delta^{\mathtt{F}}_h
\end{aligned}
\tag{2.6}
$$

Sequential Model (SM) The same way SF is comparable to GD, the sequential model (SM) is comparable to CF. Both CF and SM models require chilling to be met first and let forcing follow sequentially. Critical differences are that SM used a triangular response function for the chilling and a sigmoid function for the forcing [Sarvas, 1972, Hänninen, 1990, Kramer, 1994, Fu et al., 2012]. We replaced the triangular function with a beta function as they shared the same parameters. Equation 2.7 represents our sequential model with seven parameters: chilling minimum (T_n), maximum (T_x), optimum (T_o) temperatures, chilling requirement (R_c), forcing base temperature (T_b), temperature sensitivity (S_t), and forcing requirement (R_f).

$$\begin{aligned}
r_h &= (\frac{T_x - T_h}{T_x - T_o})(\frac{T_h - T_n}{T_o - T_n})^{\frac{T_o - T_n}{T_x - T_o}} \\
\Delta_h^{\mathtt{C}} &= \begin{cases} \frac{1}{24} r_h & \text{if } r_h < 0 \\ 0 & \text{otherwise} \end{cases} \\
\Delta_h^{\mathtt{F}} &= \frac{1}{24}\Big(\frac{1}{1 + \mathrm{e}^{S_t(T_h - T_b)}}\Big) \\
\sum_{h=24D_s}^{\hat{H}_0 - 1} \Delta_h^{\mathtt{C}} > R_d^{\mathtt{C}} &\geq \sum_{h=24D_s}^{\hat{H}_0} \Delta_h^{\mathtt{C}} \\
\sum_{h=\hat{H}_0}^{\hat{H} - 1} \Delta_h^{\mathtt{F}} < R_d^{\mathtt{F}} &\leq \sum_{h=\hat{H}_0}^{\hat{H}} \Delta_h^{\mathtt{F}}
\end{aligned} \tag{2.7}$$

Parallel Model (PM) The parallel model (PM) was extended from SM and allowed concurrent, as opposed to sequential, accumulation of chilling and forcing [Landsberg, 1974, Hänninen, 1990, Kramer, 1994, Fu et al., 2012]. The degree of forcing is weighted by the current degree of chilling satisfied. Only a small fraction of forcing would accumulate during earlier dates even if temperature was high enough to drive forcing. In later dates, forcing requirement could be met even under unusual warm periods retarding the chilling requirement. Equation 2.8 represents the model with a forcing weight coefficient K_m.

$$
\begin{aligned}
r_h &= (\frac{T_x - T_h}{T_x - T_o})(\frac{T_h - T_n}{T_o - T_n})^{\frac{T_o - T_n}{T_x - T_o}} \\
\Delta_h^{\mathsf{C}} &= \begin{cases} \frac{1}{24} r_h & \text{if } r_h < 0 \\ 0 & \text{otherwise} \end{cases} \\
k_h &= K_m + (1 - K_m) \frac{\sum_{i=H_s}^{h} \Delta_i^{\mathsf{C}}}{R_d^{\mathsf{C}}} \\
\Delta_h^{\mathsf{F}} &= \frac{1}{24} \Big(\frac{k_h}{1 + \mathrm{e}^{S_t (T_h - T_b)}} \Big) \\
\sum_{h=H_s}^{\hat{H}_0 - 1} \Delta_h^{\mathsf{C}} &> R_d^{\mathsf{C}} \geq \sum_{h=H_s}^{\hat{H}_0} \Delta_h^{\mathsf{C}} \\
\sum_{h=\hat{H}_0}^{\hat{H} - 1} \Delta_h^{\mathsf{F}} &< R_d^{\mathsf{F}} \leq \sum_{h=\hat{H}_0}^{\hat{H}} \Delta_h^{\mathsf{F}}
\end{aligned}
\tag{2.8}
$$

Alternating Model (AM) The alternating model (AM) is another variant of the CF model. With fixed starting dates of chilling and forcing, both units accumulate similarly to the linear response of CF. It also resembles PM that the forcing requirement is dynamically adjusted by the length of chilling period [Cannell and Smith, 1983, Murray et al., 1989, Fu et al., 2012]. Equation 2.9 represents the model with five parameters including chilling temperature (T_c) and forcing base temperature (T_b) as well as three coefficients (F_a, F_b, F_c) for forcing adjustment.

$$
\begin{aligned}
\Delta_h^{\mathtt{C}} &= \begin{cases} 1 & \text{if } T_h \leq Tc \\ 0 & \text{otherwise} \end{cases} \\
\Delta_h^{\mathtt{F}} &= \begin{cases} \frac{1}{24}(T_h - T_b) & \text{if } T_h > T_b \\ 0 & \text{otherwise} \end{cases} \\
R_h^{\mathtt{C}} &= \sum_{i=H_s^{\mathtt{C}}}^{h} \Delta_i^{\mathtt{C}} \\
R_h^{\mathtt{F}} &= a + b \cdot \mathrm{e}^{r \cdot R_h^{\mathtt{C}}} \\
\sum_{h=H_s^{\mathtt{F}}}^{\hat{H}-1} \Delta_h^{\mathtt{F}} < R_{\hat{H}-1}^{\mathtt{F}} &\leq R_{\hat{H}}^{\mathtt{F}} \leq \sum_{h=H_s^{\mathtt{F}}}^{\hat{H}} \Delta_h^{\mathtt{F}}
\end{aligned}
\tag{2.9}
$$

Mean (M)

The last model was introduced to provide a baseline for others as control. Its prediction always corresponded to the mean of observations from the calibration dataset.

$$\hat{H} = \bar{y} \tag{2.10}$$

The Multi-Model Ensemble (EN)

The multi-model ensemble combines outputs from all individual models. Equation 2.11 describes an ensemble model as a weighted mean of other models.

$$\hat{y}_{ensemble} = \sum_{m \in M} w_m \hat{y}_m \tag{2.11}$$

We constructed multiple ensemble models by choosing different combinations of weight coefficients w_m. The simplest ensemble model (EN) had an equal weight ($w_m = \frac{1}{|M|}$) proportional to the number of participating models M. We also created and tested additional ensembles that had the weight coefficients set to maximize given metrics from the calibration data. These ensembles were produced based on commonly used model performance metrics: Willmott's original index of agreement d (EN.d), modified variant d_1 (EN.d1), and refined variant d_r (EN.dr), Nash-Sutcliff efficiency E (EN.E) and modified variant E_1 (EN.E1), Watterson's M (EN.M), and Mieke-Berry's $\Re$ (EN.R), respectively [Willmott et al., 2012]. We also made an ensemble model with random forest regression to search for optimal weight coefficients from a set of predictions from individual models [Breiman, 2001]. A simple Random Forests model (EN.rf) was trained to predict an observation date with a given set of predictions from individual models. Another random forest model (EN.rf2) was additionally trained with a set of ground truth where all predictions and its observation happened to be the same. Amongst our evaluations between different ensemble methods, the simple ensemble (EN) performed equally as or better than any other ensemble methods we tested (data not shown). Thus, we use EN as the multi-model ensemble for all other tests we carried out in this study.

2.2.3 Model Calibration

Most of our models depend on piecewise functions to describe thermal units under different conditions. As the cost function was not differentiable, many local optimization methods were not applicable. We instead used a global optimization method called differential evolution (DE) to find an optimal set of parameters. DE runs with a pool of candidate solutions that are iteratively improved by random movement in the search space [Storn and Price, 1997]. Bounds of parameter values in the search space were manually specified to represent a reasonable range of biological and physical response.

2.2.4 Model Evaluation

The performance of the model was evaluated by Willmott's refined index of agreement d_r as expressed in Equation 2.12 [Willmott et al., 2012].

$$
\begin{aligned}
a &= \sum_t |\hat{y}_t - y_t| \\
b &= 2\sum_t |y_t - \bar{y}| \\
d_r &= \begin{cases} 1 - \frac{a}{b} & \text{if } a \leq b \\ \frac{b}{a} - 1 & \text{otherwise} \end{cases}
\end{aligned}
\tag{2.12}
$$

y_t is an ordinal date of observed FB at year t. $\hat{y}_t$ is a prediction by the model. $\bar{y}$ is the mean of observed dates in a given dataset for calibration.

For hypotheses testing associated with model performance evaluations, we conducted non-parametric tests over entire 137 datasets; these datasets include 2 flowering cherry data from Washington, D.C., 13 from Korean cherry, 22 from Kearneysville apple, 50 from Korean peach, and another 50 from Korean pear observations. Each dataset was randomly divided into five segments to conduct 5-fold cross-validation where four segments were used for calibration and the remaining one was saved for validation. In other words, models were subject to re-calibration with random samples for each comparison step. The evaluation metric (d_r) for each sub-dataset was ranked by its magnitude and the average rank of five sub-datasets then contributed to one measurement for Friedman test. We use non-parametric ranks instead of directly taking evaluation metric because the scores from multiple datasets are often not commensurable and also susceptible to outliers [Demsar, 2006]. Friedman test is a non-parametric counterpart of the parametric repeated measures ANOVA [Friedman, 1937, Demsar, 2006]. The average ranks of each model on 137 datasets are compared under the null hypothesis where all models are equal and thus their ranks are the same. Once Friedman test found a significant difference in the average performance ranks between the models, Nemenyi post-hoc analysis was further conducted to classify a combination of the models that had the significant difference (Figure 2.1). Nemenyi test is equivalent to the Tukey's range test for ANOVA [Nemenyi, 1963, Demsar, 2006].

Initially, only individual models were compared with each other to test if there exists a

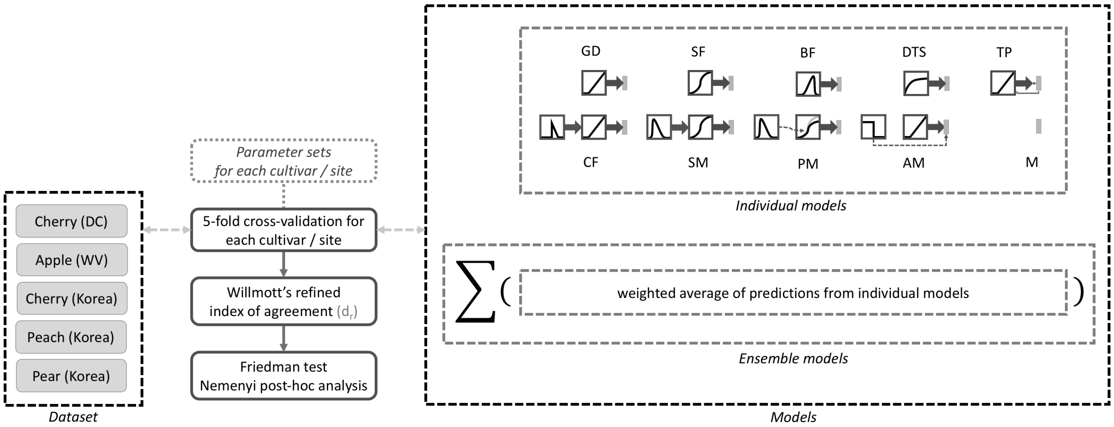

Figure 2.1: Overview of phenology model evaluation process. Individual models and their ensemble models were cross-validated with multiple datasets. Each comparison during cross-validation resulted in a score measured by Willmott's refined index of agreement (d_r) whose relative ranks among the models were then non-parametrically compared through Friedman test and Nemenyi post-hoc analysis.

single model outperforming other models. Then a simple ensemble model with equal weights (EN) was added to the group to test if EN performs better than the individual models. Lastly, ensemble models were tested without adding individual models. All statistical testing was conducted at $p = 0.01$ level unless noted otherwise.

2.2.5 Model Application

Once multi-model ensemble models were cross-validated with a large dataset under multiple comparison scenarios, the simple ensemble model (EN) was applied to the past and future conditions of a specific location to assess model agreements on phenology predictions.

The first application was to predict cherry blossom in Washington, D.C. with the existing dataset. As a previous study showed CF model was successful at predictions of Yoshino and Kwanzan cherry blossom in the same location [Chung et al., 2011], EN and CF models were deliberately chosen and compared in terms of root-mean-square error (RMSE). Both models were calibrated with 20 years of data from 1991 to 2010 and validated with 16 years of data from 1975 to 1990.

The second application was to predict cherry blossom time of the same cultivars in the same location with multiple ensemble models under future climate change scenarios. Particularly we set out to test if the models built with different physiological assumptions would reach an agreement when applied for making projections under different future climate scenarios. Three ensemble models were composed in regards with chilling dependency groups explained earlier: a sub-ensemble of forcing-only models (ENf), a sub-ensemble of chilling-based models (ENc), and the full ensemble model (EN). Two climate change scenarios, RCP4.5 and RCP8.5, were selected for representing moderate warming and extreme warming cases respectively [Pachauri et al., 2014]. Corresponding temperature projections from 2020 to 2100 were provided by MACAv2-METDATA dataset [Abatzoglou, 2013].

2.3 Results

2.3.1 Model Evaluation

Overall all models explained the variability in the observed FBD adequately. RMSE ranged from 3.5 days to 6.2 days for all models and test cases and r^2 from 0.55 and 0.85. Linear relations between phenological observations and model predictions for the entire dataset are illustrated for selected models (Figure 2.2). Samples were collected from the cross-validation conducted for non-parametric ranking test. The order of model fits indicated by r^2 and RMSE closely followed the order of performance measured by other metrics including Willmott's refined index of agreement (d_r). DTS had the highest r^2 value of 0.72 and the lowest RMSE of 4.8 days among individual models. CF was ranked slightly behind DTS despite the additional parameters included for modeling chilling process and ranked best among two-step models with r^2 value of 0.68 and RMSE of 5.3 days. EN showed better model fit than all individual models with r^2 value of 0.85 and RMSE of 3.5 days. M as the baseline control showed the lowest r^2 of 0.55 and the highest RMSE of 6.1 days.

Individual Model Comparisons

When individual models were compared, the Friedman test reported a significant difference. The subsequent Nemenyi post-hoc analysis revealed three groups of models where each group is connected by a line (Figure 2.3). The models in the same group were not significantly different from each other in terms of d_r metric ($p = 0.01$). The difference between average ranks of the models within each group was smaller than the critical difference (CD) of 1.33.

Overall there was no single model significantly better than the others. DTS was the highest average rank (4.44), followed by GD (4.82), BF (5.06), SF (5.08), CF (5.30), PM (5.71), TP (5.73), and SM (5.75). The rank difference between these eight models was not significant because it was smaller than the critical difference (1.33). AM (6.17) was not part of this group, but still not significantly different from six models except DTS and GD. M had the lowest average rank (6.94), but it was not significantly lower than AM, SM, TP, and

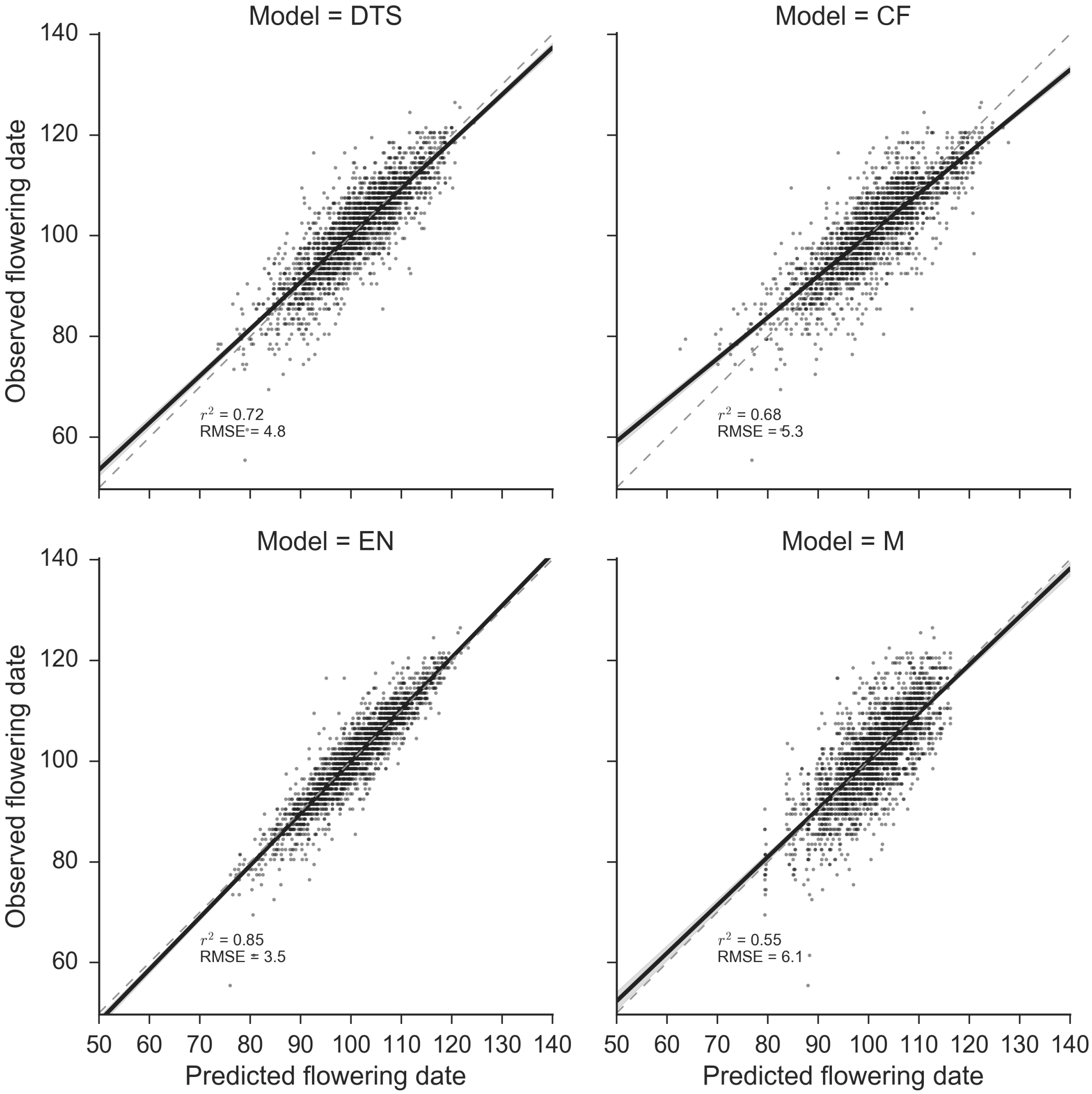

Figure 2.2: Observed vs. predicted flowering dates of the entire dataset for DTS, CF, EN, and M models. DTS was the best individual model and CF was the best among two-step models. EN was the best ensemble model and outperformed all other individual models. M as the baseline control showed the worst performance.

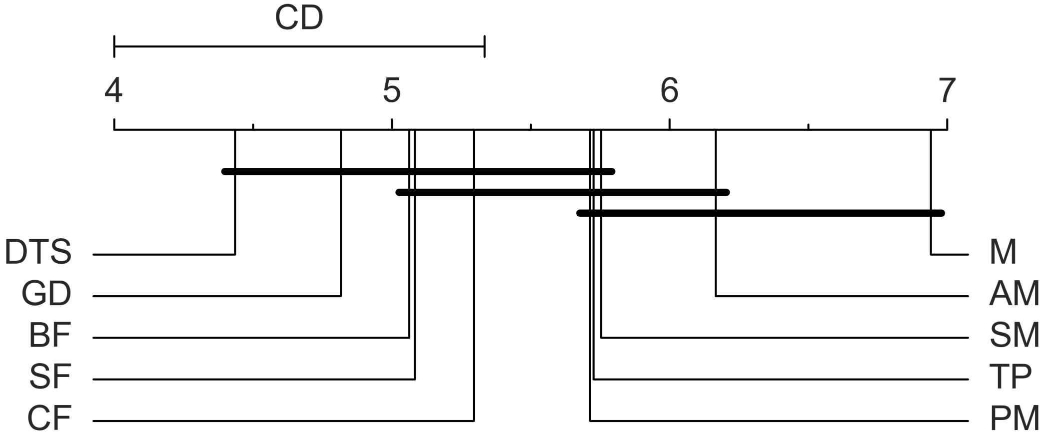

Figure 2.3: Comparison of individual models ($p = 0.01$). The models are aligned by their average ranks from cross-validation. If the rank difference between models were less than the critical difference ($CD = 1.33$), the models would be connected by a thick line to indicate non-significance. DTS had the highest average rank (4.44), but its rank was not significantly better than the following seven models.

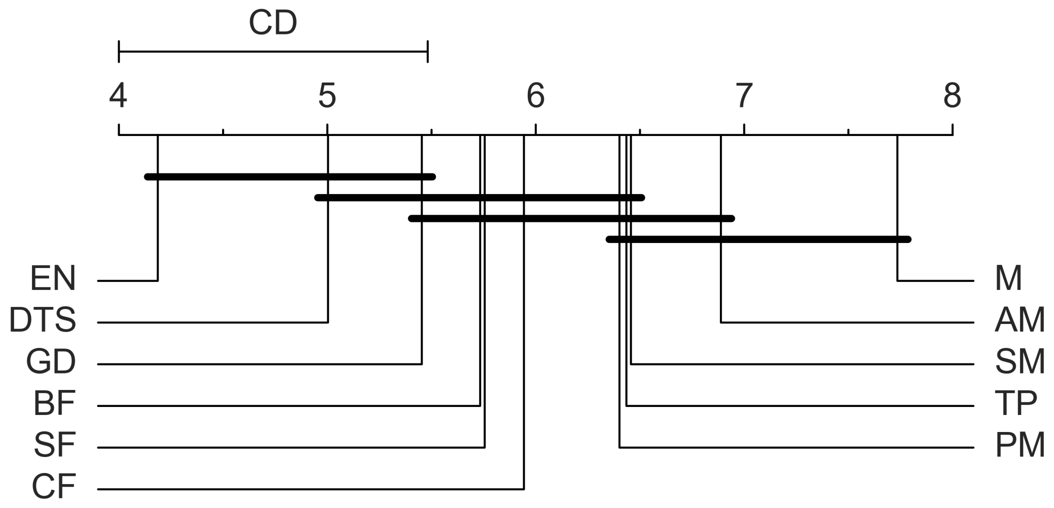

Figure 2.4: Comparison of individual and ensemble models ($p = 0.01$). The models are aligned by their average ranks from cross-validation. If the rank difference between models were less than the critical difference ($CD = 1.48$), the models would be connected by a thick line to indicate non-significance. EN had the highest average rank (4.19) followed by only DTS (5.00) and GD (5.45) within the CD.

PM.

Individual and Ensemble Model Comparisons

When individual models were compared with an ensemble model (EN), the Friedman test found a significant combination of comparisons later interpreted by Nemenyi analysis (Figure 2.4). Four groups of models were identified to perform similarly and share common lines which indicate non-significant difference in their average ranks ($p = 0.01$). When the models share the same line, the difference between average ranks of the models within each group is smaller than the critical difference (CD) of 1.48. Note that the average ranks of individual models were slightly changed but their relative positions remained the same when ensemble model was added to comparison.

There was no single model that outperformed all other models in this case either. However, EN was the highest rank (4.19) followed by only DTS (5.00) and GD (5.45) within the critical difference of 1.48. EN was significantly better than all other models except DTS and GD. The relative order of the individual models remained the same as individual models comparison.

Ensemble Model Comparisons

When ensemble models were compared, the Friedman test and subsequent Nemenyi analysis found two groups of models, but the significance was more marginal than the previous two comparisons (Figure 2.5). EN had the highest average rank (4.58), but was not significantly better than the following eight models except EN.rf which had the lowest rank (6.55). Similarly, the lower eight models except EN and EN.dr had no significant difference among them.

2.3.2 Model Application

In the first application of the ensemble model to the past prediction, FBD of Yoshino and Kwanzan cherry predicted by CF and EN was compared with actual observations in Washington, D.C. (Figure 2.6). RMSE of EN and CF with Yoshino FBD during the validation period from 1975 to 1990 was 4.8 and 7.7 days, respectively. RMSE with Kwanzan FBD was much higher, with values of 9.0 and 12.0 days, respectively. EN had a lower RMSE than CF which was the model used for predicting cherry blossom trend in the same location [Chung et al., 2011].

In the second application of the ensemble model to the future projection, FBD of Yoshino and Kwanzan cherry forecast by three ensemble models was analyzed under two future climate projections from 2020 to 2100 (Figure 2.7, 2.8).

In the RCP4.5 scenario with moderate warming of 1.8 °C on average, there was no clear distinction between sub-ensembles of chilling-based models (ENc) and forcing-only models (ENf) that both predicted similar results to the full ensemble (EN). However, in the RCP8.5

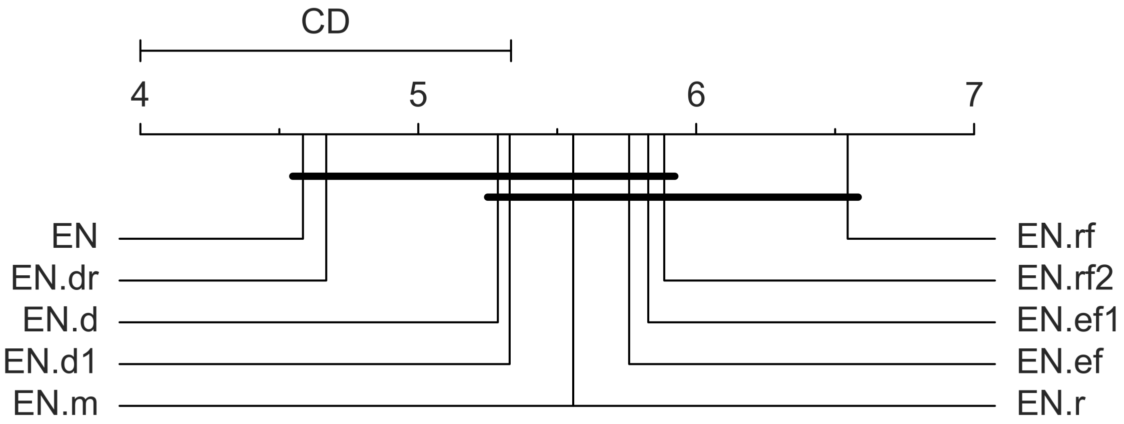

Figure 2.5: Comparison of ensemble models ($p = 0.01$). The models are aligned by their average ranks from cross-validation. If the rank difference between models were less than the critical difference ($CD = 1.33$), the models would be connected by a thick line to indicate non-significance. EN had the highest average rank (4.58), but its rank was not significantly better than the following eight models.

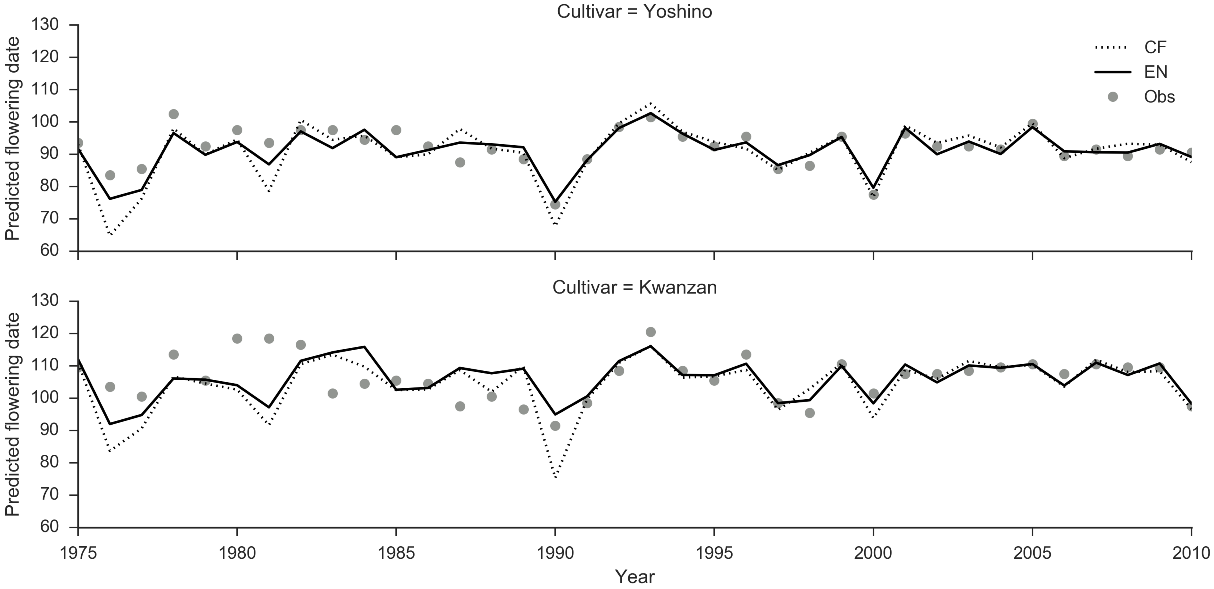

Figure 2.6: Predicted full bloom dates of Yoshino and Kwanzan cherry compared with actual observations in Washington, D.C. Both CF (chilling and forcing) and EN (ensemble) models were calibrated with 20-years of data from 1991 to 2010. RMSE was calculated from the remaining 16-years of data from 1975 to 1990. EN had lower RMSE than CF for both cultivars: 4.8 vs. 7.7 days for Yoshino; 9.9 vs 12.0 days for Kwanzan.

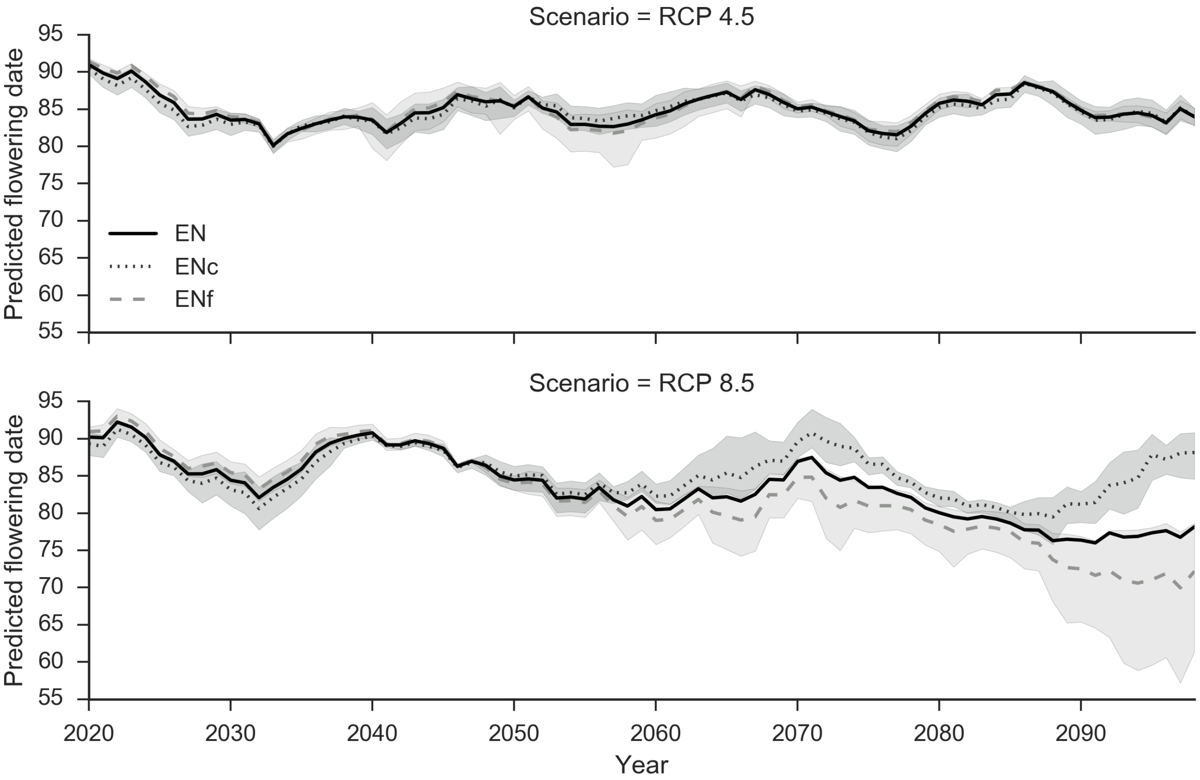

Figure 2.7: Full bloom dates of Yoshino cherry projected under future climate scenarios in Washington, D.C. Three ensemble models were used for predictions: ensemble of forcing-only models (ENf), ensemble of two-step models with chilling dependency (ENc), and full ensemble (EN). The shaded areas indicate the range of 95 % confidence intervals.

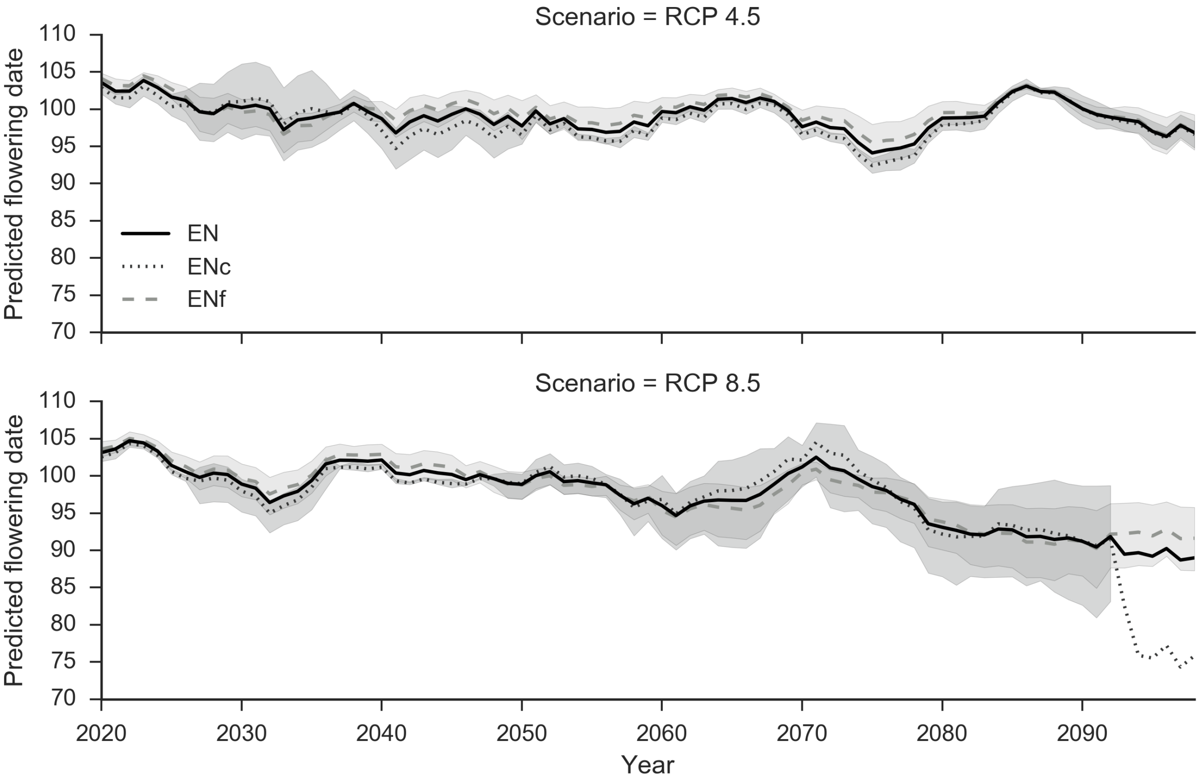

Figure 2.8: Full bloom dates of Kwanzan cherry projected under future climate scenarios in Washington, D.C. Three ensemble models were used for predictions: ensemble of forcing-only models (ENf), ensemble of two-step models with chilling dependency (ENc), and full ensemble (EN). The shaded areas indicate the range of 95 % confidence intervals. A sudden falloff after 2090s under RCP8.5 occurred by too high chilling requirements to be met under warming climate.

scenario with more extreme warming of 3.7 °C increase on average, a clear pattern of divergence between the sub-ensemble models was found.

In early-flowering Yoshino, three ensemble models showed a similar trend until 2060s, then started diverging (Figure 2.7). ENf predicted much earlier bloom whereas ENc had less sensitivity to warming temperature. After 2060s, as warming progressed, FBD forecast by ENc was apparently delayed in comparison to the prediction by ENf. In late-flowering Kwanzan, on the other hand, three models kept a more stable trend until 2090s when some chilling models started failing due to unwieldy high chilling requirements, but no diverging pattern between ENc and ENf was apparent (Figure 2.8).

2.4 Discussion

We first compared nine different phenology models for predicting flowering time of five species in 137 datasets and then again compared them with a multi-model ensemble. The ensemble model was at least as good as any individual model and showed the best average performance in our evaluation metric.

2.4.1 Individual Model Performance

There was no single best individual model that outperformed the others in all datasets. DTS had the best overall performance, but it was only significantly better than two models including a naive mean model (M) (Figure 2.3). Relatively higher rankings of the forcing-only models (DTS, GD, BF, and SF) than the chilling-dependent two-steps models was notable given that winter chilling has been recognized to play a crucial role in controlling dormancy of woody plants grown in the temperate zone [Körner and Basler, 2010, Dennis, 2003]. One reason might be due to a varying degree of chilling sensitivity particularly from late-flowering species which are less likely exposed to cold environment on flowering. They could be more affected by non-temperature variables such as photoperiod, precipitation and shading [Miller-Rushing and Primack, 2008]. Another possibility may be related to the difficulties in calibrating two-steps models with more parameters. Sub-optimal parameters for chilling process could negatively affect the overall performance of the model.

It was notable that DTS had the best performance when compared to the other forcing-only models that were based on a similar process of thermal accumulation. We speculate that its competence over other models relies on how a thermal unit is calculated from their base parameters. A mean hourly temperature is subtracted by a certain base value to define a thermal unit. DTS uses standard temperature (T_s) whereas, for example, GD uses base temperature (T_b). They are conceptually similar but there exists a critical difference that T_s defines a range of temperature in which the plants experience during the growth period, whereas T_b defines a lower limitation of temperature with which the plants can no longer continue the growth. Therefore T_s is often calibrated to a much higher value than T_b and close to the range of actual temperature observed in the dataset. This smaller gap could provide a much finer control of thermal accumulation pattern that potentially benefits DTS especially with a temperature regime mostly dominated by the forcing. Another forcing-only model, BF, uses multiple parameters, maximum (T_x) and optimal (T_o) temperatures, to define the shape of temperature response more correctly at high temperature. A careful modeling of extreme temperature regime could potentially improve predictions of summer phenology in other applications, but did not help much in our experiment because temperatures in the data mostly remained much below the estimated optimal and maximum temperatures throughout the growing season and when flowering occurs.

Chilling-based models, including CF and SM, have a potential risk of suspended forcing if chilling accumulation fails to reach the requirement before the onset of spring when no more chilling would be fulfilled. PM was not free from such unstable behaviors even though forcing was not strictly tied to chilling accomplishment. Previous studies have attempted to circumvent this issue by removing chilling enforcement after some period of time and moving onto forcing accumulation [Chung et al., 2011]. Such a procedure could eliminate some prediction failures, but also negatively affect calibration by maintaining sub-optimal parameters which otherwise would have not been selected. In our experiment, we allowed such prediction failures from chilling models and that was the reason behind a sudden change of predictions at the end of RCP8.5 projection of Kwanzan cherry blossom (Figure 2.8). Implementing alternative processes like photoperiod detection could improve prediction stability under a changing environment[Heide, 1993, Körner and Basler, 2010, Blümel and Chmielewski, 2012, Marchin et al., 2015].

2.4.2 Ensemble Model Performance

While the simple ensemble model (EN) was not always better than other models, its average performance was at least as good as the individual best model, DTS, within the current CD and significantly better than all other models. The prediction of ensemble model is primarily improved by error cancellation effect between the participating models [Hagedorn et al., 2005, Tebaldi and Knutti, 2007]. When the models produce a wide range of predictions covering a true value, their average can come close to the true value. Even when the true value is off the range of predictions, the multi-model ensemble is not inferior to other individual models, but just as worse as them. The superiority of the multi-model ensemble could be challenged by an existence of the best individual model, but identification of such a model in wide range of condition is not often feasible as we discovered in individual model comparison (Figure 2.3).

Our result also supports that ensemble models were comparable to the best single model when predicting certain variables in crop model comparison studies [Martre et al., 2015]. Simple mean and median ensembles used in Martre et al. [2015] produced similar results confirming our findings that ensemble construction methods using different metrics did not lead to a significant difference in performance. To our knowledge, applying ensemble methods for improving model predictions has not been previously reported in the phenology modeling studies.

Among multiple variations of ensemble models constructed with different weighting parameters, the simple ensemble model (EN) with equal weights was found to be the best method (Figure 2.5). It is consistent with findings in multi-model ensembles for climate projections that suggest the equal weighting scheme is safer and more transparent especially under the context of climate change [Weigel et al., 2010]. A reason behind inferior performance of more elaborate weighting parameters might be lack of more sophisticated boosting algorithms for the weight tuning process or, more likely, the scarcity of training samples both in terms of quality and quantity, which has been one of the widely known challenges for phenological research [Morisette et al., 2009]. The boosting algorithms are susceptible to noisy datasets, which is unavoidable with phenological observations, that can potentially degrade the ensemble performance in comparison to a naive approach [Long and Servedio, 2010].

2.4.3 Ensemble Model Application

As we demonstrated, the phenology ensemble models may produce better predictions than individual models, but we argue that this approach should be used only after a careful selection process for the models to be used in an ensemble. Although ensemble models generally lead to a stable prediction with lower bias as a result of averaging effects, the variances between ensemble models could remain substantially high to deserve careful interpretation of the results. We deliberately compared two ensemble model groups distinguished by inclusion of chilling-dependent processes to show the ensemble model outcomes can vary substantially with respect to the conditions with which the models are applied. A clear diverging pattern from two ensemble model groups emerged only when predicting Yoshino cherry blossom under RCP8.5 scenario of more extreme warming, whereas no difference was found with moderate RCP4.5 scenario (Figure 2.7). In high altitudes, a similar trend of spring phenology advance followed by retreat has been already reported by delayed fulfillment of chilling requirements in spite of continued warming [Yu et al., 2010]. Considering that forcing-only models performed relatively better than two-steps models on average in our individual model comparisons, a casual formulation of an ensemble with forcing-only models likely leads to contradictory outcomes in long-term predictions. The full ensemble model did not retreat as much as the chilling ensemble, but still managed to capture reduced sensitivity to the pronounced warming at the end. The discrepancy of model predictions emphasizes the importance of recognizing different characteristics of the models, understanding the underlying mechanisms, and the environments in which the models would operate.

Given contrasting climate projections and lack of mechanistic understanding of the underlying physiological process, we currently have little confidence to tell which flowering phenology projections are more probable in the future. It is known by observations that flowering in temperate trees is mostly driven by winter chilling and spring forcing with temperature modulation, but a large uncertainty remains with internal processes determining how they are triggered [Gordo and Sanz, 2010, Wu and Liu, 2013, Zhang et al., 2015]. Because dormancy break is not externally observable, chilling components tend to be empirically described with a method of many variations. Early attempts like the Utah model were designed specifically for certain species in fixed locations [Richardson et al., 1974, Anderson et al., 1986]. Later models began incorporating slightly different mechanics such as chilling unit calculation, onset determination, and chilling-forcing dependency. However, there is no consensus on the best practice of chilling model selection yet [Luedeling, 2012]. Some research reported chilling-dependent models did not perform any better than forcing-only models in the same vein as our individual model comparisons [Leinonen and Kramer, 2002, Fu et al., 2012]. Likewise, incorporating climatic variables other than temperature, such as photoperiod, precipitation and insolation, is often suggested but also open for debate due to their varying degrees of sensitivity in regards with species and locations [Körner and Basler, 2010, Chuine et al., 2010, Fu et al., 2015, Marchin et al., 2015]. Multi-model ensemble approaches do not attempt to solve these complicated issues by a single answer, but rather provide an analysis framework for possible answers with added benefits of better performance and stability [Tebaldi and Knutti, 2007]. Multi-model assessment has been frequently accomplished in many phenology studies only to select a single best model tailored to specific conditions [Kramer, 1994, Fu et al., 2012, Luedeling, 2012]. Constructing an ensemble of all available models is likely to provide better prediction performance comparable to the best individual model as we confirmed with cross-validation on multiple datasets by applying non-parametric ranking tests. Phenology predictions of higher accuracy and lower bias that avoid the pitfalls of model selection will help reducing inherent uncertainties in climate change studies.

2.5 Conclusions

In this study, we investigated if a multi-model ensemble approach can improve phenology predictions especially under the context of climate change. First, we compared nine individual models to identify a single best model which would diminish the need for multi-modeling approach and found none of the individual models outperformed the others. Then we showed their ensemble model was statistically equivalent or often better than the individual models. The multi-model ensemble approach can be a safe and effective tool in phenology prediction under climate change where great uncertainty is expected for existing models subjected to novel conditions. Yet, as the skills of such ensemble models evidently depend on the range of predictions covered by participating models, implementation of missing mechanisms to expand the coverage would be highly anticipated for future studies.

BIBLIOGRAPHY

John T Abatzoglou. Development of gridded surface meteorological data for ecological applications and modelling. *Int. J. Clim.*, 33(1):121–131, January 2013.

J L Anderson, Edmund Arlo Richardson, and C D Kesner. Validation of chill unit and flower bud phenology models for Montmorency sour cherry. *Acta Horticulturae*, 184: 71–78, May 1986.

Senthold Asseng, Frank Ewert, C Rosenzweig, J W Jones, J L Hatfield, A C Ruane, Kenneth J Boote, Peter J Thorburn, Reimund P Rötter, Davide Cammarano, Nadine Brisson, Bruno Basso, Pierre Martre, Pramod K Aggarwal, C Angulo, Patrick Bertuzzi, C Biernath, Andrew J Challinor, J Doltra, S Gayler, R Goldberg, R F Grant, L Heng, J Hooker, L A Hunt, Joachim Ingwersen, Roberto C Izaurralde, Kurt Christian Kersebaum, Christoph Mueller, Soora Naresh Kumar, Claas Nendel, Garry O'leary, Jørgen E Olesen, T M Osborne, T Palosuo, Eckart Priesack, D Ripoche, M A Semenov, Iurii Shcherbak, P Steduto, C Stoeckle, P Stratonovitch, T Streck, I Supit, Fulu Tao, Maria Travasso, Katharina Waha, Daniel Wallach, Jeffrey W White, J R Williams, and J Wolf. Uncertainty in simulating wheat yields under climate change. *Nature Climate Change*, 3(9):827–832, September 2013.

Senthold Asseng, Frank Ewert, Pierre Martre, Reimund P Rötter, David B Lobell, Davide Cammarano, Bruce A Kimball, M J Ottman, Gerard W Wall, Jeffrey W White, M P Reynolds, P D Alderman, P V Vara Prasad, Pramod K Aggarwal, J Anothai, Bruno Basso, C Biernath, Andrew J Challinor, G De Sanctis, J Doltra, E Fereres, M Garcia-Vila, S Gayler, Gerrit Hoogenboom, L A Hunt, Roberto C Izaurralde, M Jabloun, C D Jones, Kurt Christian Kersebaum, A-K Koehler, Christoph Müller, S Naresh Kumar, Claas Nendel, Garry O'leary, Jørgen E Olesen, T Palosuo, Eckart Priesack, E Eyshi Rezaei, A C Ruane, M A Semenov, Iurii Shcherbak, Claudio O Stöckle, P Stratonovitch, T Streck, I Supit, Fulu Tao, Peter J Thorburn, Katharina Waha, E Wang, Daniel Wallach, J Wolf, Z Zhao, and Y Zhu. Rising temperatures reduce global wheat production. *Nature Climate Change*, 5(2):143–147, January 2015.

Simona Bassu, Nadine Brisson, Jean-Louis Durand, Kenneth Boote, Jon I Lizaso, James W Jones, Cynthia Rosenzweig, Alex C Ruane, Myriam Adam, Christian Baron, Bruno Basso, Christian Biernath, Hendrik Boogaard, Sjaak Conijn, Marc Corbeels, Delphine Deryng, Giacomo De Sanctis, Sebastian Gayler, Patricio Grassini, Jerry Hatfield, Steven Hoek, Cesar Izaurralde, Raymond Jongschaap, Armen R Kemanian, Kurt Christian Kersebaum, Soo-Hyung Kim, Naresh S Kumar, David Makowski, Christoph Müller, Claas Nendel, Eckart Priesack, Maria Virginia Pravia, Federico Sau, Iurii Shcherbak, Fulu Tao, Edmar Teixeira, Dennis J Timlin, and Katharina Waha. How do various maize crop models vary in their responses to climate change factors? *Global Change Biol.*, 20(7):2301–2320, January 2014.

Klaus Blümel and Frank-M Chmielewski. Shortcomings of classical phenological forcing models and a way to overcome them. *Agric. For. Meteorol.*, 164:10–19, October 2012.

Raymond Bonhomme. Bases and limits to using 'degree.day' units. *European Journal of Agronomy*, 13(1):1–10, July 2000.

Leo Breiman. Random forests. *Mach Learn*, 45(1):5–32, October 2001.

M G R Cannell and R I Smith. Thermal Time, Chill Days and Prediction of Budburst in Picea-Sitchensis. *J. Appl. Ecol.*, 20(3):951–963, 1983.

Carla Cesaraccio, Donatella Spano, Richard L Snyder, and Pierpaolo Duce. Chilling and forcing model to predict bud-burst of crop and forest species. *Agric. For. Meteorol.*, 126(1-2):1–13, 2004.

Isabelle Chuine. A unified model for budburst of trees. *J. Theor. Biol.*, 207(3):337–347, 2000.

Isabelle Chuine, Xavier Morin, and Harald Bugmann. Warming, Photoperiods, and Tree Phenology. *Science*, 329(5989):277–278, 2010.

Uran Chung, Jea-Eun Jung, Hee-Cheol Seo, and Jin Il Yun. Using urban effect corrected temperature data and a tree phenology model to project geographical shift of cherry flowering date in South Korea. 93(3-4):447–463, April 2009.

Uran Chung, Liz Mack, Jin Il Yun, and Soo-Hyung Kim. Predicting the timing of cherry blossoms in Washington, DC and Mid-Atlantic States in response to climate change. *PLoS ONE*, 6(11):e27439, 2011.

Benjamin I Cook, Adam Terando, and Allison Steiner. Ecological forecasting under climatic data uncertainty: A case study in phenological modeling. *Environ. Res. Lett.*, 5(4), January 2010.

J Demsar. Statistical comparisons of classifiers over multiple data sets. *JMLR*, 7:1–30, January 2006.

F G Dennis. Problems in standardizing methods for evaluating the chilling requirements for the breaking of dormancy in buds of woody plants. *HortScience*, 38(3):347–350, June 2003.

David H Fleisher, Dennis J Timlin, Soo-Hyung Kim, and Vangimalla R Reddy. Approaches to modeling potato leaf appearance rate. *Agron. J.*, 98(3):522–528, May 2006.

Milton Friedman. The Use of Ranks to Avoid the Assumption of Normality Implicit in the Analysis of Variance. *Journal of the American Statistical Association*, 32(200): 675–701, January 1937.

Yongshuo H Fu, Matteo Campioli, Marcel Van Oijen, Gaby Deckmyn, and Ivan A Janssens. Bayesian comparison of six different temperature-based budburst models for four temperate tree species. *Ecol. Modell.*, 230:92–100, April 2012.

Yongshuo H Fu, Shilong Piao, Yann Vitasse, Hongfang Zhao, Hans J De Boeck, Qiang Liu, Hui Yang, Ulrich Weber, Heikki Hänninen, and Ivan A Janssens. Increased heat requirement for leaf flushing in temperate woody species over 1980-2012: effects of chilling, precipitation and insolation. *Global Change Biol.*, 21(7):2687–2697, January 2015.

Zachariah J Gezon, David W Inouye, and Rebecca E Irwin. Phenological change in a spring ephemeral: implications for pollination and plant reproduction. *Global Change Biol.*, 22(5):1779–1793, May 2016.

Oscar Gordo and Juan José Sanz. Impact of climate change on plant phenology in Mediterranean ecosystems. *Global Change Biol.*, 16(3):1082–1106, March 2010.

R Hagedorn, F J Doblas-Reyes, and T N Palmer. The rationale behind the success of multi-model ensembles in seasonal forecasting - I. Basic concept. 57(3):219–233, May 2005.

Heikki Hänninen. Modelling bud dormancy release in trees from cool and temperate regions. *Acta Forestalia Fennica*, 213, December 1990.

O M Heide. Daylength and Thermal Time Responses of Budburst During Dormancy Release in Some Northern Deciduous Trees. *Physiol Plantarum*, 88(4):531–540, August 1993.

Jina Hur, Joong Bae Ahn, and Kyo Moon Shim. The change of cherry first-flowering date over South Korea projected from downscaled IPCC AR5 simulation. *Int. J. Clim.*, 34(7):2308–2319, 2014.

Su-Jong Jeong, David Medvigy, Elena Shevliakova, and Sergey Malyshev. Predicting changes in temperate forest budburst using continental-scale observations and models. *Geophys. Res. Lett.*, 40(2):359–364, January 2013.

Soo-Hyung Kim, Yang Yang, Dennis J Timlin, David H Fleisher, Annette Dathe, Vangimalla R Reddy, and Kenneth Staver. Modeling Temperature Responses of Leaf Growth, Development, and Biomass in Maize with MAIZSIM. *Agron. J.*, 104(6):1523–1537, 2012.

Christian Körner and David Basler. Phenology under global warming. *Science*, 327 (5972):1461–1462, March 2010.

Koen Kramer. Selecting a Model to Predict the Onset of Growth of Fagus-Sylvatica. *J. Appl. Ecol.*, 31(1):172–181, February 1994.

G Krinner, Nicolas Viovy, Nathalie de Noblet-Ducoudré, Jérôme Ogée, Jan Polcher, Pierre Friedlingstein, Philippe Ciais, Stephen Sitch, and I Colin Prentice. A dynamic global vegetation model for studies of the coupled atmosphere-biosphere system. *Global Biogeochem. Cycles*, 19(1):1–33, March 2005.

S Kumudini, F H Andrade, Kenneth J Boote, G A Brown, K A Dzotsi, Greg O Edmeades, T Gocken, M Goodwin, A L Halter, G L Hammer, J L Hatfield, J W Jones, Armen R Kemanian, Soo-Hyung Kim, J Kiniry, Jon I Lizaso, Claas Nendel, R L Nielsen, B Parent, Claudio O Stöckle, François Tardieu, P R Thomison, Dennis J Timlin, T J Vyn, Daniel Wallach, H S Yang, and Matthijs Tollenaar. Predicting maize phenology: Intercomparison of functions for developmental response to temperature. *Agron. J.*, 106 (6):2087–2097, 2014.

J J Landsberg. Apple fruit bud development and growth: Analysis and an empirical model. *Ann. Bot.*, 38(158):1013–1023, 1974.

Ilkka Leinonen and Koen Kramer. Applications of phenological models to predict the future carbon sequestration potential of boreal forests. *Clim. Change*, 55(1-2):99–113, October 2002.

Philip M Long and Rocco A Servedio. Random classification noise defeats all convex potential boosters. *Mach Learn*, 78(3):287–304, January 2010.

Eike Luedeling. Climate change impacts on winter chill for temperate fruit and nut production: A review. *Scientia Horticulturae*, 144:218–229, September 2012.

Renée M Marchin, Carl F Salk, William A Hoffmann, and Robert R Dunn. Temperature alone does not explain phenological variation of diverse temperate plants under experimental warming. *Global Change Biol.*, 21(8):3138–3151, August 2015.

Pierre Martre, Daniel Wallach, Senthold Asseng, Frank Ewert, James W Jones, Reimund P Rötter, Kenneth J Boote, Alex C Ruane, Peter J Thorburn, Davide Cammarano, Jerry L Hatfield, Cynthia Rosenzweig, Pramod K Aggarwal, Carlos Angulo, Bruno Basso, Patrick Bertuzzi, Christian Biernath, Nadine Brisson, Andrew J Challinor, Jordi Doltra, Sebastian Gayler, Richie Goldberg, Robert F Grant, Lee Heng, Josh Hooker, Leslie A Hunt, Joachim Ingwersen, Roberto C Izaurralde, Kurt Christian Kersebaum, Christoph Müller, Soora Naresh Kumar, Claas Nendel, Garry O'leary, Jørgen E Olesen, Tom M Osborne, Taru Palosuo, Eckart Priesack, Dominique Ripoche, Mikhail A Semenov, Iurii Shcherbak, Pasquale Steduto, Claudio O Stöckle, Pierre Stratonovitch, Thilo Streck, Iwan Supit, Fulu Tao, Maria Travasso, Katharina Waha, Jeffrey W White, and Joost Wolf. Multimodel ensembles of wheat growth: Many models are better than one. *Global Change Biol.*, 21(2):911–925, January 2015.

G S McMaster and W W Wilhelm. Growing degree-days: one equation, two interpretations. *Agric. For. Meteorol.*, 87(4):291–300, 1997.

Mirco Migliavacca, O Sonnentag, Trevor F Keenan, A Cescatti, J O'Keefe, and Andrew D Richardson. On the uncertainty of phenological responses to climate change, and implications for a terrestrial biosphere model. *Biogeosciences*, 9(6):2063–2083, 2012.

Abraham J Miller-Rushing and Richard B Primack. Global warming and flowering times in Thoreau's Concord: A community perspective. *Ecology*, 89(2):332–341, February 2008.

Abraham J Miller-Rushing, Toshio Katsuki, Richard B Primack, Yukio Ishii, Sang Don Lee, and Hiroyoshi Higuchi. Impact of global warming on a group of related species and their hybrids: Cherry tree (Rosaceae) flowering at Mt. Takao, Japan. *American Journal of Botany*, 94(9):1470–1478, September 2007.

Jeffrey T Morisette, Andrew D Richardson, Alan K Knapp, Jeremy I Fisher, Eric A Graham, John T Abatzoglou, Bruce E Wilson, David D Breshears, Geoffrey M Henebry, Jonathan M Hanes, and Liang Liang. Tracking the rhythm of the seasons in the face of global change: Phenological research in the 21 st century. *Frontiers in Ecology and the Environment*, 7(5):253–260, June 2009.

M B Murray, M G R Cannell, and R I Smith. Date of budburst of fifteen tree species in Britain following climatic warming. *J. Appl. Ecol.*, 26(2):693–700, December 1989.

Kenneth R Mylne, Ruth E Evans, and Robin T Clark. Multi-model multi-analysis ensembles in quasi-operational medium-range forecasting. *Q.J.R. Meteorol. Soc.*, 128 (579):361–384, January 2002.

Peter Nemenyi. *Distribution-free multiple comparisons*. PhD thesis, 1963.

J J Nizinski and B Saugier. A model of leaf budding and development for a mature Quercus forest. *J. Appl. Ecol.*, 25(2):643–652, August 1988.

S Ono and T Konno. Estimation of flowering date and temperature characteristics of fruit trees by DTS method. *JARQ*, 33(2):105–108, April 1999.

R K Pachauri, M R Allen, V R Barros, J Broome, W Cramer, R Christ, J A Church, L Clarke, Q Dahe, P Dasgupta, N K Dubash, O Edenhofer, I Elgizouli, C B Field, P Forster, P Friedlingstein, J Fuglestvedt, L Gomez-Echeverri, S Hallegatte, G Hegerl, M Howden, K Jiang, B Jimenez Cisneroz, V Kattsov, H Lee, K J Mach, J Marotzke, M D Mastrandrea, L Meyer, J Minx, Y Mulugetta, K O'Brien, M Oppenheimer, J J Pereira, R Pichs-Madruga, G K Plattner, Hans-Otto Pörtner, S B Power, B Preston, N H Ravindranath, A Reisinger, K Riahi, M Rusticucci, R Scholes, K Seyboth, Y Sokona, R Stavins, T F Stocker, P Tschakert, D van Vuuren, and J P van Ypserle. *Climate Change 2014: Synthesis Report*. Contribution of Working Groups I, II and III to the Fifth Assessment Report of the Intergovernmental Panel on Climate Change. IPCC, Geneva, Switzerland, November 2014.

Camille Parmesan and Gary Yohe. A globally coherent fingerprint of climate change impacts across natural systems. *Nature*, 421(6918):37–42, January 2003.

Andrew D Richardson, Trevor F Keenan, Mirco Migliavacca, Youngryel Ryu, Oliver Sonnentag, and Michael Toomey. Climate change, phenology, and phenological control of vegetation feedbacks to the climate system. *Agric. For. Meteorol.*, 169:156–173, February 2013.

Edmund Arlo Richardson, S D Seely, and D R Walker. A model for estimating the completion of rest for Redhaven and Elberta peach trees. *HortScience*, 9(4):331–332, 1974.

Edmund Arlo Richardson, S D Seely, D R Walker, and J L Anderson. Pheno-climatography of spring peach bud development. *HortScience*, 10:236–237, 1975.

Reimund P Rötter, Timothy R Carter, Jørgen E Olesen, and John R Porter. Crop-climate models need an overhaul. *Nature Climate Change*, 1(4):175–177, July 2011.

R Sarvas. *Investigations on the annual cycle of development of forest trees. Active period.*, volume 76. 1972.

Stephen Sitch, B Smith, I Colin Prentice, A Arneth, A Bondeau, W Cramer, J O Kaplan, S Levis, W Lucht, M T Sykes, K Thonicke, and S Venevsky. Evaluation of ecosystem dynamics, plant geography and terrestrial carbon cycling in the LPJ dynamic global vegetation model. *Global Change Biol.*, 9(2):161–185, February 2003.

R Storn and K Price. Differential evolution - A simple and efficient heuristic for global optimization over continuous spaces. *Journal of Global Optimization*, 11(4):341–359, December 1997.

Fulu Tao, Zhao Zhang, Jiyuan Liu, and Masayuki Yokozawa. Modelling the impacts of weather and climate variability on crop productivity over a large area: A new super-ensemble-based probabilistic projection. *Agric. For. Meteorol.*, 149(8):1266–1278, August 2009.

Claudia Tebaldi and Reto Knutti. The use of the multi-model ensemble in probabilistic climate projections. *Phil. Trans. R. Soc. A*, 365(1857):2053–2075, August 2007.

Andreas P Weigel, Reto Knutti, Mark A Liniger, and Christof Appenzeller. Risks of Model Weighting in Multimodel Climate Projections. *J. Climate*, 23(15):4175–4191, 2010.

M A White, P E Thornton, and S W Running. A continental phenology model for monitoring vegetation responses to interannual climatic variability. *Global Biogeochem. Cycles*, 11(2):217–234, June 1997.

Cort J Willmott, Scott M Robeson, and Kenji Matsuura. A refined index of model performance. *Int. J. Clim.*, 32(13):2088–2094, November 2012.

Xiuchen Wu and Hongyan Liu. Consistent shifts in spring vegetation green-up date across temperate biomes in China, 1982-2006. *Global Change Biol.*, 19(3):870–880, March 2013.

Weikai Yan and L A Hunt. An equation for modelling the temperature response of plants using only the cardinal temperatures. *Ann. Bot.*, 84(5):607–614, 1999.

Xinyou Yin, Martin J Kropff, Graham McLaren, and Romeo M Visperas. A nonlinear model for crop development as a function of temperature. *Agric. For. Meteorol.*, 77 (1-2):1–16, January 1995.

Haiying Yu, Eike Luedeling, and Jianchu Xu. Winter and spring warming result in delayed spring phenology on the Tibetan Plateau. *PNAS*, 107(51):22151–22156, December 2010.

Haicheng Zhang, Wenping Yuan, Shuguang Liu, Wenjie Dong, and Yang Fu. Sensitivity of flowering phenology to changing temperature in China. *J. Geophys. Res. G: Biogeosci.*, 120(8):1658–1665, August 2015.

Chapter 3

APPLICATION II: COUPLED GAS-EXCHANGE MODEL

Abstract

Plant simulation models are abstractions of plant physiological processes that are useful for investigating the responses of plants to changes in their environment and physical structure. Photosynthesis is a basic plant process that drives growth and biomass accumulation and a basic requirement for any plant simulation model. Here, we present a coupled gas-exchange model for C_4 leaves incorporating two widely used stomatal conductance submodels: Ball–Berry and Medlyn models. The output variables of the model includes steady-state values of CO_2 assimilation rate, transpiration rate, stomatal conductance, leaf temperature, internal CO_2 concentrations, and other leaf gas-exchange attributes in response to light, temperature, CO_2, humidity, leaf nitrogen, and soil water availability. We test the model behavior and sensitivity, and discuss its applications and limitations. The model was implemented in Julia programming language using a novel modeling framework. Our testing and analyses indicate that the model behavior is reasonably sensitive and reliable in a wide range of environmental conditions. The behavior of the two model variants differing in stomatal conductance submodels deviated substantially from each other especially in low humidity conditions. The model was capable of replicating the behavior of transgenic C_4 leaves under moderate temperatures as found in the literature. The coupled model, however, underestimated stomatal conductance in very high temperatures. This is likely an inherent limitation of the coupling approaches using Ball–Berry type models in which photosynthesis and stomatal conductance are recursively linked as an input of the other.

3.1 Introduction

Leaf gas-exchange includes the processes of CO_2 assimilation and water vapor exchange by plant leaves. It is one of the most important processes for life on Earth as it provides carbohydrate for food and oxygen for respiration practically for all organisms. Because plant growth depends on photosynthesis it is an essential building block of plant simulation models. Photosynthesis models range in complexity from correlative models based on radiation use efficiency where carbon assimilation is proportional to total irradiance absorbed by leaf surfaces to models based on enzyme kinetics [Kim et al., 2019]. Integration of more mechanistic photosynthesis model has been a critical aspect in crop modeling to better understand and predict crop productivity under dynamic environments [Yin and Struik, 2009, Wu et al., 2016].

A coupled approach to modeling photosynthesis, stomatal conductance, and transpiration simultaneously for C_3 plants has been presented by a number of studies [Collatz et al., 1991, Leuning, 1995, Nikolov et al., 1995, Kim and Lieth, 2003, Tuzet et al., 2003]. This approach usually combines the FvCB (Farquhar–von Caemmerer–Berry) C_3 photosynthesis model [Farquhar et al., 1980] with a model of stomatal conductance [Ball et al., 1987, Leuning, 1995, Medlyn et al., 2011] and an energy balance equation. The coupled model approach can describe the photosynthetic behavior of leaves by taking into account the biochemical limitation for CO_2 assimilation (demand) as well as the stomatal and other biophysical limitations in CO_2 supply, linked to transpiration and leaf temperature. These models describe photosynthesis mechanistically based on its key biochemical and anatomical characteristics.

Similarly to the C_3 model, a simplified biochemical model is also available for C_4 photosynthesis that takes into account CO_2 concentrating mechanism with the anatomical and functional separation between the mesophyll and bundle sheath cells [von Caemmerer, 2000]. However, while a number of studies have adapted and applied the coupled modeling approach for C_3 leaves, its application in C_4 leaves has been limited with few exceptions [Collatz et al., 1992, Sellers et al., 1996]. An open source implementation of coupled gas-exchange modeling in R language is available with an emphasis on C_3 leaves [Duursma, 2015]. A photosynthesis model with an emphasis on plant hydraulic balance of crassulacean acid metabolism (CAM) plants is available in Python language [Hartzell et al., 2018]. Dynamic programming languages such as Python and R are often easier to use in an interactive session, but suffer from slow performance. Julia is a new dynamic programming language primarily designed for the use in scientific computing with performance in mind [Bezanson et al., 2017].

Leaf gas-exchange processes can be limited by internal and external stress factors such as leaf nitrogen and soil water availability [Sinclair and Rufty, 2012]. A process-based model should incorporate these stress responses for realistic representation of the leaf gas-exchange processes. Correlations between key enzymatic parameters and leaf nitrogen content were often derived to describe down-regulation of photosynthesis under non-optimal nitrogen availability [Medlyn et al., 1999, Vos et al., 2005, Kattge et al., 2009]. Stomatal conductance submodel was extended to acknowledge soil water status via leaf water potential and control the amount of transpiration and associated photosynthetic activity [Dewar, 2002, Vos et al., 2005, Yang et al., 2009].

Meanwhile, many existing coupled photosynthesis models have relied on an empirical relationship between photosynthesis and stomatal behavior as established by Ball, Woodrow, and Berry often referred to as Ball–Berry model [Ball et al., 1987]. Medlyn model extended Ball–Berry model in a similar structure to provide a better theoretical interpretation [Medlyn et al., 2011]. Comparisons between the two models generally reported similar performance when compared under usual conditions [Franks et al., 2017, 2018].

In this study, we developed a coupled gas-exchange model for C_4 leaves to compare performance of two stomatal conductance models: Ball–Berry (BB) and Medlyn (MED). Simulation using the two variants of coupled model were carried out under multiple environmental conditions with a varying degree of humidity, CO_2 concentration, air temperature, and irradiance. Responses to the simultaneous application of nitrogen and water stress were also investigated. Only a small number of model parameters were calibrated to an observation dataset while the most of parameter values were from existing literature and models.

An application of the model to replicate a known experiment with transgenic plants under a range of temperature is also discussed.

3.2 Materials and Methods

3.2.1 Model Structure

The gas-exchange model consists of a number of smaller submodels describing different aspect of biochemical and physical processes coupled to each other following the structure of Kim and Lieth [2003]. The C_4 photosynthesis is coupled with a stomatal conductance model via net photosynthesis rate (A_n) and also interacts with energy balance model to establish leaf temperature (T_l) [Kim et al., 2007]. We tested two stomatal conductance models, Ball–Berry model (BB) and Medlyn model (MED), combined with the rest of submodels that remained the same, yielding two variations of the gas-exchange model.

C_4 Photosynthesis

The biochemical demand for CO_2 assimilation in C_4 leaves was adapted from an existing C_4 photosynthesis model [von Caemmerer, 2000]. The rate of net CO_2 assimilation (A_n) was represented by the minimum of enzyme limited (A_c) and electron transport limited (A_j) CO_2 assimilation rates with curvature factor β.

$$A_n = \min h\{A_c, A_j, \beta\} \tag{3.1}$$

The transition between A_c and A_j was calculated using a hyperbolic minimum where $\min h\{a, b, c\}$ is equivalent to taking the lower root of quadratic equation $cx^2 - (a+b)x + ab = 0$ with curvature factor c interpreted as a parameter of co-limitation [Kirschbaum, 1994, Buckley et al., 2003]. A_c can be approximated by the minimum of phosphoenolpyruvate carboxylase (PEPC) activity (A_{c_1}) and Rubisco activity (A_{c_2}) taking into account the bundle-sheath leakage and mitochondrial respiration. A_c is driven by A_{c1} under low [CO_2] and by A_{c2} under high [CO_2].

$$A_c = \min\{A_{c_1}, A_{c_2}\} \tag{3.2}$$

$$A_{c_1} = V_p + g_{bs}C_m - R_m \tag{3.3}$$

$$A_{c_2} = V_{\text{cmax}} - R_d \tag{3.4}$$

V_p is the rate of C_4 carboxylation and assumed to be limited either by PEPC activity or PEP regeneration. g_{bs} is the bundle sheath conductance to CO_2 and C_m is the mesophyll CO_2 partial pressure. V_{cmax} is the maximum rate of Rubisco carboxylation ($\mu\text{mol}\,\text{m}^{-2}\,\text{s}^{-1}$). R_d is mitochondrial respiration in the light ($\mu\text{mol}_{CO_2}\,\text{m}^{-2}\,\text{s}^{-1}$) and half of its value was assumed a mesophyll component, R_m.

$$V_p = \min\left\{\frac{C_m V_{\text{pmax}}}{C_m + K_p}, V_{pr}\right\} \tag{3.5}$$

V_{pmax} is the maximum PEP carboxylation rate, K_p is the Michaelis-Menton constant for CO_2 of PEPC, and V_{pr} is PEP regeneration rate. Provided that the resistance for CO_2 from intercellular spaces to mesophyll cells is negligible, C_m can be estimated from CO_2 partial pressure of the air (C_a) after taking account of total leaf resistance to CO_2 (r_{v_c}) under a given A_n.

$$C_m \approx C_i = C_a - A_n r_{v_c} \tag{3.6}$$

$$r_{v_c} = r_{s_c} + r_{b_c} \tag{3.7}$$

$$r_{s_c} = \frac{1}{g_s} \cdot \left(\frac{\mathcal{D}_w}{\mathcal{D}_c}\right)^1 \tag{3.8}$$

$$r_{b_c} = \frac{1}{g_b} \cdot \left(\frac{\mathcal{D}_w}{\mathcal{D}_c}\right)^{\frac{2}{3}} \tag{3.9}$$

The ratio between diffusion coefficient for water vapor ($\mathcal{D}_w$) and CO_2 ($\mathcal{D}_c$) is used for converting from stomatal conductance (g_s) and boundary layer conductance (g_b) in terms of CO_2 into resistance in terms of water vapor (r_{s_c}, r_{b_c}). We assume g_s is subject to still air and thus raised to the power of 1 whereas g_b is subject to convective air with laminar flow and thus raised to the power of $\frac{2}{3}$ [Campbell and Norman, 1998, Jones, 2013].

C_m was solved numerically by using bisection method because its dependence on A_n which is required in the calculation of g_s forms a cyclic dependency difficult to be solved analytically.

The assimilation rate limited by electron transport (A_j) can be approximated similarly to A_c by the minimum of electron transport limited rates in C_4 and C_3 cycles.

$$A_j = \min\{A_{j_1}, A_{j_2}\} \tag{3.10}$$

$$A_{j_1} = \frac{xJ}{2} - R_m + g_{bs}C_m \tag{3.11}$$

$$A_{j_2} = \frac{(1-x)J}{3} - R_d \tag{3.12}$$

Total rate of electron transport (J) was modeled using a non-rectangular hyperbola which can be described with hyperbolic minimum (min$h$). x is a partitioning factor of J.

$$J = \min h\{I_2, J_{\max}, \theta\} \tag{3.13}$$

θ is curvature of response of electron transport to photosynthetically active radiation (PAR) and $J_{\max}$ is the maximum rate of electron transport. I_2 is effective radiation absorbed by Photosystem II (PSII) [de Pury and Farquhar, 1997, Kim and Lieth, 2003].

$$I_2 = \frac{(1-f)}{2} I_a \tag{3.14}$$

$$I_a = \alpha I \tag{3.15}$$

I is the incident light in photosynthetic photon flux density (PPFD) and I_a is PPFD absorbed by the leaf. α is leaf absorptance in PAR and assumed $1 - \delta$ where δ is the proportion of the incident light scattered by the leaf surface. f is the spectral correction factor. PAR assumes the wave band of solar radiation from 400 nm to 700 nm.

The temperature dependence of $V_{p\max}$, $V_{c\max}$, and R_d was approximated by the Arrhenius equation (k_{T_A}) normalized at a base temperature.

$$k_{T_A}[T_k, E_a] = \exp\left[\frac{E_a(T_k - T_{b_k})}{R \cdot T_k \cdot T_{b_k}}\right] \tag{3.16}$$

E_a is the activation energy varies by process, T_l is the leaf temperature and T_b is the base temperature assumed 25 °C. T_{l_k} and T_{b_k} are corresponding absolute temperatures in Kelvin (K). R is the universal gas constant. Each temperature dependent parameter has a value at 25 °C.

The temperature dependence of K_p and V_{pr} was assumed to be Q_{10} of 2.0.

$$k_{T_Q}[T] = Q_{10}^{\frac{T-T_b}{10}} \tag{3.17}$$

The temperature dependence of $J_{\max}$ was modeled using a peaked function [Medlyn et al., 2002].

$$k_{T_P}[T_k, E_a, H, S] = k_{T_A}[T_k, E_a] \cdot \left(1 + \exp\left[\frac{S \cdot T_{b_k} - H}{R \cdot T_{b_k}}\right]\right) \left(1 + \exp\left[\frac{S \cdot T_k - H}{R \cdot T_k}\right]\right)^{-1} \tag{3.18}$$

E_a and R are as defined above. H is the curvature parameter determining the rate of decrease above the peak temperature and S is the entropy factor.

Nitrogen dependence of $V_{p\max}$, $V_{c\max}$, and $J_{\max}$ was modeled by a logistic function for the current leaf nitrogen content (N) [Vos et al., 2005]. N_0 is a baseline value assumed for the leaf nitrogen content and s is the steepness of nitrogen response curve.

$$k_N = \frac{2}{1 + \exp[-s \cdot \max\{N_0, N\} - N_0]} - 1 \tag{3.19}$$

Temperature dependence (k_T) and nitrogen dependence (k_N) are multiplicative limiting factors. For example, electron transport rate ($V_{p\max}$) is scaled from $V_{p\max_{25}}$ by calculating $V_{p\max} = V_{p\max_{25}} \cdot k_{T_A}[T_l, E_{ap}] \cdot k_N$ with the current leaf temperature (T_l) and an activation energy for PEPC (E_{ap}).

Boundary Layer Conductance

Boundary layer conductance to water vapor (g_b) was derived from convective heat conductance of the leaf surface (g_H). Corresponding Nusselt number ($\mathtt{Nu}$) and Reynolds Number ($\mathtt{Re}$) were derived by assuming forced convection of streamline flow on flat plates [Monteith and Unsworth, 2014]. u is wind speed ($\mathrm{m\,s^{-1}}$) and d is characteristic dimension of the leaf determined by leaf width W (cm) [Campbell and Norman, 1998]. $\mathcal{D}_m$ is kinematic viscosity of the air and $\mathcal{D}_h$ is thermal diffusivity of the air. $\mathcal{D}_m$ and $\mathcal{D}_h$ were assumed temperature independent at 20 °C.

$$g_H = \frac{\mathcal{D}_h \cdot \mathtt{Nu}}{d} \tag{3.20}$$

$$\mathtt{Nu} = 0.60\sqrt{\mathtt{Re}} \tag{3.21}$$

$$\mathtt{Re} = \frac{u \cdot d}{\mathcal{D}_m} \tag{3.22}$$

$$d = 0.72w \tag{3.23}$$

g_H ($\mathrm{m\,s^{-1}}$) is then scaled and converted to g_h ($\mathrm{mmol\,m^{-2}\,s^{-1}}$) using the Gas Laws [Monteith and Unsworth, 2014]. T_{a_k} is the absolute temperature of air (K).

$$g_h = g_H \cdot \frac{P_a}{R \cdot T_{a_k}} \tag{3.24}$$

g_b was then derived from g_h using a diffusion ratio between water vapor and heat transfer under forced convection [Campbell and Norman, 1998, Jones, 2013]. Additionally, g_b was normalized to the current atmospheric pressure (P_a) to make its units explicitly expressed in vapor pressure gradient rather than in unitless mole fraction.

$$g_b = \frac{g_h}{P_a} \cdot \left(\frac{\mathcal{D}_w}{\mathcal{D}_h}\right)^{\frac{2}{3}} \tag{3.25}$$

Stomatal Conductance

We used two approaches for modeling stomatal conductance (g_s). $g_{s_{\mathrm{BB}}}$ is stomatal conductance following Ball–Berry (BB) model [Ball et al., 1987] and $g_{s_{\mathrm{MED}}}$ follows Medlyn (MED) model [Medlyn et al., 2011].

$$g_{s_{\mathrm{BB}}} = g_{0_{\mathrm{BB}}} + g_{1_{\mathrm{BB}}} \frac{h_s A_n}{C_s} f_{\Psi_v} \tag{3.26}$$

$g_{0_{\mathrm{BB}}}$ ($\mathrm{mol_{H_2O}\,m^{-2}\,s^{-1}\,bar^{-1}}$) is residual stomatal conductance to water vapor at the light compensation point and $g_{1_{\mathrm{BB}}}$ is the empirical coefficient for the sensitivity of g_s to other variables. h_s is relative humidity at the leaf surface (as a fraction), A_n is net photosynthesis, and P_a is the partial pressure of the air.

f_{Ψ_v} is a weight factor that adjusts stomatal conductance to the bulk leaf water potential (Ψ_v) where Ψ_f is a reference potential and s_f is a sensitivity parameter [Tuzet et al., 2003].

$$f_{\Psi_v} = \frac{1 + \exp[s_f \Psi_f]}{1 + \exp[s_f(\Psi_f - \Psi_v)]} \tag{3.27}$$

$g_{s_{\mathrm{MED}}}$ has a slightly different form compared to $g_{s_{\mathrm{BB}}}$ that uses vapor pressure deficit at the leaf surface (D_s) instead of h_s. $g_{0_{\mathrm{MED}}}$ ($\mathrm{mol_{H_2O}\,m^{-2}\,s^{-1}\,bar^{-1}}$) has the same meaning as $g_{0_{\mathrm{BB}}}$ setting a lower bound of the conductance value. $g_{1_{\mathrm{MED}}}$ is similarly a sensitivity parameter, but in different units ($\sqrt{\mathrm{kPa}}$) and scale.

$$g_{s_{\mathrm{MED}}} = g_{0_{\mathrm{MED}}} + \left(1 + \frac{g_{1_{\mathrm{MED}}}}{\sqrt{D_s}}\right) \frac{A_n}{C_s} f_{\Psi_v} \tag{3.28}$$

In both models, C_s is $\mathrm{CO_2}$ partial pressure at the leaf surface after taking account of boundary layer resistance to $\mathrm{CO_2}$ (r_{b_c}) under a given A_n.

$$C_s = C_a - A_n r_{b_c} \tag{3.29}$$

h_s in Ball–Berry model was obtained by solving an equation connecting diffusion pathways of boundary layer and stomatal interface. h_a is relative humidity in the air. Humidity inside the intercellular space was assumed fully saturated. The resultant Equation 3.30 is quadratic since $g_{s_{\mathrm{BB}}}$ has h_s in its component as defined in Equation 3.26.

$$(h_s - h_a)g_b = (1 - h_s)g_{s_{\mathrm{BB}}} \tag{3.30}$$

D_s in Medlyn model was obtained in a similar way. Water vapor pressure at the leaf surface (w_s), in the air (w_a), and in the intercellular space (w_i) were used instead of relative humidity values. The resultant Equation 3.31 is quadratic since $g_{s_{\mathrm{MED}}}$ has D_s in its component as defined in Equation 3.28. In an actual implementation, the equation was solved in terms of $\sqrt{D_s}$ and squared later to cope with a symbolic equation solver internally used by our framework.

$$(w_s - w_a)g_b = (w_i - w_s)g_{s_{\mathrm{MED}}} \tag{3.31}$$

Energy Balance

Leaf temperature (T_l) can be different from air temperature (T_a) due to energy balancing on the leaf surface.

$$T_l = T_a + \Delta T \tag{3.32}$$

The temperature difference (ΔT) is obtained by numerically solving the energy budget equation.

$$R_n - H - \lambda E = 0 \tag{3.33}$$

The equation indicates that the net radiation absorbed by the leaf (R_n) should equal to the loss by sensible heat flux (H) and latent heat flux (λE), assuming no heat is stored in the leaf.

$$R_n = R_{sw} + R_{lw} \tag{3.34}$$

$$R_{sw} = \alpha_s k I \tag{3.35}$$

$$R_{lw} = 2\epsilon\sigma(T_{a_k}^4 - T_{l_k}^4) \tag{3.36}$$

The absorbed net radiation (R_n) is composed of shortwave component driven by solar radiation (R_{sw}) and longwave component via thermal radiation (R_{lw}). Note that we assumed gas-exchange measured inside a small chamber and the temperature of chamber wall was equivalent to the surrounding air. α_s is absorption coefficient of the leaf for solar radiation and ϵ is thermal emissivity of the leaf. σ is Stefan–Boltzmann constant.

$$H = C_p g_h \Delta T \tag{3.37}$$

For the sensible heat flux (H), C_p is specific heat of air and g_h is the convective heat conductance of the leaf surface.

$$E = g_v \Delta w \tag{3.38}$$

$$g_v = \frac{1}{\dfrac{1}{g_s} + \dfrac{1}{g_b}} \tag{3.39}$$

$$D = e_s[T_l] - e_a \tag{3.40}$$

For the latent heat flux (λE), λ is the latent heat of vaporization for water. E is the transpiration rate calculated with leaf conductance (g_v) and vapor pressure gradient between leaf surface and the air (Δw). e_a is ambient vapor pressure of air. e_s is saturated vapor pressure at a given temperature (T).

$$e_s[T] = 0.611 \cdot \exp\left[\frac{17.502 \cdot T}{240.97 + T}\right] \tag{3.41}$$

Coupling Submodels

The net photosynthetic rate (A_n) depends on mesophyll [CO$_2$] ($C_m \approx C_i$) through Equations 3.2 and 3.10. C_i depends on stomatal conductance (g_s) through Equation 3.6. g_s then again depends on A_n through Equations 3.26 and 3.28, forming a cyclic dependency solved by an iterative numerical method. In the meantime, many parameters for A_n depends on temperature that the temperature of biochemical reaction site (T_l) should play an important role. Vapor pressure of intercellular space (pi) used for Medlyn stomatal conductance model can also change with T_l. The latent heat component of Equation 3.33 solved for T_l is then driven by leaf conductance (g_v) which depends on g_s through Equation 3.39.

Therefore, three submodels for photosynthesis, stomatal conductance, and energy balance are interdependent. We used a nested iterative procedure using the bisection method to solve this relation numerically. For initial condition, each variable was given a sensible range of minimum and maximum values. C_i was assumed to be at least 0 µbar and lower than two times of C_a. ΔT, the difference between leaf temperature (T_l) and air temperature (T_a), was assumed in the range of -10 K and 10 K.

Implementation

An early version of the model was implemented in Delphi which was later converted to C++ and released as a sample of peer-reviewed publication of computer code [Timlin et al., 2016]. Then the model was translated, calibrated, and visualized with Cropbox framework [Cropbox.jl] written in Julia programming language [Bezanson et al., 2017]. In this framework, a small component of the model is encapsulated into a structure called system and each system is a collection of variables described in a declarative form which closely resembles mathematical equations defined above and specifications of variables and parameters (Table 3.1, 3.2). The gas-exchange model was composed of 23 systems including a submodel for stomatal conductance (Figure 3.1).

The framework provides a number of unique types of variable declaration that can help

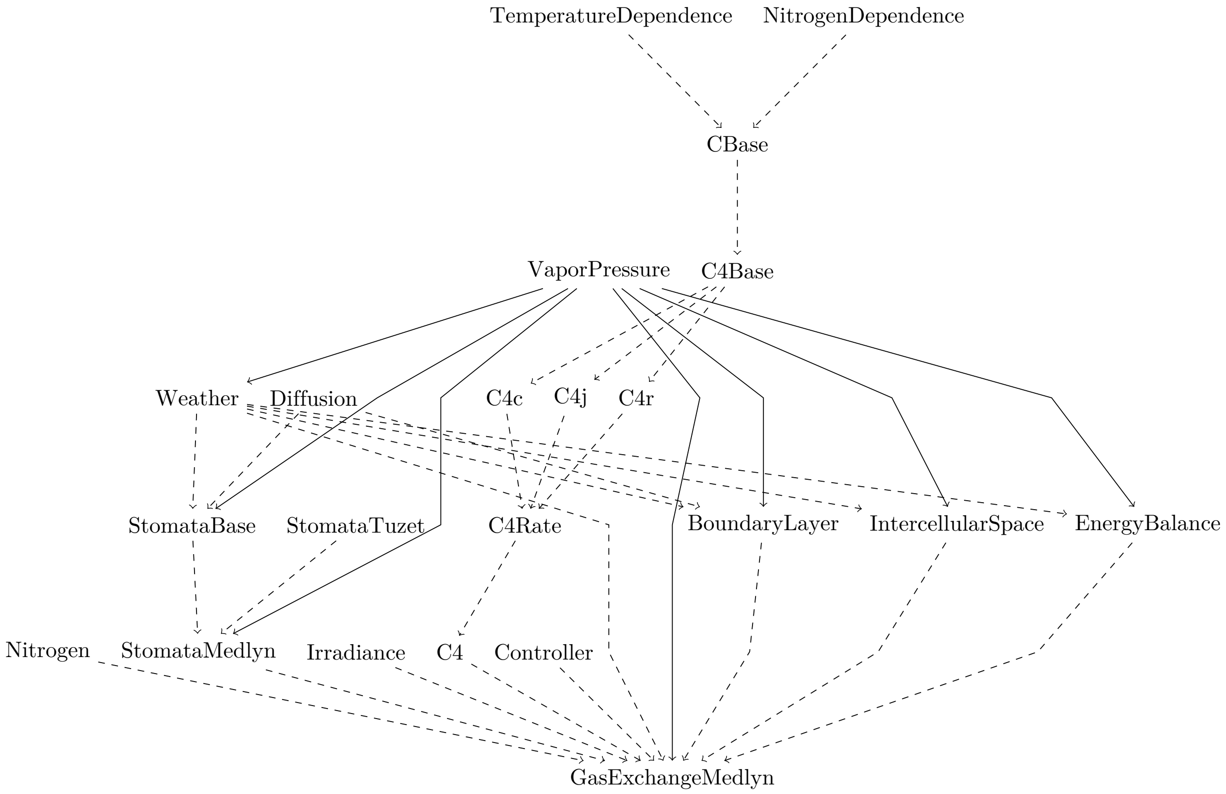

Figure 3.1: System diagram of the gas-exchange model (`GasExchangeMedlyn`) incorporating several submodels including Medlyn stomatal conductance model implemented on Cropbox framework. Solid arrow indicates 'has' relationship that the entity pointed out by the arrow owns the other entity and takes responsibility of state updates. Dashed arrow indicates 'is' relationship that the pointing entity becomes a trait of the other entity at the end.

hiding complexity of implementation details. For example, h_s in Equation 3.30 is declared as a `solve` variable which is automatically expanded and solved in terms of symbolic algebra. ΔT in Equation 3.32 in conjunction with Equation 3.33 is declared as a `bisect` variable which would automatically generate necessary code to implement a nested iterative solver as described in Appendix 3.2.1. An optimal value of ΔT that satisfies $R_n = H + \lambda E$

as Equation 3.33 would be found out by applying bisection method (Figure 3.2). Given Equation 3.6 was also implemented as a `bisect` variable, the framework would analyze dependency between variables and generate proper code for nested structure.

```
@system EnergyBalance(Weather) begin
  ..
  ϵ: leaf_thermal_emissivity ⇒ 0.97 ~ preserve(parameter)
  σ: stefan_boltzmann_constant ⇒ u"σ" ~ preserve(u"W/m^2/K^4")
  λ: latent_heat_of_vaporization_at_25 ⇒ 44 ~ preserve(u"kJ/mol", parameter)
  Cp: specific_heat_of_air ⇒ 29.3 ~ preserve(u"J/mol/K", parameter)

  Δw(T, T_air, RH, ea=vp.ambient, es=vp.saturation): leaf_vapor_pressure_gradient ⇒ begin
      es(T) - ea(T_air, RH)
  end ~ track(u"kPa")
  E(gv, Δw): transpiration ⇒ gv*Δw ~ track(u"mmol/m^2/s")

  H(Cp, gh, ΔT): sensible_heat_flux ⇒ Cp*gh*ΔT ~ track(u"W/m^2")
  λE(λ, E): latent_heat_flux ⇒ λ*E ~ track(u"W/m^2")

  ΔT(R_net, H, λE): temperature_adjustment ⇒ begin
      R_net == H + λE
  end ~ bisect(lower=-10, upper=10, u"K", evalunit=u"W/m^2")

  T(T_air, ΔT): leaf_temperature ⇒ (T_air + ΔT) ~ track(u"°C")
  Tk(T): absolute_leaf_temperature ~ track(u"K")
end
```

Figure 3.2: Snippet of model code implementing energy balance process.

Note that all equations described in this section assume implicit units conversion and scaling which is a feature provided by Cropbox framework. For example, in Equation 3.23, leaf width W was declared in 'cm' then automatically scaled to match the units of final product in 'm' that an actual code generated for calculating characteristic dimension was $d = 0.72 \left(w \cdot 0.01 \, \frac{\mathrm{m}}{\mathrm{cm}} \right)$.

Table 3.1: Variables declared in the coupled gas-exchange model.

Symbol	**Units**	**Description**
$\mathrm{C_4}$ Photosynthesis		
A_c	$\mathrm{\mu mol_{CO_2}\,m^{-2}\,s^{-1}}$	Rubisco-limited $\mathrm{CO_2}$ assimilation rate
A_j	$\mathrm{\mu mol_{CO_2}\,m^{-2}\,s^{-1}}$	Electron transport-limited $\mathrm{CO_2}$ assimilation rate
A_n	$\mathrm{\mu mol_{CO_2}\,m^{-2}\,s^{-1}}$	Net photosynthesis rate

Continued

Symbol	Units	Description
C_a	µbar	Atmospheric CO_2 partial pressure*
C_i	µbar	Intercellular CO_2 partial pressure
C_m	µbar	Mesophyll CO_2 partial pressure
J	$\mu mol_{electrons}\,m^{-2}\,s^{-1}$	Electron transport rate
J_{max}	$\mu mol_{electrons}\,m^{-2}\,s^{-1}$	Maximum rate of electron transport
k_N	-	Nitrogen dependence
k_{T_A}	-	Temperature dependence by Arrhenius equation
k_{T_Q}	-	Temperature dependence by Q_{10} function
k_{T_P}	-	Temperature dependence by a peaked function
K_c	µbar	Michaelis-Menton constant of Rubisco for CO_2
K_p	µbar	Michaelis-Menton constant of PEPC for CO_2
N	$g\,m^{-2}$	Leaf nitrogen content
N_p	%	Relative leaf nitrogen content assuming SLA $= 200\,cm^2\,g^{-1}$
P_a	kPa	Atmospheric pressure*
R_d	$\mu mol_{CO_2}\,m^{-2}\,s^{-1}$	Mitochondrial respiration rate
r_{v_c}	$m^2\,s\,mol_{CO_2}^{-1}\,bar$	Total leaf resistance to CO_2
T_a	°C	Air temperature in Celsius*
T_{a_k}	K	Air temperature in Kelvin
T_l	°C	Leaf temperature in Celsius
T_{l_k}	K	Leaf temperature in Kelvin
V_p	$\mu mol_{CO_2}\,m^{-2}\,s^{-1}$	C_4 carboxylation rate
V_{pr}	$\mu mol_{CO_2}\,m^{-2}\,s^{-1}$	PEP regeneration rate
V_{cmax}	$\mu mol_{CO_2}\,m^{-2}\,s^{-1}$	Maximum rate of Rubisco carboxylation
V_{pmax}	$\mu mol_{CO_2}\,m^{-2}\,s^{-1}$	Maximum rate of C_4 carboxylation
Irradiance		
I	$\mu mol_{quanta}\,m^{-2}\,s^{-1}$	Incident PAR*
I_a	$\mu mol_{quanta}\,m^{-2}\,s^{-1}$	Absorbed PAR
I_2	$\mu mol_{quanta}\,m^{-2}\,s^{-1}$	Effective PAR
Boundary Layer		
d	m	Leaf characteristic dimension

Continued

Symbol	**Units**	**Description**
g_b	$\text{mol}_{\text{H}_2\text{O}}\,\text{m}^{-2}\,\text{s}^{-1}\,\text{bar}^{-1}$	Boundary layer conductance to water vapor
g_h	$\text{mmol}\,\text{m}^{-2}\,\text{s}^{-1}$	Leaf convective heat conductance in molar flux
g_H	$\text{m}\,\text{s}^{-1}$	Leaf convective heat conductance
r_{b_c}	$\text{m}^2\,\text{s}\,\text{mol}_{\text{CO}_2}^{-1}\,\text{bar}$	Boundary layer resistance to CO_2
u	$\text{m}\,\text{s}^{-1}$	Wind speed*
Stomatal Conductance		
D_s	kPa	Vapor pressure deficit at the leaf surface
f_{Ψ_v}	-	Water stress factor
g_s	$\text{mol}_{\text{H}_2\text{O}}\,\text{m}^{-2}\,\text{s}^{-1}\,\text{bar}^{-1}$	Stomatal conductance to water vapor
$g_{s_{\text{BB}}}$	$\text{mol}_{\text{H}_2\text{O}}\,\text{m}^{-2}\,\text{s}^{-1}\,\text{bar}^{-1}$	Stomatal conductance to water vapor from Ball–Berry model
$g_{s_{\text{MED}}}$	$\text{mol}_{\text{H}_2\text{O}}\,\text{m}^{-2}\,\text{s}^{-1}\,\text{bar}^{-1}$	Stomatal conductance to water vapor from Medlyn model
RH	%	Relative humidity of the air (0–100)
h_a	-	Relative humidity of the air (0–1)
h_s	-	Relative humidity at the leaf surface (0–1)
w_a	kPa	Water vapor pressure in the air
w_i	kPa	Water vapor pressure in the intercellular space
w_s	kPa	Water vapor pressure at the leaf surface
Ψ_v	MPa	Bulk leaf water potential
r_{s_c}	$\text{m}^2\,\text{s}\,\text{mol}_{\text{CO}_2}^{-1}\,\text{bar}$	Stomatal resistance to CO_2
Energy Balance		
Δw	kPa	Vapor pressure gradient between leaf surface and the air
e_a	kPa	Vapor pressure in the ambient air
e_s	kPa	Saturated vapor pressure
E	$\text{mmol}_{\text{H}_2\text{O}}\,\text{m}^{-2}\,\text{s}^{-1}$	Transpiration rate
g_v	$\text{mol}_{\text{H}_2\text{O}}\,\text{m}^{-2}\,\text{s}^{-1}\,\text{bar}^{-1}$	Total leaf conductance to water vapor
H	$\text{W}\,\text{m}^{-2}$	Sensible heat flux
λE	$\text{W}\,\text{m}^{-2}$	Latent heat flux
R_n	$\text{W}\,\text{m}^{-2}$	Net radiation absorbed
ΔT	K	Temperature difference between T_l and T_a

* Input variables to the model (Table 3.3).

Table 3.2: Parameters and constants used in the coupled gas-exchange model.

Symbol	**Value**	**Units**	**Description**
C_4 Photosynthesis			
β	0.99	-	Sharpness of transition between A_c and A_j
E_{ac}	55.9[1]	$\mathrm{kJ\,mol^{-1}}$	Activation energy for $V_{c\max}$
E_{aj}	32.8†	$\mathrm{kJ\,mol^{-1}}$	Activation energy for $J_{\max}$
E_{ap}	75.1†	$\mathrm{kJ\,mol^{-1}}$	Activation energy for $V_{p\max}$
E_{ar}	39.8†	$\mathrm{kJ\,mol^{-1}}$	Activation energy for R_d
g_{bs}	0.003[2]	$\mathrm{mol_{CO_2}\,m^{-2}\,s^{-1}\,bar^{-1}}$	Bundle-sheath conductance to CO_2
H_j	220[3]	$\mathrm{kJ\,mol^{-1}}$	Curvature parameter for $J_{\max}$
$J_{\max_{25}}$	300†	$\mathrm{\mu mol_{electrons}\,m^{-2}\,s^{-1}}$	Maximum rate of electron transport at 25 °C
$K_{c_{25}}$	650[2]	µbar	Michaelis-Menton constant of Rubisco for CO_2 at 25 °C
$K_{p_{25}}$	80[2]	µbar	Michaelis-Menton constant of PEPC for CO_2 at 25 °C
N_0	0.343*	$\mathrm{g\,m^{-2}}$	Baseline leaf nitrogen content
R	8.314	$\mathrm{J\,K^{-1}\,mol^{-1}}$	Universal gas constant
$R_{d_{25}}$	2[3]	$\mathrm{\mu mol_{CO_2}\,m^{-2}\,s^{-1}}$	Mitochondrial respiration rate at 25 °C
s	4.191*	$\mathrm{m^2\,g^{-1}}$	Steepness of nitrogen response curve
S_j	702.6†	$\mathrm{J\,mol^{-1}\,K}$	Entropy factor for $J_{\max}$
θ	0.5†	-	Sharpness of transition between light limitation and saturation
T_b	25	°C	Base temperature in Celsius
T_{b_k}	298.15	K	Base temperature in Kelvin
$V_{c\max_{25}}$	50†	$\mathrm{\mu mol_{CO_2}\,m^{-2}\,s^{-1}}$	Maximum rate of Rubisco carboxylation at 25 °C
$V_{p\max_{25}}$	70†	$\mathrm{\mu mol_{CO_2}\,m^{-2}\,s^{-1}}$	Maximum rate of PEP carboxylation at 25 °C
$V_{pr_{25}}$	80[2]	$\mathrm{\mu mol_{CO_2}\,m^{-2}\,s^{-1}}$	PEP regeneration rate at 25 °C
x	0.4[2]	-	Partitioning factor of electron transport rate
Irradiance			
α	0.85[4]	-	Leaf absorptance in PAR
δ	0.15[5]	-	Leaf scattering factor
f	0.15[5]	-	Leaf spectral correction factor

Continued

Symbol	**Value**	**Units**	**Description**
Boundary Layer			
$\mathcal{D}_w$	24.2	$\mathrm{mm^2\,s^{-1}}$	Diffusion coefficient for water vapor in air at 20 °C
$\mathcal{D}_c$	14.7	$\mathrm{mm^2\,s^{-1}}$	Diffusion coefficient for CO_2 in air at 20 °C
$\mathcal{D}_h$	21.5	$\mathrm{mm^2\,s^{-1}}$	Diffusion coefficient for heat (thermal diffusivity) in air at 20 °C
$\mathcal{D}_m$	15.1	$\mathrm{mm^2\,s^{-1}}$	Diffusion coefficient for momentum (kinematic viscosity) in air at 20 °C
W	10	cm	Leaf width
Stomatal Conductance			
$g_{0_{\mathrm{BB}}}$	0.036*	$\mathrm{mol_{H_2O}\,m^{-2}\,s^{-1}\,bar^{-1}}$	Lower bound of $g_{s_{\mathrm{BB}}}$
$g_{1_{\mathrm{BB}}}$	2.792*	-	Sensitivity of $g_{s_{\mathrm{BB}}}$
$g_{0_{\mathrm{MED}}}$	0.031*	$\mathrm{mol_{H_2O}\,m^{-2}\,s^{-1}\,bar^{-1}}$	Lower bound of $g_{s_{\mathrm{MED}}}$
$g_{1_{\mathrm{MED}}}$	1.281*	$\sqrt{\mathrm{kPa}}$	Sensitivity of $g_{s_{\mathrm{MED}}}$
Ψ_f	-2.0	MPa	Reference water potential
s_f	2.3[6]	$\mathrm{MPa^{-1}}$	Sensitivity of water response
Energy Balance			
α_s	0.79[7]	-	Radiation absorption coefficient of the leaf
C_p	29.3	$\mathrm{J\,mol^{-1}\,K^{-1}}$	Specific heat of air
ϵ	0.97[8]	-	Leaf thermal emissivity
k	0.22	$\mathrm{J\,\mu mol^{-1}}$	Radiation conversion factor
λ	44	$\mathrm{kJ\,mol^{-1}}$	Latent heat of vaporization at 25 °C
σ	5.670×10^{-8}	$\mathrm{W\,m^{-2}\,K^{-4}}$	Stefan–Boltzmann constant

* Parameter values calibrated in this paper.

† Parameter values calibrated with a dataset from [Kim et al., 2012].

[1] [Sage, 2002]

[2] [von Caemmerer, 2000]

[3] [Kim et al., 2007]

[4] [Jones, 2013]

[5] [de Pury and Farquhar, 1997]

[6] [Yang et al., 2009]

[7] [Earl and Tollenaar, 1997]

[8] [Campbell and Norman, 1998]

Workflow

A system implemented on Cropbox framework can be run by `simulate()` function supplied with an optional configuration. For instance, the coupled gas-exchange model with Medlyn stomatal conductance submodel (`GasExchangeMedlyn`) was run with a set of default parameters described in Table 3.3 and 3.2 (Figure 3.3). `simulate()` function returns a result of simulation in a tabular data frame which can be further analyzed by various tools including visualization methods provided by the framework. By default, the result contains values of all numerical variables declared in the controller system.

```
c0 = (
    :StomataMedlyn ⇒ (g0 = 0.031, g1 = 1.281),
    :NitrogenDependence ⇒ (s = 4.191, N0 = 0.343),
    .. # default configuration
)
r = simulate(GasExchangeMedlyn; config=c0)
```

Figure 3.3: Script for running a coupled gas-exchange model with Medlyn stomatal conductance submodel. Parameter values as listed in Table 3.2 are included in the baseline configuration `c0` used by `simulate()` function.

After testing models with initial parameters, calibration of four parameters, N_0, s, $g_{0_{\mathrm{MED}}}$ and $g_{1_{\mathrm{MED}}}$, as explained in Section 3.2.2 can be done by `calibrate()` function with a training dataset (Figure 3.4). In this example, we had two `target` variables in the dataset, `Photo` and `gs`, and wanted to compare them with `A_net` (A_n) and `gs` (g_s) estimated by the model. A percentage root mean square error (PRMSE) calculated from the difference between each set of variables was minimized by updating four parameters. The range of each parameter value is specified in `parameters` option.

Plotting model response in multiple ranges of criteria would require aggregation of results from models running multiple times with slightly different configuration. `visualize()` function takes care of a few common plotting scenarios in a simple interface. All figures in this paper were directly generated from the framework. For example, Figure 3.9b was

```
obs_df = .. # data frame contains gas exchange measurements
obs_C = .. # list of configurations for each measurement
c1 = calibrate(GasExchangeMedlyn, obs_df, obs_C;
    index = [:PARi ⇒ :PFD, :CO2S ⇒ :CO2, :RH_S ⇒ :RH, :Tair ⇒ :T_air, :Press ⇒ :P_air, :SPAD],
    target = [:Photo ⇒ :A_net, :gs],
    parameters = (
        :NitrogenDependence ⇒ (s=(0, 10), N0=(0, 1)),
        :StomataMedlyn ⇒ (g0=(0, 1), g1=(0, 10)),
    ),
    metric = :prmse,
    .. # other options
)
```

Figure 3.4: Script for calibrating parameters for the gas-exchange model. `index` option provides a mapping of variable names between a dataset and the model specification. `target` option indicates two variables, A_n and g_s, for which fitting errors are minimized. `parameters` option specifies a range of parameter values to be calibrated. A set of calibrated parameters are stored in a variable named `c1`.

generated by running `GasExchangeMedlyn` model with four levels of `RH` (RH) from 20 % to 80 % and plotting `gs` (g_s) against `Ci` (C_i) in lines (Figure 3.5). Each line of response was composed by changing `CO2` (C_a) in a range from 10 µbar to 1500 µbar at an interval of 10 µbar.

A Jupyter notebook containing source code of the model with calibration datasets and scripts for producing figures presented in this paper is available at `https://github.com/cropbox/plants2020`.

3.2.2 Model Calibration

The most of parameter values came from existing literature (Table 3.2). Some photosynthetic parameters were obtained from Pioneer hybrid 3733 maize (*Zea mays*) grown under Soil–Plant–Atmosphere Research (SPAR) chambers located at Beltsville, MD, USA in 2002 [Kim et al., 2012]. Only four parameters were specifically calibrated for modeling experiments presented in this paper. Two are nitrogen-related parameters: baseline leaf nitrogen content (N_0) and steepness of nitrogen response curve (s). The other two are related to stomatal conductance: lower bound of stomatal conductance (g_0) and sensitivity of stomatal

```
visualize(GasExchangeMedlyn; config=(c0, c1),
    x = :Ci, y = :gs,
    xstep = :Weather => :CO2 => 10:10:1500,
    group = :Weather => :RH => [80, 60, 40, 20],
    xlim = (0, 600), ylim = (0, 1), legendpos = (0.8, 0),
    kind = :line
)
```

Figure 3.5: Script for generating Figure 3.9b. `visualize()` function internally runs `simulate()` and renders a plot using the output. Note that a configuration used here is the baseline `c0` partially overridden by the calibrated `c1`. `x` and `y` options specify variables used for two axes of the plot. `xstep` option provides a range of values to compose a single curve, indicating atmospheric CO_2 concentration (C_a) is ranged from 10 µbar to 1500 µbar. `group` option provides a group of treatments to render multiple curves, indicating four levels of relative humidity (RH) are used. `xlim` option sets the visible range of C_i limited from 0 µbar to 600 µbar and `ylim` option sets the range of g_s from 0 to 1 $\mathrm{mol_{H_2O}\,m^{-2}\,s^{-1}\,bar^{-1}}$. `kind` option for plot type can be either `:line` or `:scatter`.

conductance (g_1). For comparison of overall gas-exchange response between two stomatal conductance models, calibration was separately done for the two models: Ball–Berry (BB) and Medlyn (MED) models.

N_0 and s calibrated for BB and MED were then pooled together to provide average parameter values used by the both models. To make sure a slight divergence in the parameter value did not make an impact on overall model response, we also conducted a sensitivity analysis on N_0 and s for a range of possible values. As g_0 and g_1 should involve inherent differences between two stomatal conductance models, a separate set of parameter values were used accordingly. BB model relied on $g_{0_{\mathrm{BB}}}$ and $g_{1_{\mathrm{BB}}}$. MED model relied on $g_{0_{\mathrm{MED}}}$ and $g_{1_{\mathrm{MED}}}$. The optimization method used for calibration was differential evolution algorithm [Storn and Price, 1997].

The experimental dataset for calibration was collected from a growth chamber experiment conducted with Pioneer hybrid 34N43 maize in 2005 at Beltsville, MD, USA as used in Kim et al. [2006, 2007]. Spot measurements of gas-exchange were recorded with LI-COR

LI-6400XT when plants were at the onset of reproductive stage. Three nitrogen levels at $0\,\mathrm{kg\,ha^{-1}}$, $50\,\mathrm{kg\,ha^{-1}}$ and $200\,\mathrm{kg\,ha^{-1}}$ in total were applied two times. For leaf nitrogen content (N), SPAD measurements were instead collected with Konica Minolta SPAD-502 and converted to N.

Our experimental dataset used in calibration had SPAD measurements as a proxy to leaf nitrogen content. A small number of samples were separately collected from direct measurement of leaf nitrogen content and then used to derive a relationship between SPAD measurement and leaf nitrogen content. A quadratic equation in the form of $N = ax^2 + bx + c$ was fitted for leaf nitrogen content (N) and SPAD measurement (x = SPAD) where $a = 0.0004$, $b = 0.012$, and $c = 0$ with $R^2 = 0.92$ (Figure 3.6).

The fitness of model calibration was evaluated by Willmott's refined index of agreement d_r as defined in Equation 2.12 [Willmott et al., 2012] and Nash–Sutcliffe modeling efficiency coefficient (NSE) as defined in Equation 3.42 [Nash and Sutcliffe, 1970]. y_i is an observed value for the variable of interest under a specific environmental condition ordered by i. $\hat{y}_i$ is an estimation by the model for the same input condition as y_i. $\bar{y}$ is the mean of observed values. Net photosynthetic rate (A_n) and stomatal conductance (g_s) were two variables selected for the evaluation.

$$NSE = 1 - \frac{\sum_i (\hat{y}_i - y_i)^2}{\sum_i (y_i - \bar{y})^2} \tag{3.42}$$

3.2.3 Model Comparison

We compared two variants of the gas-exchange model depending on which submodel was used for calculating stomatal conductance: Ball–Berry (BB) and Medlyn (MED). Net photosynthetic rate (A_n) was calculated over a range of values for specific environmental input variables, atmospheric CO_2 and air temperature (T_a). C_a ranged from $0\,\mu\mathrm{bar}$ to $1500\,\mu\mathrm{bar}$ and T_a ranged from $-10\,^\circ\mathrm{C}$ to $50\,^\circ\mathrm{C}$. Other environmental variables remained constant as default values (Table 3.3). Since stomatal conductance can be more directly related to the

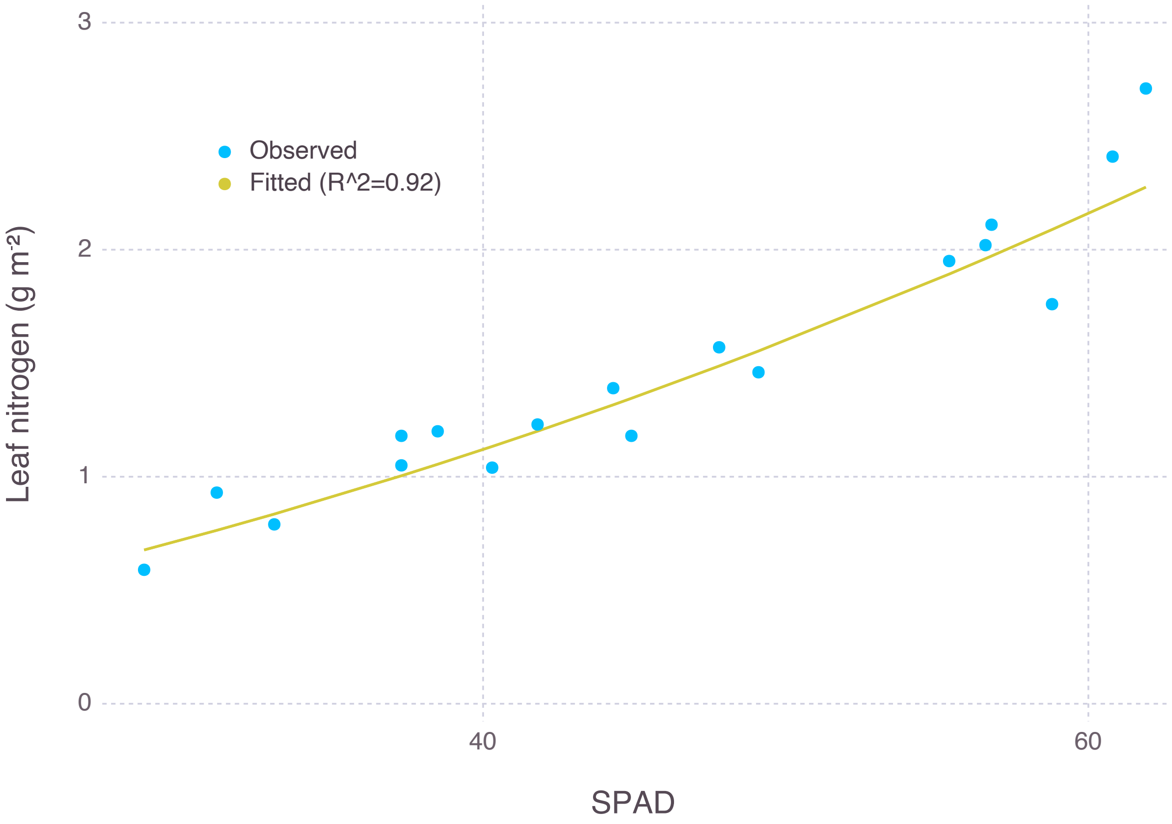

Figure 3.6: Fitting SPAD measurement to leaf nitrogen content (N). N was fitted by a quadratic equation $N = 0.0004x^2 + 0.012x$ for 18 samples of SPAD measurement ($x =$ SPAD) with $R^2 = 0.92$.

relative humidity of surrounding air (RH) than other variables, a response curve of A_n was separately obtained for ten levels of RH from 0 % to 100 %.

3.2.4 Model Response

We simulated nitrogen and water stress factors by adjusting relevant parameter values. For nitrogen stress, leaf nitrogen content (N) was changed from $0\,\mathrm{g\,m^{-2}}$ to $2\,\mathrm{g\,m^{-2}}$ to impose stress when N was lower. For water stress, bulk leaf water potential (Ψ_v) was changed

Table 3.3: Default environmental condition for the coupled gas-exchange model.

Symbol	**Value**	**Units**	**Description**
C_a	400	µbar	Atmospheric CO_2 partial pressure
P_a	99.4	kPa	Atmospheric pressure
T_a	32	°C	Air temperature in Celsius
I	2000	$\mu\text{mol}_{\text{quanta}}\,\text{m}^{-2}\,\text{s}^{-1}$	Incident PAR
u	2	$\text{m}\,\text{s}^{-1}$	Wind speed
RH	66	%	Relative humidity of the air
SPAD	60	-	SPAD value

from 0 MPa down to -3 MPa to impose stress when Ψ_v was lower. The range of values were deliberately chosen by first selecting biophysically feasible extremes, $0\,\text{g}\,\text{m}^{-2}$ for N and 0 MPa for Ψ_v, then selecting a value for the other end where output variable exhibits a clear convergence. When simulating a response for each stress factor, the other stress factor assumed to be not limiting. The response curve of net photosynthetic rate (A_n) was obtained for multiple environmental input variables including relative humidity (RH), atmospheric CO_2 (C_a), air temperature (T_a), and irradiance (I).

In order to observe interaction effects between the two stress factors, contour plot of A_n was obtained by applying the same range of two stress factors simultaneously. For each environmental input variable, four different levels of the value were chosen to show a varying contrast as the input changes. RH changed to 30, 50, 70 and 90 %. C_a changed to 200, 400, 600 and 800 µbar. I changed to 500, 1000, 1500 and $2000\,\mu\text{mol}\,\text{m}^{-2}\,\text{s}^{-1}$.

3.3 Results

3.3.1 Gas-exchange Model Calibration

The performance of calibrated parameters was evaluated by Willmott's refined index of agreement (d_r) and Nash–Sutcliffe model efficiency coefficient (NSE) for the two variants of gas-exchange model (Figure 3.7). d_r of the model with Ball–Berry stomatal conductance submodel (BB) was 0.879 for net photosynthesis rate (A_n) and 0.804 for stomatal conductance (g_s). d_r of the other model with Medlyn submodel (MED) was 0.881 for net photosynthesis rate (A_n) and 0.820 for stomatal conductance (g_s). NSE of the BB model was 0.941 for A_n and 0.798 for g_s. NSE of the MED model was 0.937 for A_n and 0.796 for g_s.

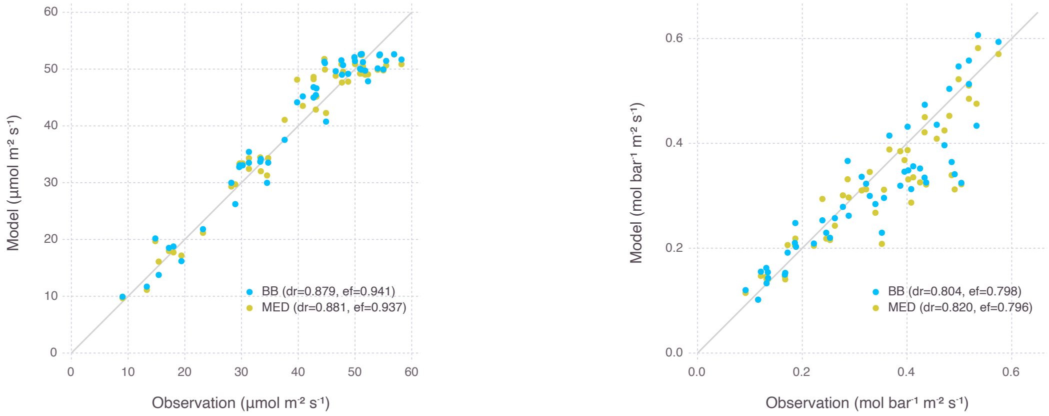

(a) Net photosynthesis rate (A_n)

(b) Stomatal conductance (g_s)

Figure 3.7: Evaluation of the gas-exchange model with two stomatal conductance submodels, Ball–Berry (BB) and Medlyn (MED), after calibrating parameters related to nitrogen (N_0, s) and stomata ($g_{0_{\mathrm{MED}}}$, $g_{1_{\mathrm{MED}}}$). Each dot represents an observed photosynthesis rate (A_n) or stomatal conductance (g_s) under a given experimental condition and a corresponding estimation by the model. A gray solid line shows 1:1 reference for comparison. `dr` indicates Willmott's refined index of agreement (d_r) and `ef` indicates Nash–Sutcliffe modeling efficiency coefficient (NSE).

d_r values were close to 1 meaning our models were calibrated adequately for further analysis carried in the following sections, especially when it was achieved by calibrating only four parameters while most other parameters came from existing models or literature (Table 3.2). The two variants of the gas-exchange model with different selection of the stomatal conductance submodel did not show a clear difference in their performance within the range of input given by our experimental dataset.

Although the difference between two gas-exchange models only came from how stomatal conductance was calculated in submodel, the pooled nature of our calibration process produced a slightly different set of parameters used for the other parts of model, such as nitrogen submodel shared by the two variants. For example, with baseline leaf nitrogen content (N_0) and steepness of nitrogen response curve (s) parameters, BB got 0.371 and 4.470 while MED got 0.315 and 3.912, respectively. To ensure their difference did not hamper comparison between two stomatal conductance models, we did a further sensitivity analysis on the two other parameters and confirmed the difference was negligible in regards with A_n response (Figure 3.8).

The sensitivity of parameters related to nitrogen dependence was obtained by calculating net photosynthesis rate (A_n) with a range of values for the parameter in question while keeping other parameters unchanged (Figure 3.8). For reference, N_0 was 0.371 and 0.315, and s was 4.470 and 3.912, for BB and MED respectively. Baseline leaf nitrogen content (N_0) barely had an impact on A_n with its range from $0.2\,\mathrm{g\,m^{-2}}$ to $0.5\,\mathrm{g\,m^{-2}}$. Sensitivity of nitrogen response curve (s) did not make a large difference either within the range of calibrated parameter values. For example, two sets of N_0 and s mentioned above resulted into less than 1 % difference in A_n at $400\,\mathrm{\mu mol\,m^{-2}\,s^{-1}}$ of ambient CO_2 level. Therefore we assumed the difference between nitrogen parameter values we obtained from calibration for BB and MED were negligible and safe to pool them together for one unified set of parameters. The averaged out values for N_0 and s used in the rest of simulation was 0.343 and 4.191 (Table 3.2).

3.3.2 Stomatal Conductance Model Comparison

g_s predicted by MED was generally higher than g_s from BB (Figure 3.9). g_s from both models were in a similar range when relative humidity (RH) was around 65 % to 90 % while maximum g_s was much higher in MED when RH was saturated. When RH went lower than

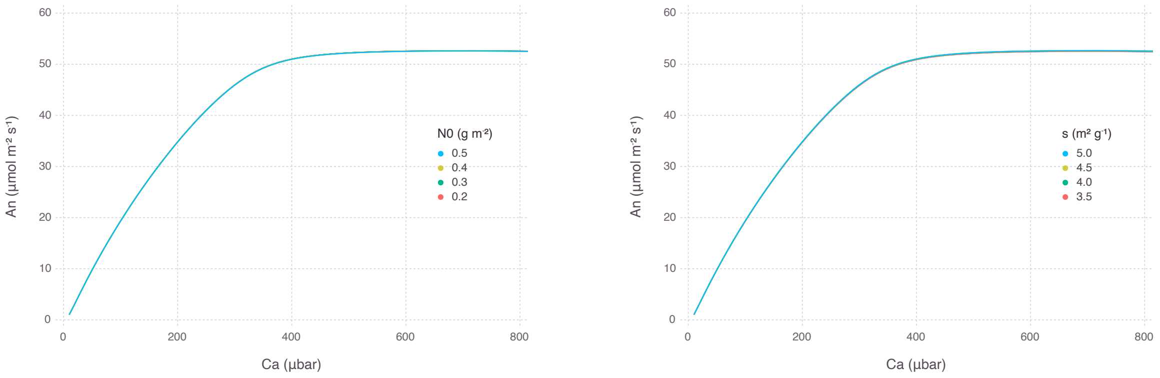

(a) Baseline leaf nitrogen content (N_0)

(b) steepness of nitrogen response curve (s)

Figure 3.8: Sensitivity of parameters related to nitrogen dependence. The coupled gas-exchange model with Medlyn stomatal conductance model was used for testing. Air temperature (T_a) was 32 °C, irradiance (I) was 2000 $\mu\mathrm{mol}_{\mathrm{quanta}}\,\mathrm{m}^{-2}\,\mathrm{s}^{-1}$, and relative humidity (RH) was 66 %.

50 %, gs from BB dropped rapidly and mostly converged to the lower bound ($g_{0_{\mathrm{BB}}}$), almost shutting down transpiration. In MED, decrease of g_s along RH gradient was more gradual and its value usually remained higher than the lower bound ($g_{0_{\mathrm{MED}}}$) to ensure a certain amount of transpiration keeps occurring.

As a result, A_n from the gas-exchange model using BB decreased more rapidly while the counterpart using MED showed a much gentle response as RH went down at the same level of concentration of atmospheric CO_2 (C_a). The rate of decrease in A_n was 75 % with BB and 20 % with MED when RH was dropped from 80 % to 20 %. However, there was little difference in the curvature of A_n response between the two models in terms of intercellular CO_2 concentration (C_i), suggesting the difference was mostly due to a change in supply function of the curve (Figure 3.10).

A similar response can be observed when A_n was plotted against a range of air temperature (T_a) from 0 °C to 50 °C (Figure 3.11). At lower RH, MED was able to maintain g_s to

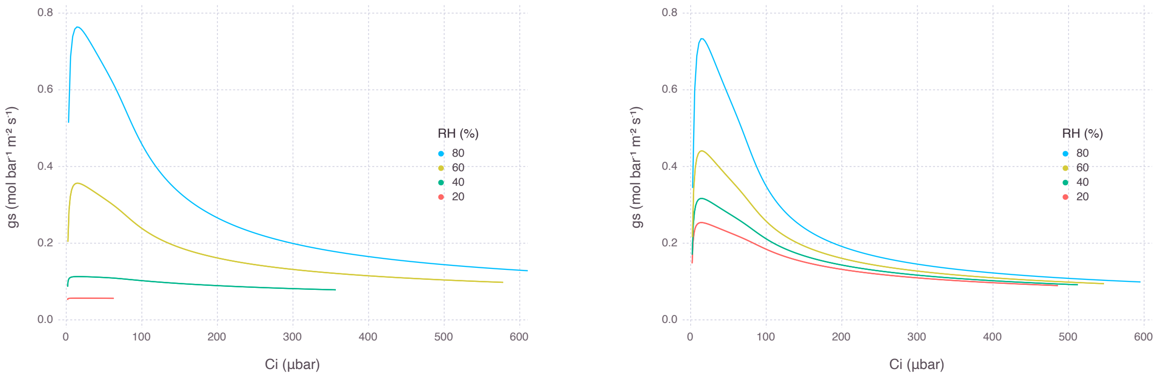

(a) Ball–Berry model (BB)

(b) Medlyn model (MED)

Figure 3.9: Stomatal conductance (g_s) estimated by two stomatal conductance models over a range of atmospheric CO_2 concentration (C_a) from 10 µbar to 1500 µbar at multiple levels of relative humidity (RH). The graph was plotted against resultant intercellular CO_2 concentration (C_i). Air temperature (T_a) was 32 °C and irradiance (I) was 2000 $\mu\text{mol}_{\text{quanta}}\,\text{m}^{-2}\,\text{s}^{-1}$.

a certain level and therefore keep A_n from collapsing. The shifting of optimal temperature towards higher regime with lower RH came from increased cooling effect by higher water loss in drier condition.

In turn, leaf temperature (T_l) which is adjusted by energy balance equation involving latent heat flux mainly driven by leaf transpiration showed a clear difference between the two models. With BB, lower RH had stomata almost closed down and thus not able to cool down leaf temperature with latent cooling. On the contrary, MED implied higher latent cooling under lower RH due to stronger gradient of water vapor pressure formed between air and inside the leaf.

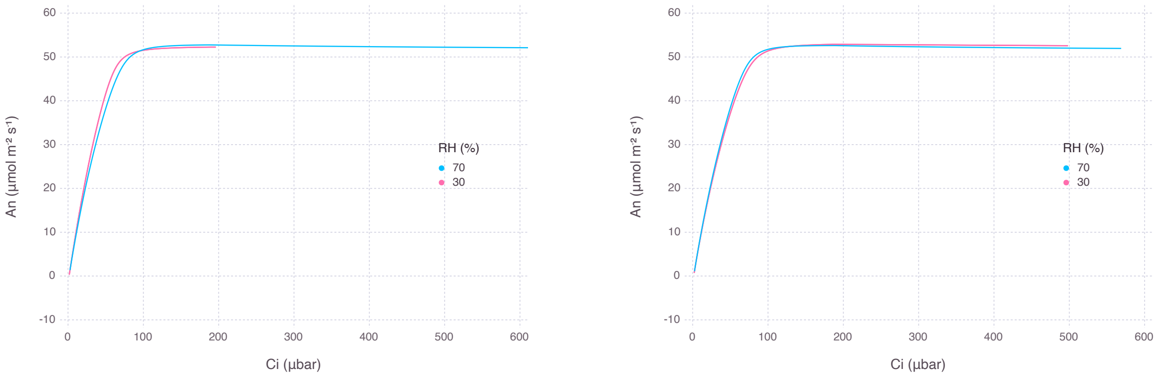

(a) Ball–Berry model (BB)

(b) Medlyn model (MED)

Figure 3.10: Net photosynthesis rate (A_n) estimated by two stomatal conductance models over a range of atmospheric CO$_2$ concentration (C_a) from 10 µbar to 1500 µbar at two levels of relative humidity (RH). The graph was plotted against resultant intercellular CO$_2$ concentration (C_i). Air temperature (T_a) was 32 °C and irradiance (I) was 2000 $\mu\text{mol}_{\text{quanta}}\,\text{m}^{-2}\,\text{s}^{-1}$.

3.3.3 Stress Responses

Leaf Nitrogen Deficiency

A_n generally decreased as leaf nitrogen content (N) reduced and the rate of decrease accelerated when nitrogen was more limited as represented by logarithmic curves. Yet, the strength of response was not constant and varied depending on environmental conditions. A_n was more decreased with lower RH, but the difference diminished when N went below 0.5 $\text{g}\,\text{m}^{-2}$ or relative leaf nitrogen content (N_p) was less than 1 % assuming specific leaf area (SLA) was 200 $\text{cm}^2\,\text{g}^{-1}$. The rate of A_n decrease did not change much with high atmospheric CO$_2$ (C_a) and only had more negative effect when C_a was below 400 $\mu\text{mol}\,\text{mol}^{-1}$. Response to T_a under nitrogen stress was nonlinear that the decrease was more significant when T_a was moving away from optimal temperature. The optimal temperature, where a peak A_n could be achieved, slightly increased with more N available and thus the maximum A_n itself

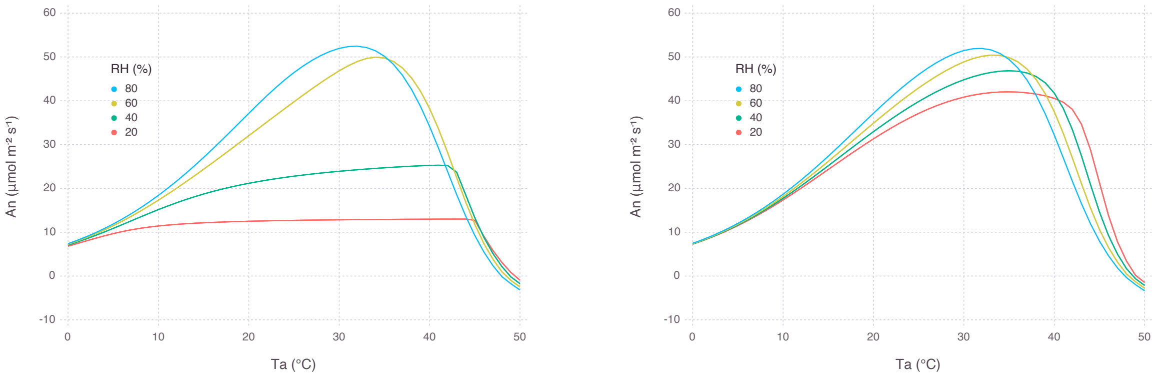

(a) Ball–Berry model (BB)

(b) Medlyn model (MED)

Figure 3.11: Net photosynthesis rate (A_n) estimated by two stomatal conductance models over a range of air temperature (T_a) from 0 °C to 50 °C at multiple levels of relative humidity (RH). Atmospheric CO_2 concentration (C_a) was 400 µbar and irradiance (I) was $2000\,\mu\text{mol}_{\text{quanta}}\,\text{m}^{-2}\,\text{s}^{-1}$.

also increased due to more favorable biochemical reactions with higher temperature and N (Figure 3.12c, 3.12g). The slope of A_n decrease by N stress was steeper under higher irradiance (I) and the difference between the levels of I gradually diminished as N approaching a minimum (Figure 3.12a, 3.12e). Overall, there was no clear difference in terms of nitrogen response between BB and MED models.

Leaf Water Status

A_n decreased as bulk leaf water potential (Ψ_v) reduced, but the rate of decrease did not monotonically change as in the case of nitrogen stress. Generally under a greater water stress with lower water potential, stress response represented by A_n reduction tapered off and formed a logistic response curve. A_n was more decreased with lower RH, but the difference diminished when Ψ_v kept decreasing . Also note that with higher RH, leaf was able to sustain maximum A_n even under mild water deficit which would have led to a noticeable reduction in A_n under lower RH. For example, at $-0.4\,\mathrm{MPa}$, A_n under 80 % of RH did not decrease much whereas A_n under 40 % of RH saw almost 60 % reduction with BB (Figure 3.12b) and 20 % reduction with MED (Figure 3.12f). The decrease of A_n was more consistent with all range of C_a compared to nitrogen stress response. For $-1.5\,\mathrm{MPa}$ and below, the rate of A_n decrease became almost identical regardless of C_a. With higher C_a, maximum A_n was sustained for larger range of Ψ_v similar to the RH response. Water response to T_a was also nonlinear, but the difference wore off with lower Ψ_v and no single optimal temperature was clear to be found (Figure 3.12d, 3.12h). Overall response to T_a under water stress was similar between BB and MED except BB exhibited much higher optimal temperature than MED in a mild-to-severe stress level indicated by $-1.0\,\mathrm{MPa}$. Overall, BB was more sensitive to RH changes under water stressed conditions than MED (Figure 3.12b, 3.12f).

3.3.4 Interactions between Leaf Nitrogen and Water Potential

Response to Relative Humidity

At high RH, A_n remained relatively stable within its optimal range when both N and Ψ_v kept high for less stress (Figure 3.13a, 3.13g). An area of this region located in the upper right side of contour plot shrunk and so did the range of non-limiting N and Ψ_v as RH went down. In other words, with lower RH, A_n became more sensitive to both nitrogen and water stress factors. The reduction of A_n for lower RH was extremely strong with BB (Figure 3.13d) compared to MED (Figure 3.13j). No other variables showed such drastic difference between BB and MED in the comparison.

Note that with low N and high Ψ_v, the sensitivity of A_n was mostly governed by the change of N, thus limited by nitrogen. On the other hand, with high N and low Ψ_v, the most of sensitivity came from the change of Ψ_v, thus limited by water. Then with both low N and Ψ_v, A_n was also largely driven by Ψ_v unless N dropped down to a very low range.

Ball–Berry (BB)

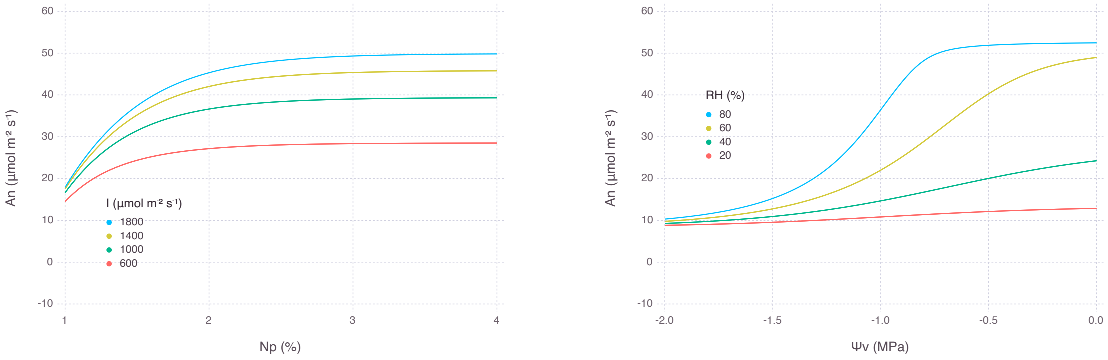

(a) Irradiance (I)

(b) Relative humidity (RH)

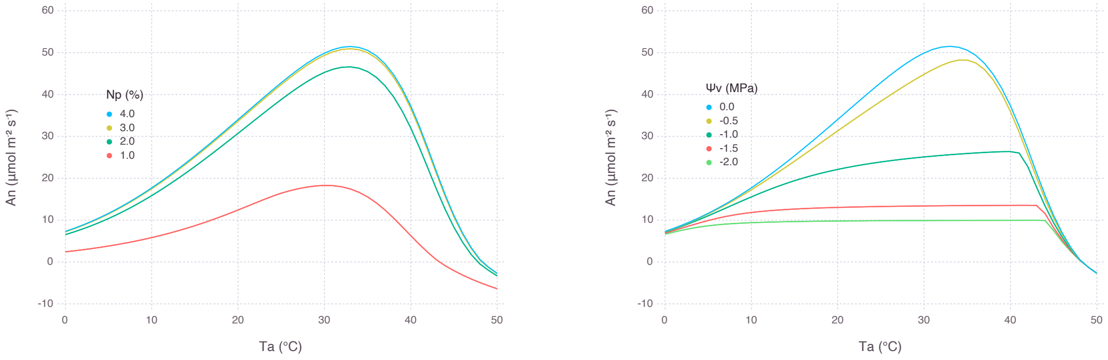

(c) Air temperature (T_a)

(d) Air temperature (T_a)

Figure 3.12: Net photosynthesis rate (A_n) over a range of environmental input variables at multiple levels of nitrogen or water stress for the two variants of coupled gas-exchange model using Ball–Berry (BB) and Medlyn (MED) stomatal conductance submodels. (a), (c), (e) and (g) show responses to a varying degree of relative leaf nitrogen content (N_p) assuming specific leaf area (SLA) was $200\,\mathrm{cm}^2\,\mathrm{g}^{-1}$. (b), (d), (f) and (h) show responses to bulk leaf water potential (Ψ_v). *Continued*

Response to Atmospheric CO_2

The upper-right region of non-limiting A_n existed with a range of C_a above 400 µbar. This region vertically expands further down to cover lower Ψ_v under higher C_a as shown by

Medlyn (MED)

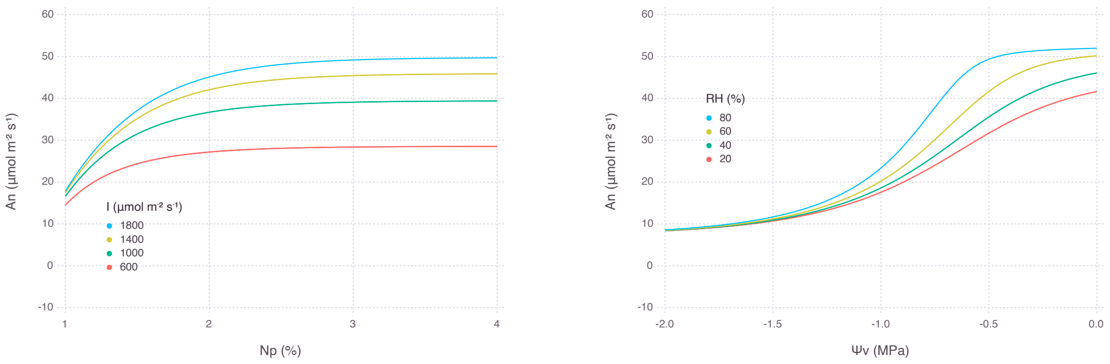

(e) Irradiance (I)　(f) Relative humidity (RH)

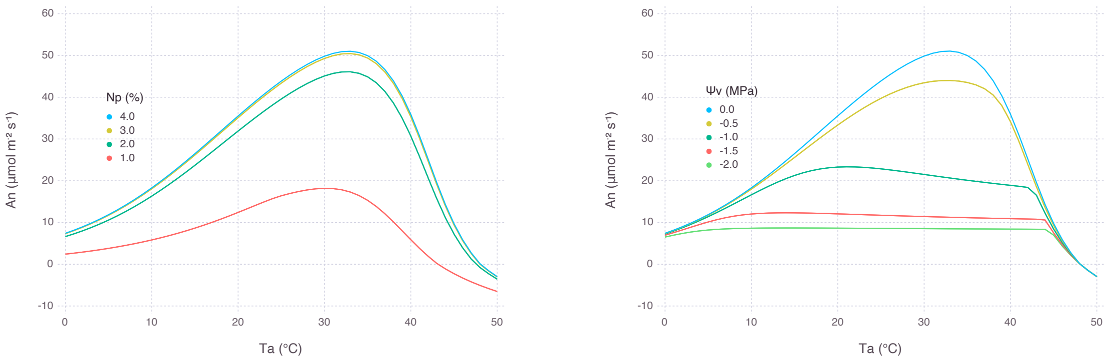

(g) Air temperature (T_a)　(h) Air temperature (T_a)

Figure 3.12: Net photosynthesis rate (A_n) over a range of environmental input variables at multiple levels of nitrogen or water stress for the two variants of coupled gas-exchange model using Ball–Berry (BB) and Medlyn (MED) stomatal conductance submodels. (a), (c), (e) and (g) show responses to a varying degree of relative leaf nitrogen content (N_p) assuming specific leaf area (SLA) was $200\,\mathrm{cm}^2\,\mathrm{g}^{-1}$. (b), (d), (f) and (h) show responses to bulk leaf water potential (Ψ_v).

comparing ambient CO_2 (Figure 3.13e, 3.13k) with elevated CO_2 (Figure 3.13b, 3.13h), indicating possible alleviation of water stress by elevated CO_2 concentration. A_n remained relatively stable until Ψ_v reached down $-1.0\,\mathrm{MPa}$ under $800\,\mu\mathrm{bar}$ of C_a whereas A_n started decreasing faster only after $-0.5\,\mathrm{MPa}$ under $400\,\mu\mathrm{bar}$ of C_a. Below these boundaries, A_n was mostly limited by water only.

Response to Irradiance

The region of non-limiting A_n remained relatively stable with a range of I (Figure 3.13c, 3.13i) and even expanded further down when I was lower, although the magnitude of A_n was much smaller (Figure 3.13f, 3.13l). In other words, under shaded condition with less light, nitrogen and water became less relevant because A_n had to be much smaller. Below this region, A_n was again mostly limited by water only unless N deficiency was extremely strong.

3.4 Discussion

3.4.1 Performance of Stomatal Conductance Models

We did not find much difference in performance between two stomatal conductance submodels BB and MED when used for fitting calibration dataset (Figure 3.7). It is known that two models have equal predictive strength for non-extreme environmental conditions where the data are usually collected for calibration and validation [Franks et al., 2018]. Results started deviating from each other under more extreme conditions such as low C_a and low RH which are also close to the range where gas-exchange instruments often find difficulties in accurate measurements (Figure 3.9, 3.10, 3.11, 3.12b, 3.12f). Under low RH, especially below 50 %, $g_{s_{\mathrm{BB}}}$ had much higher rate of decrease and almost converged to $g_{0_{\mathrm{BB}}}$ in the end whereas $g_{s_{\mathrm{MED}}}$ maintained higher than $g_{0_{\mathrm{MED}}}$ with smooth and gentle transitions most of the time (Figure 3.9). Seemingly degenerate behavior of $g_{s_{\mathrm{BB}}}$ might be an overlooked effect of $g_{0_{\mathrm{BB}}}$ as a parameter estimated from regression rather than a directly measured value [Duursma et al., 2019]. A clearly different response from each model warrants caution especially when applying models to extreme conditions, such as concurrent exposure to high temperature and high vapor pressure deficit (VPD), likely encountered in future climate projections [Hsiao

Ball–Berry (BB)

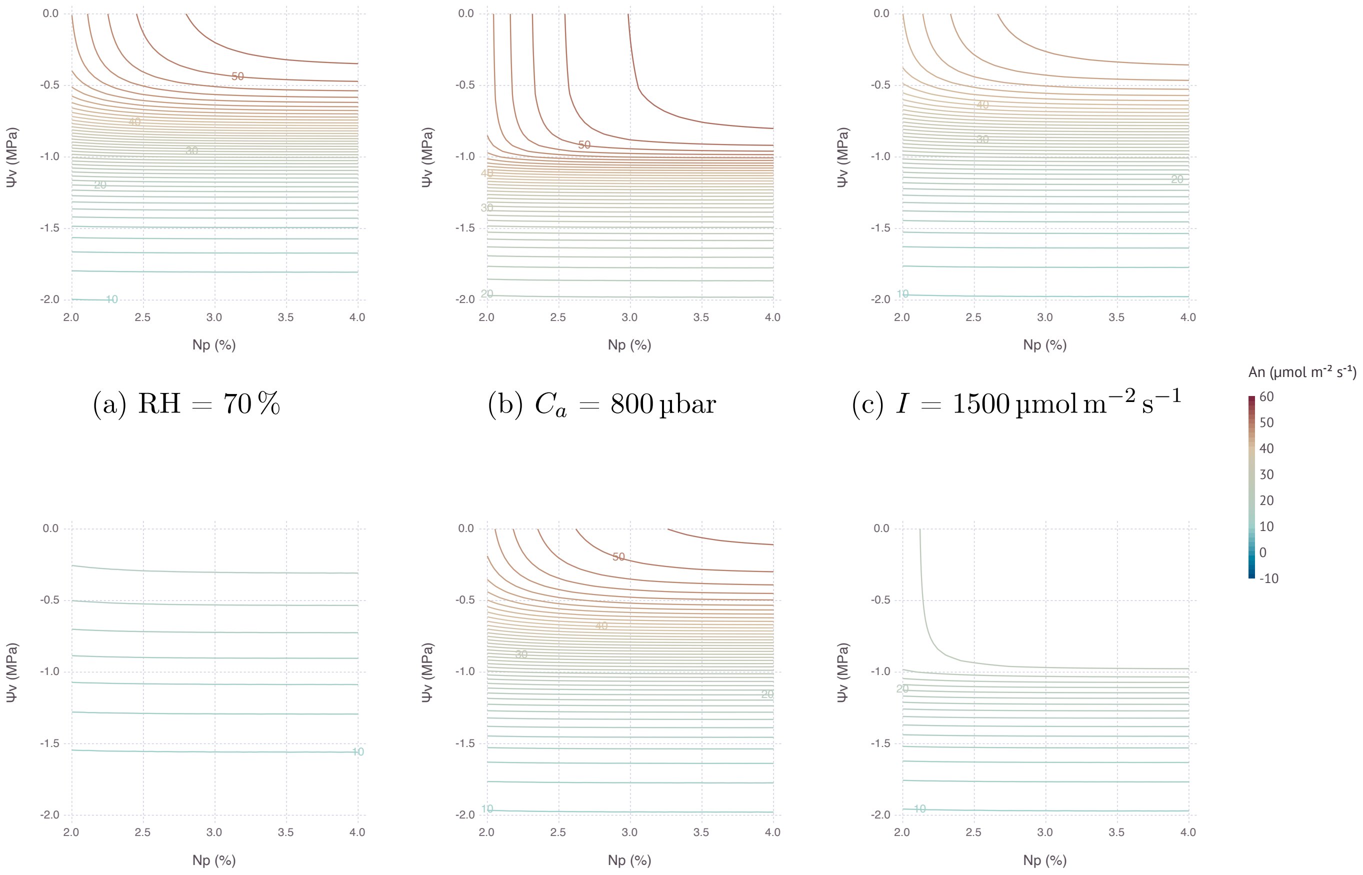

(a) RH = 70 %

(b) C_a = 800 μbar

(c) I = 1500 μmol m^{-2} s^{-1}

(d) RH = 30 %

(e) C_a = 400 μbar

(f) I = 500 μmol m^{-2} s^{-1}

Figure 3.13: Responses of net photosynthesis rate (A_n) under nitrogen and water stress implied by relative leaf nitrogen content (N_p) and bulk leaf water potential (Ψ_v) for the two variants of coupled gas-exchange model using Ball–Berry (BB) and Medlyn (MED). (a)/(d) and (g)/(j) show contrasting effects of high and low relative humidity (RH). (b)/(e) and (h)/(k) compare elevated and current concentrations of atmospheric CO$_2$ (C_a). (c)/(f) and (i)/(l) compare high and low levels of irradiance (I). Contour lines are spaced at an interval of 1 μmol m^{-2} s^{-1} of the simulated A_n values. *Continued*

Medlyn (MED)

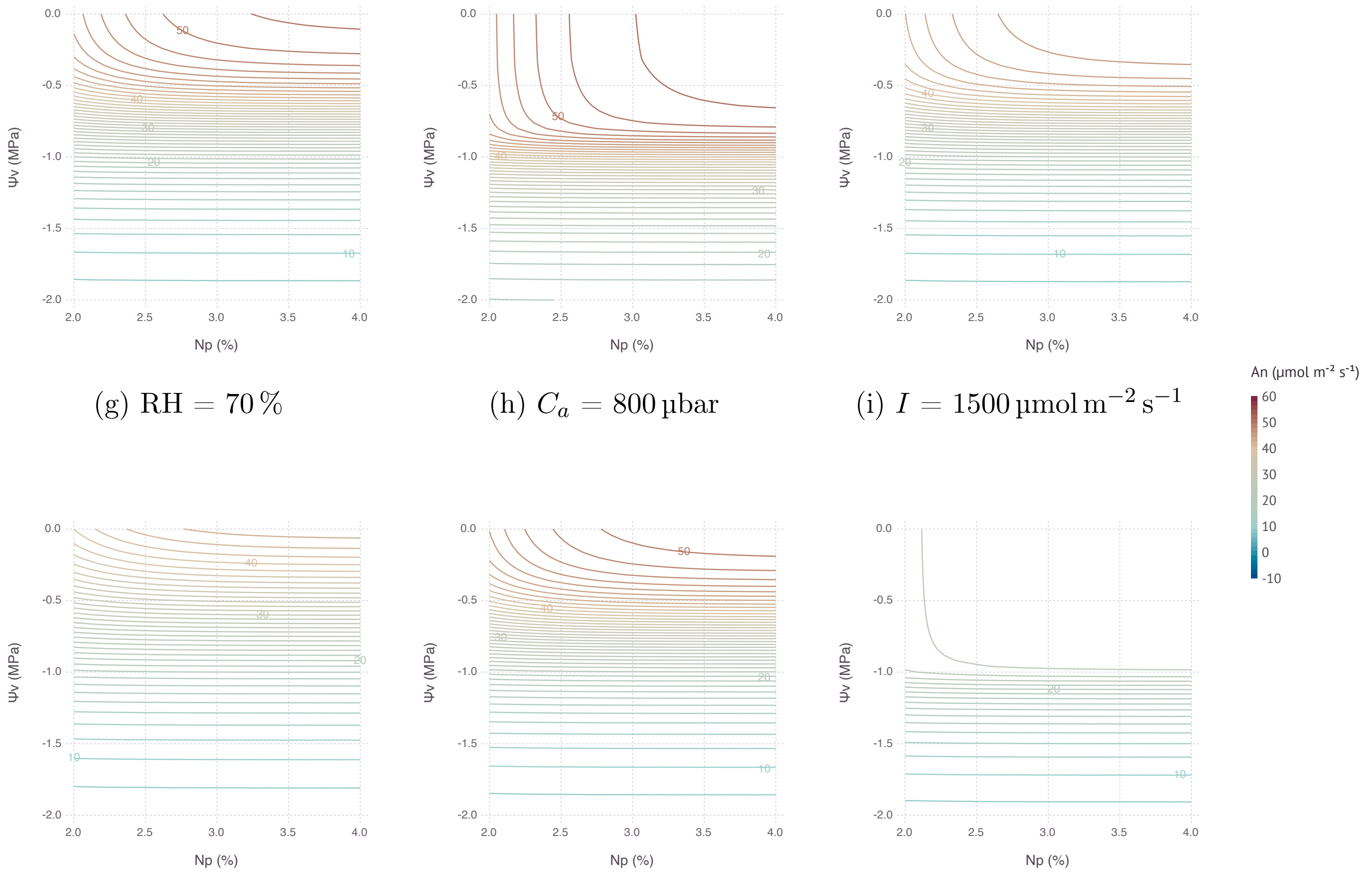

(g) RH = 70 %

(h) C_a = 800 µbar

(i) I = 1500 µmol m^{-2} s^{-1}

(j) RH = 30 %

(k) C_a = 400 µbar

(l) I = 500 µmol m^{-2} s^{-1}

Figure 3.13: Responses of net photosynthesis rate (A_n) under nitrogen and water stress implied by relative leaf nitrogen content (N_p) and bulk leaf water potential (Ψ_v) for the two variants of coupled gas-exchange model using Ball–Berry (BB) and Medlyn (MED). (a)/(d) and (g)/(j) show contrasting effects of high and low relative humidity (RH). (b)/(e) and (h)/(k) compare elevated and current concentrations of atmospheric CO$_2$ (C_a). (c)/(f) and (i)/(l) compare high and low levels of irradiance (I). Contour lines are spaced at an interval of 1 µmol m^{-2} s^{-1} of the simulated A_n values.

et al., 2019].

3.4.2 Stress Response to Elevated CO_2

Nitrogen stress consistently posed a negative impact on A_n although the degree of reduction may vary depending on the severity of stress and corresponding environmental conditions (Figure 3.12a, 3.12c, 3.12e, 3.12g). While water stress also reduced A_n most of the time (Figure 3.12b, 3.12d, 3.12f, 3.12h), we observed in some conditions that the impact of water stress greatly diminished, for instance, when RH was higher than 60 % (Figure 3.13a, 3.13g) or C_a was higher than $400\,\mu\mathrm{mol\,mol^{-1}}$ (Figure 3.13b, 3.13h). There is increasing evidence that elevated CO_2 concentration alleviates water stress [Hsiao and Jackson, 1999, Ghannoum, 2008, Markelz et al., 2011, Xu et al., 2013, Manderscheid et al., 2014, Zong and Shangguan, 2014, van der Kooi et al., 2016]. Our simulation result confirms this positive effect of elevated CO_2 by showing high A_n sustained in a wider range of Ψ_v under high C_a due to reduced g_s preserving water loss via transpiration. The effect was mostly pronounced under a mild water stressed condition since maximum A_n did not change much in the absence of water stress [Leakey et al., 2006]. Alleviation strength was dependent on leaf nitrogen supply such that even very mild water stress could not be overcome by high C_a under low N [Zong and Shangguan, 2014].

3.4.3 Interactions between Nitrogen Deficiency and Water Stress

When both nitrogen and water stress were imposed simultaneously, the net effect of stress may vary depending on the relative degree of each stress factor and environmental variables. In the contour plots of interactive stress effects, we can identity three types of contours (Figure 3.13). Mostly vertical lines with very steep slopes indicate A_n could be only improved by moving across a horizontal gradient, conferring a dominant N sensitivity. Likewise, mostly horizontal lines with close to zero slope indicate A_n could be only improved by moving across a vertical gradient, conferring a dominant Ψ_v sensitivity. Other curves from round contour lines indicate A_n are affected by both stress factors. With that in mind, looking back stress interaction result figures gives an insight that a vast area of N and Ψ_v grid are covered by horizontal lines and thus they are mostly under water limiting conditions. Nitrogen limiting conditions are, on the other hand, exhibited within an area where N is low or Ψ_v is high. Such distinctions could be also found in literature that negative impact of nitrogen stress could be inflated by an existence of drought stress [Morgan, 1984, Shangguan et al., 2000, Markelz et al., 2011, Roth et al., 2013].

3.4.4 Response of Transgenic C_4 Leaves to Temperature

As an extended exercise for testing model response against real conditions, we applied our model to simulate a wide range of temperature response of transgenic C_4 plants, *Flaveria bidentis*, with varying amount of Rubisco reported by Kubien et al. [2003].

A few parameters were derived to replicate a wide range of temperature response of transgenic plants with reduced amounts of Rubisco. We mostly used the same values for variables and parameters identified in the paper, except $J_{\max_{25}}$ which was not mentioned but needed adjustments to replicate original curves (Table 3.4). Measured values of A_n, g_s, and C_i under three treatments were digitized from their Figure 1. WT indicates wild type while AR1 and AR2 refers to mutants treated with anti-Rubisco antibody to have Rubisco content reduced to 49 % and 32 %, respectively.

Table 3.4: Variables and parameters for replicating experiment by Kubien et al. [2003].

Symbol	**Value**	**Units**	**Description**
Input variables			
C_a	370	$\mu\mathrm{bar}$	Atmospheric CO_2 partial pressure
D	12	mbar	Vapor pressure deficit of the air (converted to RH)
I	1500	$\mu\mathrm{mol}_{\mathrm{quanta}}\,\mathrm{m}^{-2}\,\mathrm{s}^{-1}$	Incident PAR
Shared parameters			
$g_{0_{\mathrm{BB}}}$	0.138*	$\mathrm{mol}_{\mathrm{H_2O}}\,\mathrm{m}^{-2}\,\mathrm{s}^{-1}\,\mathrm{bar}^{-1}$	Lower bound of $g_{s_{\mathrm{BB}}}$

Continued

Symbol	**Value**	**Units**	**Description**
$g_{0_{\text{MED}}}$	0.138*	$\text{mol}_{\text{H}_2\text{O}}\,\text{m}^{-2}\,\text{s}^{-1}\,\text{bar}^{-1}$	Lower bound of $g_{s_{\text{MED}}}$
Parameters for WT			
E_{ac}	56.1	$\text{kJ}\,\text{mol}^{-1}$	Activation energy for $V_{c\text{max}}$
E_{ap}	71.6	$\text{kJ}\,\text{mol}^{-1}$	Activation energy for $V_{p\text{max}}$
$J_{\text{max}_{25}}$	300†	$\mu\text{mol}_{\text{electrons}}\,\text{m}^{-2}\,\text{s}^{-1}$	Maximum rate of electron transport at 25 °C
$V_{c\text{max}_{25}}$	51.48	$\mu\text{mol}_{\text{CO}_2}\,\text{m}^{-2}\,\text{s}^{-1}$	Maximum rate of Rubisco carboxylation at 25 °C
$V_{p\text{max}_{25}}$	159.9	$\mu\text{mol}_{\text{CO}_2}\,\text{m}^{-2}\,\text{s}^{-1}$	Maximum rate of PEP carboxylation at 25 °C
Parameters for AR1			
E_{ac}	57.0	$\text{kJ}\,\text{mol}^{-1}$	Activation energy for $V_{c\text{max}}$
E_{ap}	69.4	$\text{kJ}\,\text{mol}^{-1}$	Activation energy for $V_{p\text{max}}$
$J_{\text{max}_{25}}$	240†	$\mu\text{mol}_{\text{electrons}}\,\text{m}^{-2}\,\text{s}^{-1}$	Maximum rate of electron transport at 25 °C
$V_{c\text{max}_{25}}$	24.7	$\mu\text{mol}_{\text{CO}_2}\,\text{m}^{-2}\,\text{s}^{-1}$	Maximum rate of Rubisco carboxylation at 25 °C
$V_{p\text{max}_{25}}$	186.3	$\mu\text{mol}_{\text{CO}_2}\,\text{m}^{-2}\,\text{s}^{-1}$	Maximum rate of PEP carboxylation at 25 °C
Parameters for AR2			
E_{ac}	59.3	$\text{kJ}\,\text{mol}^{-1}$	Activation energy for $V_{c\text{max}}$
E_{ap}	74.0	$\text{kJ}\,\text{mol}^{-1}$	Activation energy for $V_{p\text{max}}$
$J_{\text{max}_{25}}$	120†	$\mu\text{mol}_{\text{electrons}}\,\text{m}^{-2}\,\text{s}^{-1}$	Maximum rate of electron transport at 25 °C
$V_{c\text{max}_{25}}$	15.54	$\mu\text{mol}_{\text{CO}_2}\,\text{m}^{-2}\,\text{s}^{-1}$	Maximum rate of Rubisco carboxylation at 25 °C
$V_{p\text{max}_{25}}$	146.9	$\mu\text{mol}_{\text{CO}_2}\,\text{m}^{-2}\,\text{s}^{-1}$	Maximum rate of PEP carboxylation at 25 °C

[*] Minimum g_s observed in the dataset.

[†] Scaled to the ratio of maximum A_n for each treatment to make up missing information.

By using the set of slightly modified parameters, we were able to replicate overall patterns of A_n (Figure 3.14d) and C_i (Figure 3.14f) over a wide range of T_l using MED. BB also performed closely to MED except that C_i under low T_a with more reduced Rubisco (AR2) showed an abrupt change due to g_s went too low reaching the lower bound $g_{0_{\text{BB}}}$ (Figure 3.14a, 3.14c).

Simulated g_s closely followed the actual measurements until around 35 °C where model and observation started showing disagreement (Figure 3.14b, 3.14e). In the experiment, g_s

kept increasing further with higher T_l whereas our model estimated g_s should decrease when A_n was not able to keep up under excessive heat stress. Such decreasing patterns occurred regardless of stomatal conductance submodels. This behavior is indeed contrary to observations where transpiration rate continually increases with higher leaf temperature, implying A_n inhibition is not caused by stomatal closure and thus A_n should decouple from g_s for some species [Crafts-Brandner and Salvucci, 2002, Urban et al., 2017]. However, this mechanism is not easily applicable to many if not all commonly used gas-exchange models relying on empirical relationship between A_n and g_s as explained in Appendix 3.2.1. Alternative stomatal conductance models with mechanistic understandings on stomata responses to humidity and temperature could be useful for simulating field conditions where temperature fluctuates more than humidity [Peak and Mott, 2011, Buckley and Mott, 2013]. In the meantime, more attention should be paid to the current results of gas-exchange models under high temperature which is especially critical when simulating climate change scenarios.

3.5 Conclusions

We compared how two stomatal conductance models, Ball-Berry (BB) and Medlyn (MED), perform when coupled with the C_4 photosynthesis model of von Caemmerer [2000]. Traditionally BB has been widely used in leaf gas-exchange modeling research. More recently proposed MED approach is founded upon BB approach to provide physiological underpinnings of empirical parameters and considered as an alternative to BB. Our results confirmed that the performance of two models were comparable in a wide range of environmental conditions, yet could deviate substantially in low humidity conditions.

We further tested applicability of the model by replicating the behavior of transgenic C_4 leaves under moderate temperatures found in the literature. The coupled model, however, underestimated stomatal conductance in very high temperatures, presumably due to an inherent limitation of the coupling approaches using Ball–Berry type models in which photosynthesis and stomatal conductance are recursively linked as an input of the other.

We were able to reach this findings thanks to a novel modeling framework written in Julia

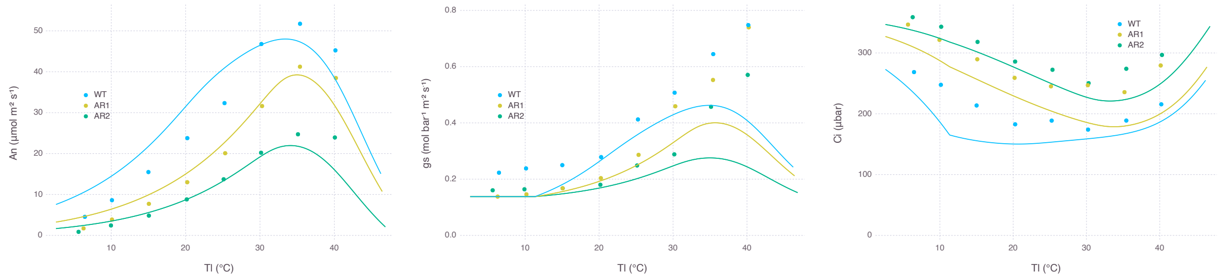
Ball–Berry (BB)

(a) Net photosynthetic rate (A_n) (b) Stomatal conductance (g_s) (c) Intercellular [CO_2] (C_i)

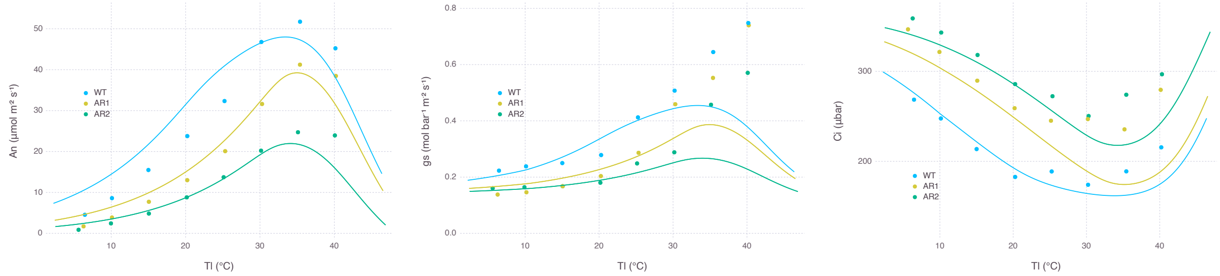
Medlyn (MED)

(d) Net photosynthetic rate (A_n) (e) Stomatal conductance (g_s) (f) Intercellular [CO_2] (C_i)

Figure 3.14: Gas-exchange simulation results over a range of leaf temperature for wild type (WT) and mutants (AR1, AR2) *Flaveria bidentis* leaves with Rubisco content reduced to 49 % and 32 % respectively to replicate Figure 1 of Kubien et al. [2003]. Variables and parameters modified for this simulation are listed in Table 3.4. Other parameters remained the same as listed in Table 3.2. Solid curves represent model estimation for each treatment. Dots indicate data points digitized from the result of original experiment.

programming language used for model development and analysis [Cropbox.jl]. Our modeling approach is extensible and can be a useful means for studying the ecophysiology of C_4 plants including staple and energy crops such as maize, sorghum, and switchgrass.

BIBLIOGRAPHY

J. Timothy Ball, Ian E. Woodrow, and Joseph A. Berry. A model predicting stomatal conductance and its contribution to the control of photosynthesis under different environmental conditions. In J. Biggens, editor, *Progress in Photosynthesis Research*, pages 221–224. Springer, Dordrecht, Netherlands, 1987.

Jeff Bezanson, Alan Edelman, Stefan Karpinski, and Viral B. Shah. Julia: a fresh approach to numerical computing. *SIAM Review*, 59(1):65–98, 2017.

T. N. Buckley, K. A. Mott, and G. D. Farquhar. A hydromechanical and biochemical model of stomatal conductance. *Plant, Cell & Environment*, 26(10):1767–1785, 2003.

Thomas N. Buckley and Keith A. Mott. Modelling stomatal conductance in response to environmental factors. *Plant, Cell & Environment*, 36(9):1691–1699, 2013.

Gaylon S. Campbell and John Norman. *An Introduction to Environmental Biophysics*. Springer-Verlag, New York, NY, USA, 2nd edition, 1998.

G. James Collatz, J. Timothy Ball, Cyril Grivet, and Joseph A Berry. Physiological and environmental regulation of stomatal conductance, photosynthesis and transpiration: a model that includes a laminar boundary layer. *Agricultural and Forest Meteorology*, 54 (2):107–136, 1991.

GJ Collatz, M Ribas-Carbo, and JA Berry. Coupled photosynthesis-stomatal conductance model for leaves of C_4 plants. *Functional Plant Biology*, 19(5):519–538, 1992.

Steven J. Crafts-Brandner and Michael E. Salvucci. Sensitivity of photosynthesis in a C_4 plant, maize, to heat stress. *Plant Physiology*, 129(4):1773–1780, 2002.

Cropbox.jl. `https://github.com/cropbox/Cropbox.jl`.

D. G. G. de Pury and G. D. Farquhar. Simple scaling of photosynthesis from leaves to canopies without the errors of big-leaf models. *Plant, Cell & Environment*, 20(5): 537–557, 1997.

R. C. Dewar. The ball–berry–leuning and tardieu–davies stomatal models: synthesis and extension within a spatially aggregated picture of guard cell function. *Plant, Cell & Environment*, 25(11):1383–1398, 2002.

Remko A. Duursma. Plantecophys — an r package for analysing and modelling leaf gas exchange data. *PLOS ONE*, 10(11):1–13, 2015.

Remko A. Duursma, Christopher J. Blackman, Rosana Lopéz, Nicolas K. Martin-StPaul, Hervé Cochard, and Belinda E. Medlyn. On the minimum leaf conductance: its role in models of plant water use, and ecological and environmental controls. *New Phytologist*, 221(2):693–705, 2019.

H. J. Earl and M. Tollenaar. Maize leaf absorptance of photosynthetically active radiation and its estimation using a chlorophyll meter. *Crop Science*, 37(2):436–440, 1997.

G. D. Farquhar, S. von Caemmerer, and J. A. Berry. A biochemical model of photosynthetic CO_2 assimilation in leaves of C_3 species. *Planta*, 149(1):78–90, 1980.

Peter J. Franks, Joseph A. Berry, Danica L. Lombardozzi, and Gordon B. Bonan. Stomatal function across temporal and spatial scales: Deep-time trends, land–atmosphere coupling and global models. *Plant Physiology*, 174(2):583–602, 2017.

Peter J. Franks, Gordon B. Bonan, Joseph A. Berry, Danica L. Lombardozzi, N. Michele Holbrook, Nicholas Herold, and Keith W. Oleson. Comparing optimal and empirical stomatal conductance models for application in earth system models. *Global Change Biology*, 24(12):5708–5723, 2018.

Oula Ghannoum. C_4 photosynthesis and water stress. *Annals of Botany*, 10(4):635–644, 2008.

Samantha Hartzell, Mark S. Bartlett, and Amilcare Porporato. Unified representation of the C_3, C_4, and cam photosynthetic pathways with the photo3 model. *Ecological Modelling*, 384:173–187, 2018.

Jennifer Hsiao, Abigail L.S. Swann, and Soo-Hyung Kim. Maize yield under a changing climate: The hidden role of vapor pressure deficit. *Agricultural and Forest Meteorology*, 279:107692, 2019.

Theodore C. Hsiao and Robert B. Jackson. Interactive effects of water stress and elevated CO_2 on growth, photosynthesis, and water use efficiency. In Yiqi Luo and Harold A. Mooney, editors, *Carbon Dioxide and Environmental Stress*, pages 3–31. Academic Press, San Diego, CA, USA, 1999.

Hamlyn G. Jones. *Plants and Microclimate: A Quantitative Approach to Environmental Plant Physiology.* Cambridge University Press, Cambridge, UK, 3rd edition, 2013.

Jens Kattge, Wolfgang Knorr, Thomas Raddatz, and Christian Wirth. Quantifying photosynthetic capacity and its relationship to leaf nitrogen content for global-scale terrestrial biosphere models. *Global Change Biology*, 15(4):976–991, 2009.

Soo-Hyung Kim and J. Heinrich Lieth. A coupled model of photosynthesis, stomatal conductance and transpiration for a rose leaf (*Rosa hybrida L.*). *Annals of Botany*, 91 (7):771–781, 2003.

Soo-Hyung Kim, Richard C. Sicher, Hanhong Bae, Dennis C. Gitz, Jeffrey T. Baker, Dennis J. Timlin, and Vangimalla R. Reddy. Canopy photosynthesis, evapotranspiration, leaf nitrogen, and transcription profiles of maize in response to CO_2 enrichment. *Global Change Biology*, 12(3):588–600, 2006.

Soo-Hyung Kim, Dennis C. Gitz, Richard C. Sicher, Jeffrey T. Baker, Dennis J. Timlin, and Vangimalla R. Reddy. Temperature dependence of growth, development, and photosynthesis in maize under elevated CO_2. *Environmental and Experimental Botany*, 61(3):224–236, 2007.

Soo-Hyung Kim, Yang Yang, Dennis J. Timlin, David H. Fleisher, Annette Dathe, Vangimalla R. Reddy, and Kenneth Staver. Modeling temperature responses of leaf growth, development, and biomass in maize with maizsim. *Agronomy Journal*, 104(6): 1523–1537, 2012.

Soo-Hyung Kim, Jennifer Hsiao, and Hannah Kinmonth-Schultz. Advances and improvements in modeling plant processes. In Kenneth Boote, editor, *Advances in Crop Modelling for a Sustainable Agriculture*, pages 3–43. Burleigh Dodds Science Publishing, London, UK, 2019.

M. U. F. Kirschbaum. The sensitivity of C_3 photosynthesis to increasing CO_2 concentration: a theoretical analysis of its dependence on temperature and background CO_2 concentration. *Plant, Cell & Environment*, 17(6):747–754, 1994.

David S. Kubien, Susanne von Caemmerer, Robert T. Furbank, and Rowan F. Sage. C_4 photosynthesis at low temperature. a study using transgenic plants with reduced amounts of rubisco. *Plant Physiology*, 132(3):1577–1585, 2003.

Andrew D.B. Leakey, Martin Uribelarrea, Elizabeth A. Ainsworth, Shawna L. Naidu, Alistair Rogers, Donald R. Ort, and Stephen P. Long. Photosynthesis, productivity, and yield of maize are not affected by open-air elevation of CO_2 concentration in the absence of drought. *Plant Physiology*, 140(2):779–790, 2006.

R. Leuning. A critical appraisal of a combined stomatal-photosynthesis model for C_3 plants. *Plant, Cell & Environment*, 18(4):339–355, 1995.

Remy Manderscheid, Martin Erbs, and Hans-Joachim Weigel. Interactive effects of free-air CO_2 enrichment and drought stress on maize growth. *European Journal of Agronomy*, 52:11–21, 2014.

R. J. Cody Markelz, Reid S. Strellner, and Andrew D. B. Leakey. Impairment of C_4 photosynthesis by drought is exacerbated by limiting nitrogen and ameliorated by elevated [CO_2] in maize. *Journal of Experimental Botany*, 62(9):3235–3246, 2011.

B. E. Medlyn, F. W. Badeck, D. G. G. de Pury, C. V. M. Barton, M. Broadmeadow, R. Ceulemans, P. de Angelis, M. Forstreuter, M. E. Jach, S. Kellomäki, E. Laitat, M. Marek, S. Philippot, A. Rey, J. Strassemeyer, K. Laitinen, R. Liozon, B. Portier, P. Roberntz, K. Wang, and P. G. Jstbid. Effects of elevated [CO_2] on photosynthesis in european forest species: a meta-analysis of model parameters. *Plant, Cell & Environment*, 22(12):1475–1495, 1999.

Belinda E. Medlyn, D. Loustau, and S. Delzon. Temperature response of parameters of a biochemically based model of photosynthesis. i. seasonal changes in mature maritime pine (*Pinus pinaster* ait.). *Plant, Cell & Environment*, 25(9):1155–1165, 2002.

Belinda E. Medlyn, Remko A. Duursma, Derek Eamus, David S. Ellsworth, I. Colin Prentice, Craig V. M. Barton, Kristine Y. Crous, Paolo de Angelis, Michael Freeman, and Lisa Wingate. Reconciling the optimal and empirical approaches to modelling stomatal conductance. *Global Change Biology*, 17(6):2134–2144, 2011.

John L. Monteith and Mike H. Unsworth. *Principles of Environmental Physics: Plants, Animals, and the Atmosphere.* Academic Press, Cambridge, MA, USA, 4th edition, 2014.

Jack A. Morgan. Interaction of water supply and n in wheat. *Plant Physiology*, 76(1): 112–117, 1984.

J.E. Nash and J.V. Sutcliffe. River flow forecasting through conceptual models part i – a discussion of principles. *Journal of Hydrology*, 10(3):282–290, 1970.

Nedialko T. Nikolov, William J. Massman, and Anna W. Schoettle. Coupling biochemical and biophysical processes at the leaf level: an equilibrium photosynthesis model for leaves of C_3 plants. *Ecological Modelling*, 80(2):205–235, 1995.

David Peak and Keith A. Mott. A new, vapour-phase mechanism for stomatal responses to humidity and temperature. *Plant, Cell & Environment*, 34(1):162–178, 2011.

Jason A. Roth, Ignacio A. Ciampitti, and Tony J. Vyn. Physiological evaluations of recent drought-tolerant maize hybrids at varying stress levels. *Agronomy Journal*, 105 (4):1129–1141, 2013.

Rowan F. Sage. Variation in the kcat of rubisco in C_3 and C_4 plants and some implications for photosynthetic performance at high and low temperature. *Journal of Experimental Botany*, 53(369):609–620, 2002.

P.J. Sellers, D.A. Randall, G.J. Collatz, J.A. Berry, C.B. Field, D.A. Dazlich, C. Zhang, G.D. Collelo, and L. Bounoua. A revised land surface parameterization (sib2) for atmospheric gcms. part i: Model formulation. *Journal of Climate*, 9(4):676–705, 1996.

Zhouping Shangguan, Mingan Shao, and Jens Dyckmans. Effects of nitrogen nutrition and water deficit on net photosynthetic rate and chlorophyll fluorescence in winter wheat. *Journal of Plant Physiology*, 156(1):46–51, 2000.

Thomas R. Sinclair and Thomas W. Rufty. Nitrogen and water resources commonly limit crop yield increases, not necessarily plant genetics. *Global Food Security*, 1(2): 94–98, 2012.

Rainer Storn and Kenneth Price. Differential evolution – a simple and efficient heuristic for global optimization over continuous spaces. *Journal of Global Optimization*, 11(4): 341–359, 1997.

Dennis Timlin, Olaf David, Timothy R. Green, David H. Fleisher, Soo-Hyung Kim, and Laj R. Ahuja. Proposed standards for peer-reviewed publication of computer code. *Agronomy Journal*, 108(5):1782–1786, 2016.

A. Tuzet, A. Perrier, and R. Leuning. A coupled model of stomatal conductance, photosynthesis and transpiration. *Plant, Cell & Environment*, 26(7):1097–1116, 2003.

Josef Urban, Miles W. Ingwers, Mary Anne McGuire, and Robert O. Teskey. Increase in leaf temperature opens stomata and decouples net photosynthesis from stomatal conductance in *Pinus taeda* and *Populus deltoides x nigra*. *Journal of Experimental Botany*, 68(7):1757–1767, 2017.

Casper J. van der Kooi, Martin Reich, Markus Löw, Luit J. De Kok, and Michael Tausz. Growth and yield stimulation under elevated CO_2 and drought: A meta-analysis on crops. *Environmental and Experimental Botany*, 122:150–157, 2016.

Susanna von Caemmerer. *Biochemical Models of Leaf Photosynthesis.* CSIRO Publishing, Clayton, Australia, 2000.

Jan Vos, P. E. L. van der Putten, and C. J. Birch. Effect of nitrogen supply on leaf appearance, leaf growth, leaf nitrogen economy and photosynthetic capacity in maize (*Zea mays* l.). *Field Crops Research*, 93(1):64–73, 2005.

Cort J. Willmott, Scott M. Robeson, and Kenji Matsuura. A refined index of model performance. *International Journal of Climatology*, 32(13):2088–2094, 2012.

Alex Wu, Youhong Song, Erik J. van Oosterom, and Graeme L. Hammer. Connecting biochemical photosynthesis models with crop models to support crop improvement. *Frontiers in Plant Science*, 7:1518, 2016.

Zhenzhu Xu, Hideyuki Shimizu, Yasumi Yagasaki, Shoko Ito, Yuanrun Zheng, and Guangsheng Zhou. Interactive effects of elevated CO_2, drought, and warming on plants. *Journal of Plant Growth Regulation*, 32(4):692–707, 2013.

Yang Yang, Soo-Hyung Kim, Dennis J. Timlin, David H. Fleisher, B. Quebedeaux, and V. R. Reddy. Simulating canopy transpiration and photosynthesis of corn plants under contrasting water regimes using a coupled model. *Transactions of the ASABE*, 52(3): 1011–1024, 2009.

X. Yin and P.C. Struik. C_3 and C_4 photosynthesis models: An overview from the perspective of crop modelling. *NJAS – Wageningen Journal of Life Sciences*, 57(1): 27–38, 2009.

Yuzheng Zong and Zhouping Shangguan. Nitrogen deficiency limited the improvement of photosynthesis in maize by elevated CO_2 under drought. *Journal of Integrative Agriculture*, 13(1):73–81, 2014.

Chapter 4

APPLICATION III: GARLIC MODEL

Abstract

A new crop model for garlic (*Allium sativum*) was built for yield estimation under diverse environmental conditions. An existing process-based model was capable of simulating leaf growth and development, but not validated for biomass allocation which is a critical component for yield estimation. We used Cropbox framework to implement the new model for taking advantage of declarative modeling language and unified interface for simulation. The model was validated against three datasets with an emphasis on biomass measurements. For model application, optimal planting date was assessed under future climate conditions to review climate adaptation between two contrasting locations in South Korea, where one is the current growing region (Gosan) and the other is an unfavorable region (Chuncheon) due to cold winter. The model was able to simulate growth and development of a southern-type cultivar (Namdo) with minimum adjustment in the parameters from previous model. Under RCP (Representative Concentration Pathway) scenarios, an overall delay in optimal planting date from a week to a month was expected in Gosan with a slight increase in potential yield although yield difference between planting dates was smaller. Expansion of growing region to northern area including Chuncheon was expected due to mild winter temperature in the future which would allow growing Namdo cultivar in more regions. Optimal planting date in the new region was predicted similar to the current growing region that favors early planting in fall. Our process-based garlic model provides more mechanistic responses to environmental cues and thus allows simulation under unobserved climate conditions useful for climate adaptation assessment.

4.1 Introduction

Garlic (*Allium sativum*) is a historically important horticultural crop in many countries with global production reaching 30.7 million tons in 2019 after 40 % increase of production in the last decade [FAO, 2020]. Physiology of garlic has been extensively studied with an emphasis on characteristics as a bulbous crop where a clove of bulb is planted for growth and a newly grown bulb is harvested for storage and the next round of planting [Takagi, 1989, Kamenetsky, 2007]. Some knowledge has been transferred to building crop models specifically targeted for simulating garlic growth and estimating yield at harvest. An early attempt for building a whole-plant garlic model was based on radiation-use efficiency (RUE) to obtain the total amount of carbon assimilates [Rizzalli et al., 2002]. Similarly, an RUE-based general crop model CropSyst was parameterized for garlic and used for simulating crop rotation between garlic and wheat [Giménez et al., 2016]. Other studies focused on a certain aspect of garlic growth and development. The crop coefficient (K_c) needed for calculating evapotranspiration with Penman-Monteith equation was specifically determined for garlic [Villalobos et al., 2004]. Photosynthesis and transpiration responses to various environmental conditions were obtained for building a leaf-level gas-exchange model for garlic [Kim et al., 2013]. Photosynthetic responses under elevated CO_2 and nitrogen fertilization were further investigated for building a robust model for future climate conditions [Nackley et al., 2016]. With a coupled gas-exchange model parameterized for garlic, a process-based model for simulating leaf development and growth of hardneck garlic was developed [Hsiao et al., 2019]. Phenology of leaf initiation and appearance was individually tracked by taking account of multiple cues including thermal time accumulation, bulb storage effect, and photoperiod. Individual leaf elongation was translated and aggregated into leaf area expansion at canopy level which was then divided into two layers of sunlit and shaded leaves for accounting assimilated carbon based on the coupled gas-exchange model. However, carbon partitioning into plant organs such as bulb was not validated and thus not used for yield estimation. Carbon partitioning is a crucial step in yield estimation modeling for horticultural crops in a sense that the final yield is a result of biomass partitioned into a certain organ, such as bulb, to be harvested [Marcelis et al., 1998]. The early garlic model used a set of multiple partitioning coefficients dynamically varying with development stages of the plant [Rizzalli et al., 2002].

Yield estimation for garlic cultivars grown in each region has been crucial to manage growing practices and maintain a stable supply in the market [Põldma et al., 2005, Lee et al., 2011, Abdalla et al., 2011, Portela et al., 2012]. Regression models based on weather data or satellite images were often used for yield estimation at a large scale with a minimum set of historical input data [Choi and Baek, 2016, Gómez et al., 2021]. Although worldwide garlic production has been steadily increased in the recent years, it is unclear if yield will be stable in the current growing regions under future climate conditions. For estimating yield under previously unobserved conditions, it is critical to develop a physiological understanding of how garlic would respond to these environmental cues [Nackley et al., 2016]. Regional climate changes may lead to changes in current farming practices and shifts in growing regions to maintain or maximize the yield. Crop model is an important tool for supporting such decisions by enabling simulations of plant growth under diverse climate adaptation strategies [Rosenzweig et al., 2014, Holzkämper et al., 2015, Corbeels et al., 2018].

In this study, our primary objective was to build a garlic model suitable for yield estimation under diverse environments including future climate conditions. A new model was developed based on an existing process-based garlic model with an original emphasis on phenology and extended with a focus on biomass accumulation and partitioning [Hsiao et al., 2019]. The model was also improved to better reflect physiological responses to temperature by taking account storage conditions of seed garlic bulbs and cold stress response in terms of leaf-level growth and canopy-level mortality. We used Cropbox modeling framework for reimplementation to take advantage of its declarative modeling language and unified interface for coordinating a large batch of simulations with minimum configurations [Yun et al., 2020]. For model testing, a new parameter set was specifically calibrated for Namdo cultivar (*Allium sativum* 'Namdo') and validated with multiple datasets with biomass measurements. For demonstrating yield estimation capability of the model, a climate adaptation strategy was assessed by model simulations for the same cultivar grown in two locations of South Korea. Namdo is a cultivar originally adapted to warm climate in southern region of Korea [Kim et al., 2009]. However, the boundary of growth region between northern and southern types of garlic has moved northward in the past decades due to warming climate [Heo et al., 2006]. Optimal planting dates for achieving maximum yield were discovered through model simulation under current and future climate conditions in the two locations where one is an already established region for growing southern-type garlic and the other has a potential to become a new establishment in the future.

4.2 Materials and Methods

4.2.1 Garlic Model

The garlic growth model was extended from a process-based model for leaf development and growth in hardneck garlic [Hsiao et al., 2019]. The original model was capable of simulating leaf area expansion at an individual leaf level and estimating carbon assimilated in a canopy calculated by coupled gas-exchange, but assessing biomass allocated into a particular organ, i.e. bulb, was not a primary subject of the model at the time. For realistic yield prediction under future scenarios, the model should be able to be reliable under diverse environmental conditions [IPCC, 2014]. Model changes made for the experiments reported in this paper include improved biomass allocation, a dynamically adjusted phyllochron, and cold stress response. For the sake of technical convenience, model code originally written in C++ was reimplemented with Cropbox modeling framework using Julia programming language [Cropbox.jl]. The Cropbox framework allowed a streamlined model development from model description in a concise declarative form, iterative parameter adjustments within a notebook environment, and batch simulation of large sets of parameters and production of figures included in this paper.

Biomass Allocation

The total amount of carbon assimilation was calculated by a C_3 photosynthesis model coupled with a stomatal conductance model and energy balance model as described in the previous paper [Hsiao et al., 2019]. Note that overall model structure including the gas-exchange module was reorganized for taking advantage of domain-specific language provided by Cropbox modeling framework [Yun et al., 2020]. The assimilated carbon accumulates and forms a carbon pool (g) ready to be distributed to plant organs. A potential allocation rate of available carbon ($\mathrm{g\,d^{-1}}$) is driven by carbon supply rate from the pool ($\mathrm{g\,d^{-1}}$) excluding maintenance respiration ($\mathrm{g\,d^{-1}}$). After taking account of carbohydrate synthesis efficiency (Y_g), an actual allocation rate ($\mathrm{g\,d^{-1}}$) is determined and split into a set of allocation rates for structural organs according to a partitioning table (Figure 4.1). The partitioning table is a 2-dimensional array where each row represents a developmental stage and column represents a destination. Developmental stages span from seed, vegetative, bulb growth before scape appearance, bulb growth after scape appearance, bulb growth after scape removal, and death. Partitioning destinations include root, leaf, sheath, scape, and bulb. For each time step of simulation, an actual allocation rate weighted by a partitioning coefficient found in the table was used for biomass accumulation of each destination organ.

Dynamic Phyllochron

An interval between leaf appearance, phyllochron, is not necessarily static throughout plant growth, but can dynamically change depending on the growth condition. However, maximum leaf tip appearance rate ($\mathrm{LTAR_{max}}$; $\mathrm{d^{-1}}$) in the original garlic model was determined by thermal time based on storage duration between harvest and planting as well as storage temperature for which seed garlic has been kept during this period. Once initialized, $\mathrm{LTAR_{max}}$ would remain the same until the end of simulation. This assumption was often held when storage duration was close to an average duration where curve fitting was originally done for. However, sometimes the leaf tip appearance rate stayed too high at the end of

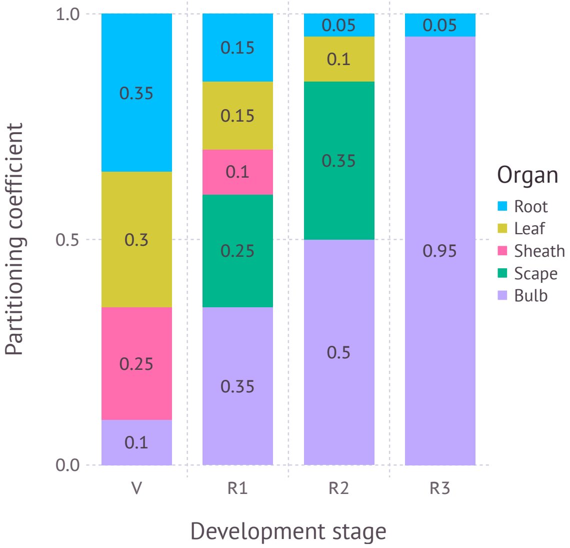

Figure 4.1: Partitioning coefficients for plant organs dynamically adjusted according to development stage. V: vegetative stage; R1: reproductive stage between scape initiation and appearance; R2: reproductive stage between scape appearance and removal; R3: reproductive stage after scape removal. R3 is not used if scape is not removed during simulation.

growing season when storage duration was longer than usual. The opposite would happen when storage duration was too short. In other words, scape appearance in the reproductive stage, which is driven by the same phyllochron assuming a scape would appear after passing three phyllochrons, could become too sensitive to the initial value of $\mathrm{LTAR_{max}}$. To alleviate this issue, $\mathrm{LTAR_{max}}$ was adjusted to converge towards a half of the asymptote of maximum leaf tip appearance rate parameter ($\mathrm{LTAR_{max,a}}$; $\mathrm{d^{-1}}$). After each leaf appearance, $\mathrm{LTAR_{max}}$ would linearly increase or decrease depending on the initial rate and the slope towards the asymptote. Convergence is done when leaf rank k reaches generic leaf number N_g which was set to 10 by default.

$$r_0 = \mathrm{LTAR}_{\mathrm{max,s}} = \frac{\mathrm{LTAR}_{\mathrm{max,a}}}{1 + e^{-k(\mathrm{SD} - \mathrm{SD}_m)}} \tag{4.1}$$

$$r_1 = \frac{\mathrm{LTAR}_{\mathrm{max,a}}}{2} \tag{4.2}$$

$$\mathrm{LTAR}_{\mathrm{max}} = r_0 + (r_1 - r_0)\frac{k}{N_g} \tag{4.3}$$

Cold Stress

Two types of cold stress response commonly found with garlic plants grown in the field during winter season were added to the model: cold injury and cold damage. Cold injury represents impeded leaf growth under below normal air temperatures. Actual leaf elongation rate (LER) is scaled down from potential leaf elongation rate (LER_p) by cold injury effect (E) which is a function of the number of cold days (D) the plant has experienced. We assumed critical temperature where cold injury begins to appear at 0 C and had related factors (a, b) fitted with a dataset obtained from a growth chamber experiment. Namdo (ND) cultivar were planted and grown in pots under room temperature until the third leaf emerged. Plants were then placed in a growth chamber subject to constant temperature of 0 °C, −5 °C, −10 °C and −15 °C, respectively. Each treatment had three replicates and leaf area of the third leaf blade from survived plants was measured for eight days.

$$d = \begin{cases} 1, & T < T_{c,i} \\ -1, & T \geq T_{c,i} \end{cases} \tag{4.4}$$

$$D = \sum d \tag{4.5}$$

$$E = 1 - \frac{\log(a(T - T_{c,i}) + b)}{e^{\frac{1}{D}}} \tag{4.6}$$

$$\mathrm{LER} = E \cdot \mathrm{LER}_p \tag{4.7}$$

Cold damage represents death of the plant under more extreme temperature, resulting into a reduced plant density. Unlike cold injury where leaf growth slows down only under low temperature and recovers once temperature goes back up, cold damage leads to permanent wilting from which the plant cannot recover. Mortality due to cold damage (M) is a logistic curve fitted to the number of plants survived at the end of the experiment under cold treatments.

$$M = \frac{e^{-s(T-T_{c,d})}}{1+e^{-s(T-T_{c,d})}} \tag{4.8}$$

$$S = 1 - M \tag{4.9}$$

$$\mathrm{PD} = S \cdot \mathrm{PD}_0 \tag{4.10}$$

4.2.2 Parameter Calibration

A parameter set for Namdo (ND) cultivar was mostly based on existing parameter sets calibrated for Korean Mountain (KM) and Shantung Purple (SP). Only a few parameters were modified to reflect how ND grows in general compared to the other cultivars. Minimum length of longest leaf ($\mathrm{LL}_{\mathrm{min}}$) was increased to 100 cm which was the largest value found in our datasets. Maximum elongation rate ($\mathrm{LER}_{\mathrm{max}}$) was accordingly adjusted to 5.56 cm d^{-1} assuming full leaf expansion takes 18 days under optimal condition. Initial leaves at harvest (ILN) was set to 6 as found in a dissected seed garlic bulb. Stay green (SG) was set to 1.5 d which was a value calibrated for SP cultivar. Storage temperature (SD) was assumed constant 8 °C during entire storage period. Seed bulb was assumed harvested on June 30th and storage duration (SD) was calculated accordingly. Note that it was our intention to select parameters that allow overestimation of biomass and leaf area for tracking potential growth while calibrating parameters to keep timing of phenology as close as possible to the observation.

We validated our new parameter set for ND cultivar using three datasets. The first dataset (D1) was collected from an experiment plot located at Agricultural Research Center for Climate Change, Jeju, South Korea. ND cultivar was planted on October 8th, 2014 and harvested on June 19th, 2015. Growth and development measurements, such as leaf count, leaf area, biomass for each part, were recorded from mid-vegetative stage until harvest. This dataset was used for evaluating overall response of the ND parameter set we obtained above. The second dataset (D2) was collected from a temperature gradient house located at the same location in Jeju. Temperature gradient house is a glass house equipped with heaters on the one side of wall that keeps a small, but constant gradient in continuous planting zones. Five planting zones were set up with 2 °C to 3 °C of temperature difference kept from end to end. ND cultivar was planted on October 7th, 2014 and harvested on May 17th, 2015. Similar measurements to the first dataset were recorded from early vegetative stage until harvest. This dataset was used for evaluating response of the model to modest temperature changes in a similar way that the model would be subject under future climate conditions. Scape was not removed in both datasets. The last third dataset (D3) was obtained from a farm field located in Jeju, South Korea. ND cultivar was planted on September 9th, 2009 and harvested on June 18th, 2010. Types of recorded variables were the same as other datasets. Scape was assumed to be removed shortly after its appearance out of the whorl. Only the visible portion of scape was cut and measured for biomass. Hourly time-series of weather data for each dataset were obtained from nearby Jeju station (184) operated by Korean Meteorological Administration.

4.2.3 Future Climate Projections

For assessing garlic yield changes in future climate conditions, we specifically chose two locations in South Korea (Figure 4.2). The first site was Gosan, Jeju located in a Southern island with a humid subtropical climate off the Korean peninsula, which is in Zone 9b in terms of USDA Hardiness Zones. Gosan is where Namdo (ND) cultivar is currently grown in a large scale for commercial purpose where stakeholders are interested to see how the cultivar would be performing and if any adjustments in growing practice such as if planting date shifts would be required in the long term. The second site was Chuncheon, Gangwon which is located in the middle of the Korean peninsula with a humid continental climate with cold winter. Chuncheon is in Zone 6b according to USDA Hardiness Zones and the current climate is not favorable for growing a Southern cultivar such as Namdo which has been historically more adapted to warm climate. However, it is not clear whether future climate conditions could allow growing of new crops in a region previously not suited for production. We assumed two RCP (Representative Concentration Pathway) scenarios, RCP4.5 and RCP8.5, for future climate projections [IPCC, 2014]. Daily weather dataset for the two locations under RCP4.5 and RCP8.5 scenarios were obtained from AgClimate data portal [RDA] operated by Rural Development Administration in South Korea. Elevated CO_2 concentrations for RCP scenarios were used accordingly for driving the integrated coupled gas-exchange model. For comparison with current climate conditions of each location, we also obtained 30-years normal weather data from 1980 to 2010 provided by the same data portal. The daily weather dataset was then scaled down to hourly time-series by applying an interpolation method specifically designed for different types of weather variables [Moon et al., 2019]. Elevated CO_2 levels for each year under future scenarios were obtained by linear interpolation between CO_2 abundance projection reported in the Climate System Scenario Tables [IPCC, 2013].

For each location, multiple runs of simulation were executed with combinations of treatments. In the case of future climate projections, 8 time windows from 2020s to 2090s with 10 years interval multiplied by 10 repetitions from different random seed and two RCP scenarios, RCP4.5 and RCP8.5, produced 160 weather datasets in total. Historical weather was organized in a single time window referred to 1980s with 10 random repetitions, leading to 80 weather datasets. Planting date was adjusted from 240th to 350th DOY (day of the year) with 10 days interval, requiring 12 runs for each weather condition. Immediate scape removal after appearance was assumed. Harvest date was set fixed to be May 15th considering practical harvest dates of ND cultivar grown in Jeju. Yield was based on fresh biomass of bulb at the harvest date. In model simulation, fresh biomass was calculated with 85 % moisture content in bulb. Optimal plating date was then determined by finding out a planting date which gives maximum yield for a given year. For the sake of yield comparison between planting dates, years were grouped into three time periods, namely 1980—2010s,

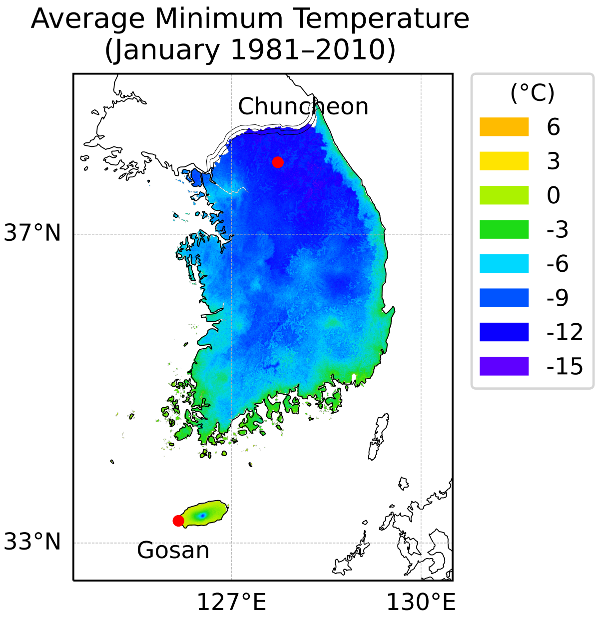

Figure 4.2: Geographic locations of Gosan and Jeju in South Korea. Gosan is located in a Southern island with a humid subtropical climate off the Korean peninsula. Chuncheon is located in the middle of the peninsula with a humid continental climate with cold winter. A color overlay represents average minimum temperature (°C) in January during past 30 years from 1981 to 2010 provided by National Institute of Agricultural Sciences, South Korea. According to USDA Hardiness Zones, Gosan is Zone 9b and Chuncheon is Zone 6b.

2020—2050s, and 2060—2090s.

4.3 Results

4.3.1 Model Validation

Dataset 1 (RICCA field)

Our parameter for ND cultivar was first evaluated with measurements from field grown garlic in dataset D1. Green leaf area from the model exhibited consistent overestimation with an average RMSE (root mean square error) of 443 cm^2 while keeping a similar trajectory of leaf expansion and senescence pattern to the observation (Figure 4.3). The maximum green leaf area was estimated to be 1429 cm^2 on April 27th while the maximum value in the dataset was 1150 cm^2 observed on April 30th. The peak was reached in simulation shortly after scape appeared on April 23rd during early vegetative growth.

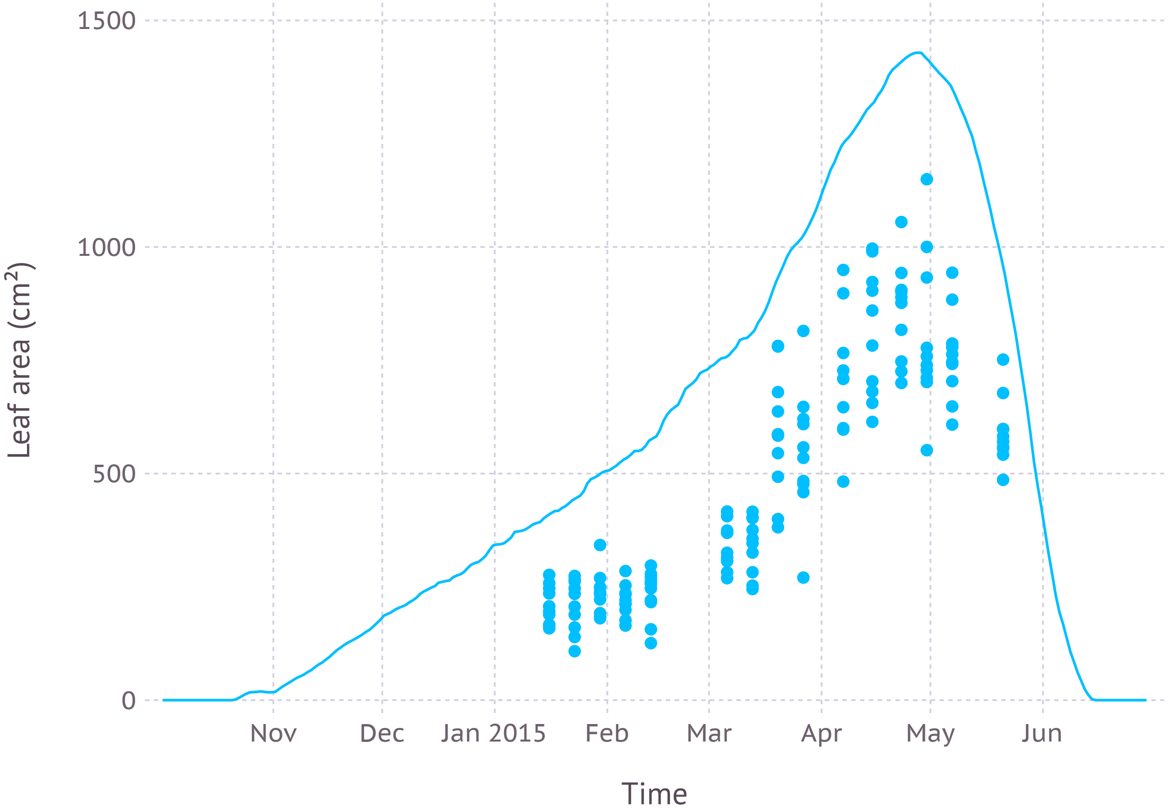

Figure 4.3: Comparison of model simulated green leaf area and observation from dataset D1 which was from field measurements and primarily used for evaluating new parameters.

Simulated biomass allocation to each part of plant structure, namely leaf, bulb, stalk, and scape, was close to the observation with an average RMSE of 5.7 g, 2.6 g, 3.2 g and

6.0 g, respectively (Figure 4.4). The maximum living leaf biomass from simulation was 9.9 g reached on April 27th and the maximum observed value was the same 9.9 g on April 30th. The maximum biomass of bulb from simulation was 23.7 g reached on June 14th while the observed maximum was 26.0 g measured on June 4th which was the final date recorded in the dataset. The maximum biomass of stalk, which consists of leaf sheath and scape, from simulation was 16.0 g close to observed maximum of 15.9 g. However, the timing of peak was shifted by about two weeks later on May 23rd compared to the observed May 7th. Since leaf sheath withered away at the end of growth stage, the only remaining part of living stalk would be scape which was the reason why a convergence between two values occurred in mid-June. Simulated biomass of scape was consistently overestimated and reached its maximum value of 14.2 g on June 20th while observed maximum was 9.5 g on June 4th. Note that the slopes of biomass increase for simulation and observation were almost parallel to each other.

Leaf development phenology simulated by the model was in agreement with fresh leaf count recorded in the dataset with an average RMSE of 1.9 leaves (Figure 4.5). According to the model, leaf initiation was completed on March 22nd with the total number of 16 leaves and the 16th leaf appeared on April 2nd. The final leaf was completely senesced and dropped after about 2.5 months of growth on June 15th.

Dataset 2 (RICCA TCG)

Plants grown in higher temperature zone 1 had larger green leaf area of 1796 cm^2 and reached its peak earlier on April 18th when compared to plants grown in lower temperature zone 5 whose maximum green leaf area was estimated to be 1539 cm^2 reached on May 4th (Figure 4.6). Simulation result was in agreement with observation recorded in dataset D2 in which zone 1 had larger leaf area of $1176 \pm 239\,\mathrm{cm}^2$ on April 17th, in contrast to zone 5 having smaller leaf area of $1124 \pm 90\,\mathrm{cm}^2$ on the same date. After three weeks on May 9th, the difference was flipped over where zone 1 had senesced faster to result in a smaller green leaf area of $512 \pm 56\,\mathrm{cm}^2$ while zone 5 was still greener with $701 \pm 70\,\mathrm{cm}^2$. Mean temperature recorded in dataset D2 for zone 1 was 15.5 °C and zone 5 was 12.6 °C.

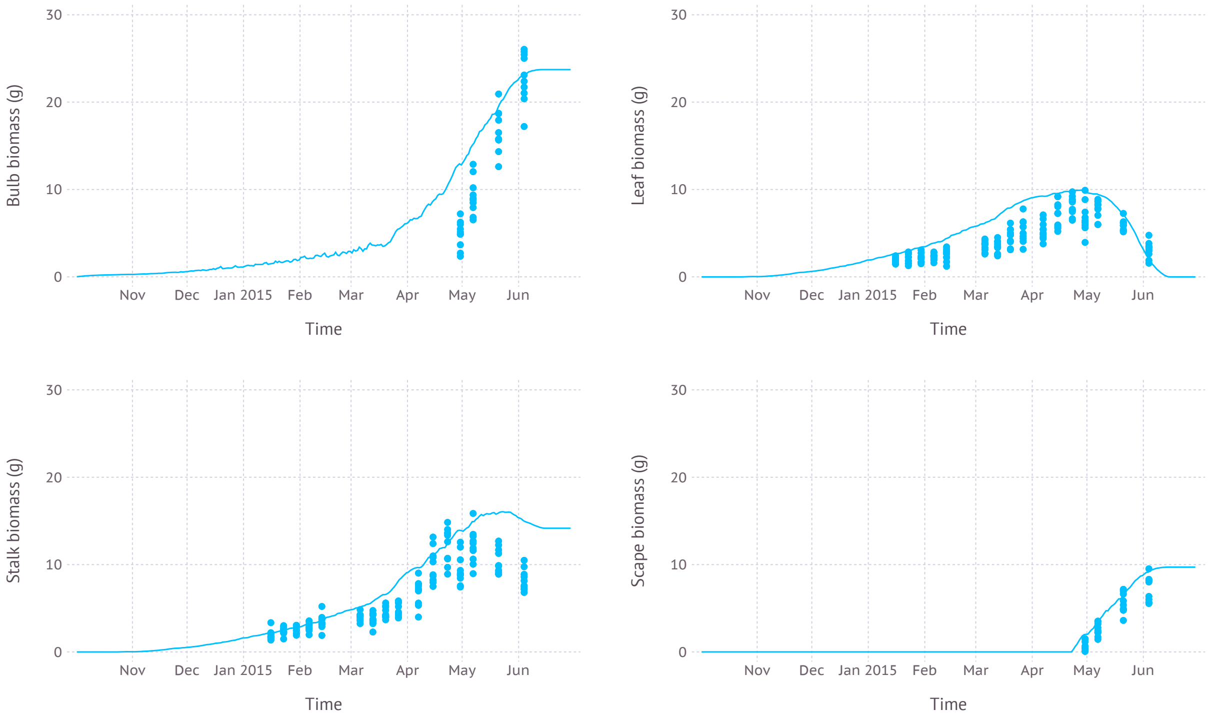

Figure 4.4: Biomass allocation to leaf, bulb, stalk, and visible portion of scape simulated over time compared with measurements from dataset D1 which was from field measurements and primarily used for evaluating new parameters.

Dataset 3 (JS)

Simulated biomass allocation compared with another independent dataset D3 came with an average RMSE of 5.0 g, 8.1 g and 4.2 g for leaf, bulb, and stalk, respectively (Figure 4.7). According to the dataset, scape was removed during reproductive stage, but an exact date of removal was not recorded. We assumed scape removal took place as soon as a tip of the scape became visible out of the whorl which occurred on May 1st by model estimation. The scape biomass at the time of removal was 6.0 g. The maximum living leaf biomass from simulation was 11.8 g reached on May 1st and the maximum observed value was 9.1 g on

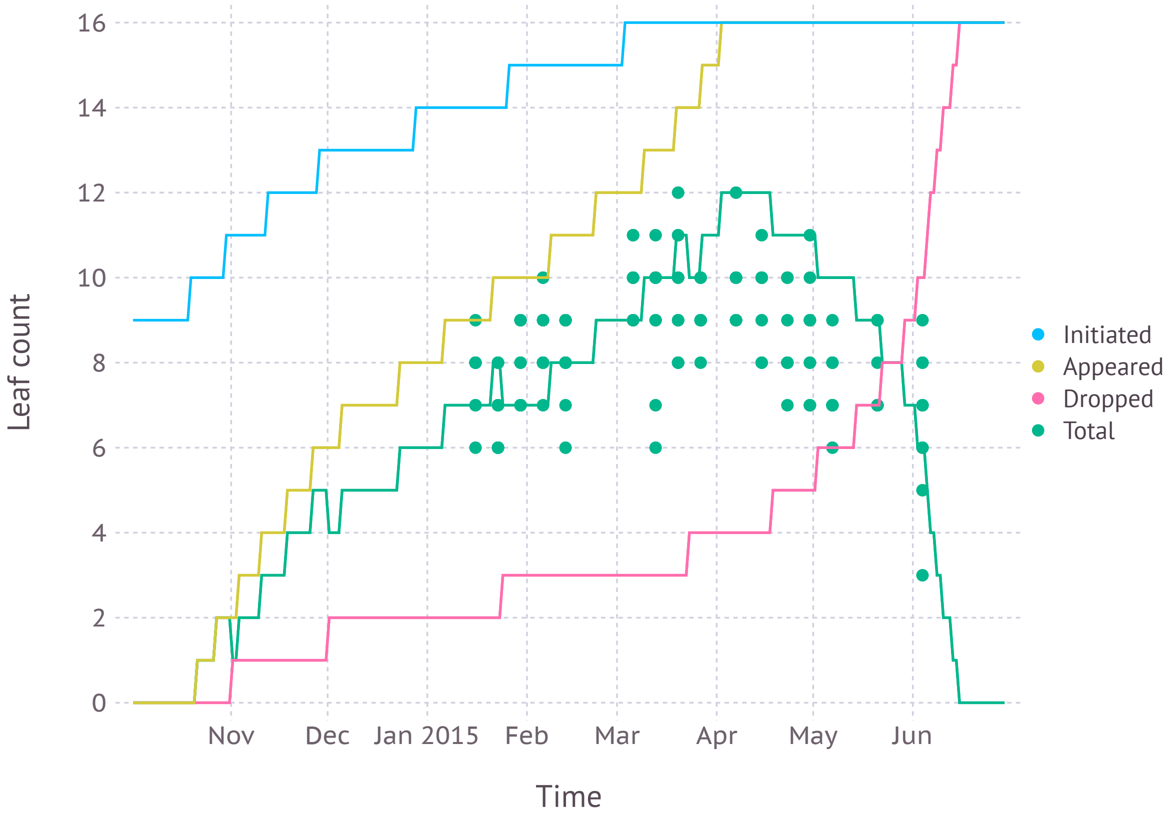

Figure 4.5: Simulated leaf development phenology compared with fresh leaf count recorded in dataset D1 which was from field measurements and primarily used for evaluating new parameters.

April 28th. The maximum bulb biomass from simulation was 39.0 g reached on June 22nd while the observed maximum was 28.7 g measured on May 26th. The maximum biomass of stalk from simulation was 15.3 g on May 1st when scape just appeared and subsequently removed. The maximum stalk biomass recorded in the dataset was 12.3 g observed on April 28th. Once scape was removed and no longer a part of stalk composition, stalk biomass gradually decreased as the mature sheath stopped growing and started senescence.

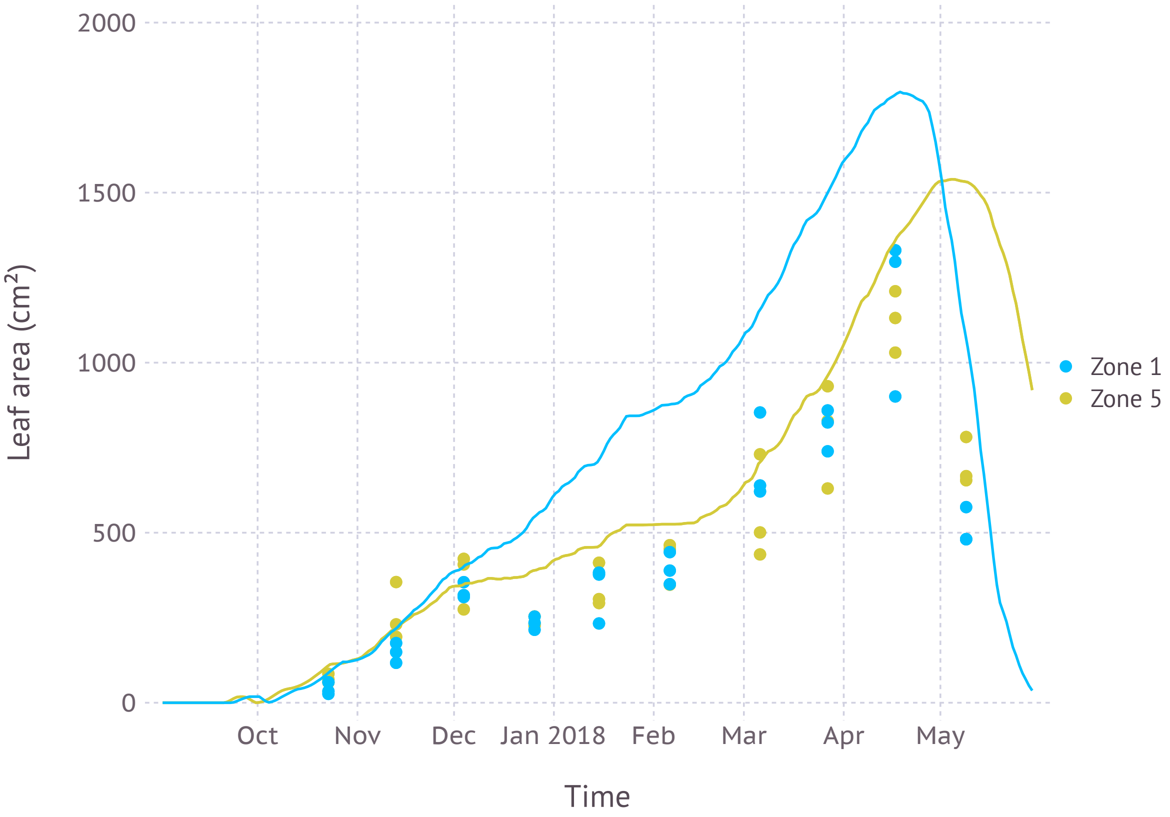

Figure 4.6: Comparison of model simulated green leaf area and observation for two temperature zones (Zone 1: high, Zone 5: low) recorded in dataset D2 from a temperature-controlled glass house.

4.3.2 Yield Projection

Gosan

In the current climate condition, fresh yield on ND cultivar in Gosan, Jeju was estimated to be maximum at an average of 6.8 $\mathrm{kg\,m^{-2}}$ with standard deviation of 0.8 $\mathrm{kg\,m^{-2}}$ when planted in late August (240 DOY) which was closely followed by early September planting (260 DOY) with an average of $6.7 \pm 0.7\,\mathrm{kg\,m^{-2}}$ (Figure 4.8). A similar level of high yield was maintained

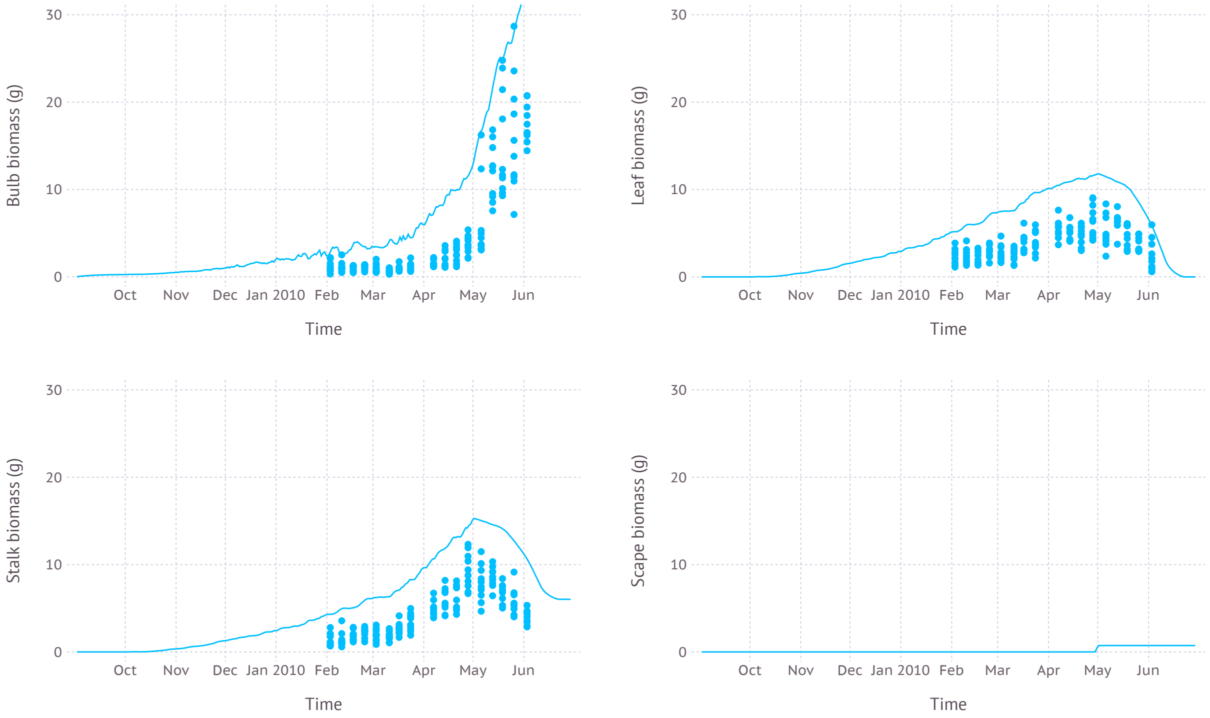

Figure 4.7: Biomass allocation to leaf, bulb, stalk, and visible portion of scape simulated over time compared with measurements from dataset D3 which was from field measurements with scape removal.

until late September then yield gradually decreased with later planting dates. The difference between maximum yield from early planting date and minimum yield from later planting date was $3.7\,\mathrm{kg\,m^{-2}}$. In the near future from 2020s to 2050s, a similar pattern was observed that high yield was achieved with early planting in September. An overall yield was increased to $7.5\pm0.8\,\mathrm{kg\,m^{-2}}$ under RCP4.5 and $7.6\pm0.8\,\mathrm{kg\,m^{-2}}$ under RCP8.5 scenario when compared to the current climate. There was no clear difference between RCP4.5 and RCP8.5 scenarios in terms of estimated yield for a given planting date. In the distant future from 2060s to 2090s, RCP4.5 scenario still maintained a similar pattern where high yield was achieved in early planting dates, but then the range of potential high yield was expanded to later planting dates. For example, planting dates from late August (240 DOY) to mid-October (290 DOY) all resulted in an average yield closely ranged from 7.6 kg m^{-2} to 7.7 kg m^{-2}. The difference between maximum and minimum yield estimated in the range of planting dates was reduced to 3.0 kg m^{-2}. Under RCP8.5 scenario, the yield curve was more flattened that the difference was only 1.8 kg m^{-2} between all planting dates. The maximum yield was 8.3 ± 0.6 kg m^{-2} in early-October (280 DOY).

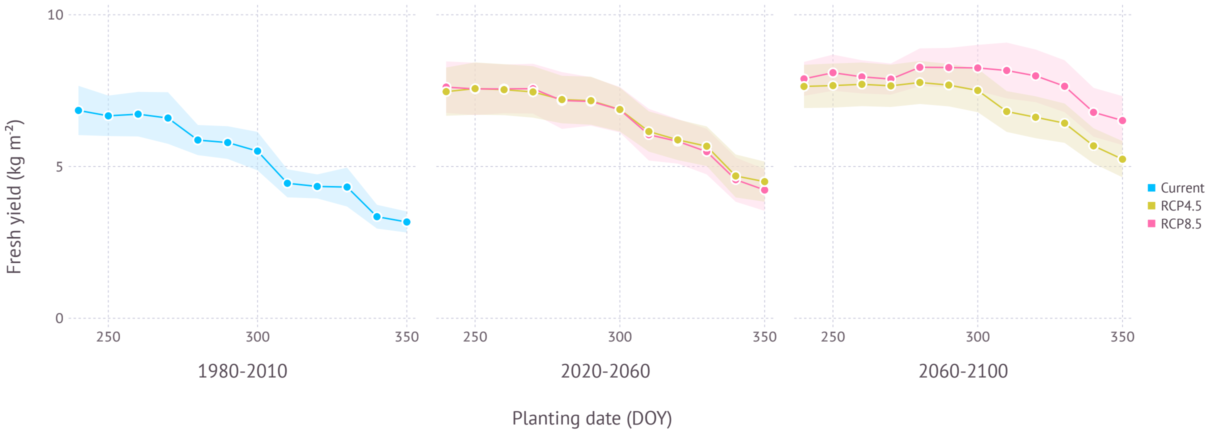

Figure 4.8: Yield estimation within a range of planting dates under current and future climate projection in Gosan, Jeju which is a region grows ND cultivar at commercial scale. Current scenario indicates simulation results with 30-years normal weather data from 1980—2010. Shades represent a range of ±1 standard deviation from mean fresh yield.

When optimal plating dates were assessed from current to future climate conditions by 10 year intervals, a clear trend of shifting towards later planting date was found in the future projection although its strength varied depending on scenarios (Figure 4.9). Both scenarios began with optimal planting date in early to mid-September then showed a strong divergence at the end of the century that the optimal planting date surfaced from late September to early October under RCP4.5 scenario, while mid-November became a possibility under RCP8.5

scenario.

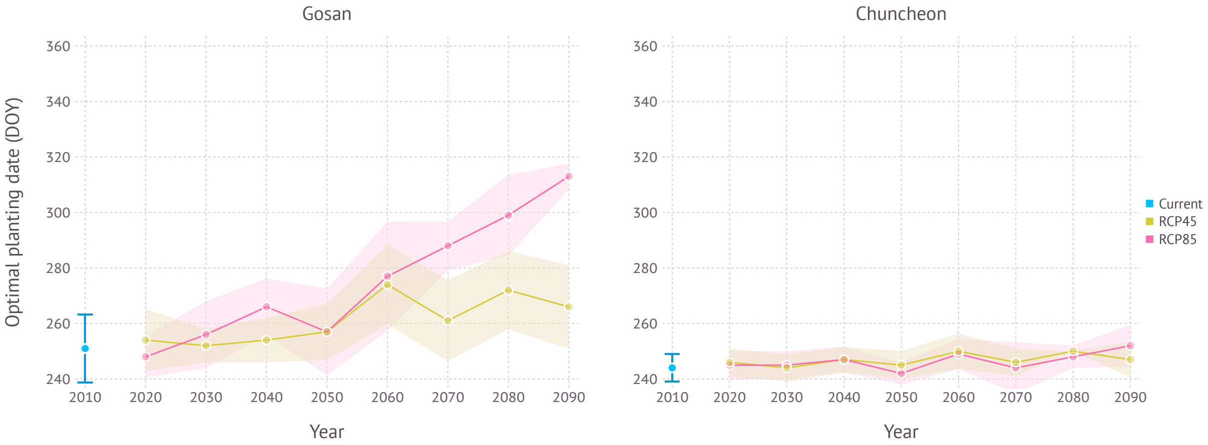

Figure 4.9: Optimal planting dates estimated for each year under current and future climate projections in Gosan and Chuncheon. Year 2010 indicates simulation results with 30-years normal weather data from 1980—2010 representing current climate. For RCP scenarios, each year indicates 10-year average, e.g., 2090 refers to 2090—2100. Error bar and shades represent a range of ±1 standard deviation from mean optimal planting date.

Chuncheon

In the current climate condition, yield of ND cultivar in Chuncheon, Gangwon was estimated close to nil with a maximum yield $0.06 \pm 0.05\,\mathrm{kg\,m^{-2}}$ due to impeded leaf growth and increased mortality from cold winter temperature during early vegetative growth (Figure 4.10). However, under future projections, yield became more viable thanks to warmer climate. In the near future from 2020s to 2050s, maximum estimated yield was $1.5 \pm 0.7\,\mathrm{kg\,m^{-2}}$ under RCP4.5 and $1.3 \pm 0.9\,\mathrm{kg\,m^{-2}}$ under RCP8.5 scenario when both planted in early September (250 DOY). In the distant future from 2060s to 2090s, more yield was achievable with $2.5 \pm 0.8\,\mathrm{kg\,m^{-2}}$ under RCP4.5 and $4.3 \pm 1.1\,\mathrm{kg\,m^{-2}}$ under RCP8.5 scenario with early to mid-September plating dates, 250 DOY and 240 DOY, respectively. The difference between maximum and minimum yield estimated in the range of planting dates was 0.6 $\mathrm{kg\,m^{-2}}$ in early period and 1.0 $\mathrm{kg\,m^{-2}}$ in late period under RCP4.5 scenario. RCP8.5 scenario initially had a similar range of estimated yield over multiple planting dates with 0.5 $\mathrm{kg\,m^{-2}}$ in early period, but then showed much higher variance of 1.7 $\mathrm{kg\,m^{-2}}$ in late period.

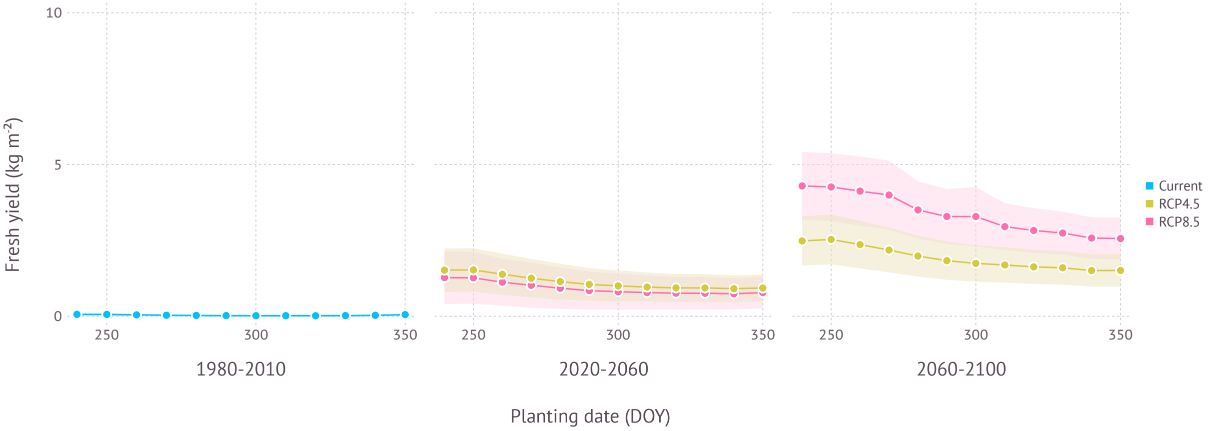

Figure 4.10: Yield estimation within a range of planting dates under current and future climate projection in Chuncheon, Gangwon where current climate is not favorable for growing ND cultivar. Current scenario indicates simulation results with 30-years normal weather data from 1980—2010. Shades represent a range of ±1 standard deviation from mean fresh yield.

In terms of optimal planting dates for each period, planting in around early September consistently turned out to work best regardless of climate scenarios and estimated yield gradually declined with later planting dates in all scenarios (Figure 4.9).

4.4 Discussion

4.4.1 Model Validation

Parameter Calibration

Our parameter set for ND cultivar was mostly derived from existing parameters for Korean Mountain (KM) and Shantung Purple (SP) with small changes. The final parameter set used in our simulation turned out to be similar to one calibrated for SP cultivar. It would not be unexpected given that ND was originated from a Chinese cultivar and hence there is a chance SP might be also related with this original cultivar due to geographical proximity [Kim et al., 2009].

Overestimation

Simulation with the calibrated parameter set often resulted in overestimation in a sense that model output tends to touch upper boundaries of observed data points (Figure 4.3,4.4,4.6,4.7). We consider it reasonable since our model estimates yield potential for a given environmental condition with assuming no limiting factors such as water and nutrient. Some types of overestimation also presumably came from difference between physical measuring methods and modeled algorithms. For example, green leaf area recorded in the dataset was measured by taking only non-withered leaves at the time of observation which is prone to lose leaves with some green parts intact. On the other hand, green leaf area from the model was calculated for individual leaves at a fractional scale by tracking current green portion of the leaf for each time step. These difference could have been one of the reasons leading to overestimation in leaf area simulation (Figure 4.3,4.6).

Temperature Regimes

Evaluation of model response under slightly separate temperature regimes as conducted in temperature gradient house provided an insight how elevated air temperature under RCP scenarios would affect plant growth (Figure 4.6). In short, plant will grow larger and faster and die earlier in warmer conditions. An average of 3 °C difference in temperature led to more than two weeks of shift in growth peak and 15 % change in total green leaf area. Subsequent changes in senescence timing would imply a need for finding out optimal harvest dates which we assumed as a rather constant management decision in our simulation.

Storage Condition

Storage duration (SD) affects maximum leaf tip appearance rate ($\mathrm{LTAR}_{\mathrm{max}}$) via the dynamic phyllochron model (Equation 4.1,4.2,4.3). Storage temperature (ST) along with storage duration then decides number of leaves initiated inside a seed bulb at the time of planting. Despite their importance on phenology, there often exits no record on when seed bulbs were harvested and in which condition they were stored until the date of planting. With controlled experiments on storage condition, we could have better understanding on how leaves are initiated during storage period and whether more sophisticated approaches like a dynamic plastochron would be necessary.

Other Environmental Cues

While our assessment for yield projection under future condition was primarily driven by model response to temperature regimes, there is still room for considering other environmental cues. For instance, we did not have a separate vernalization process in the model, but assumed winter chilling was always at an adequate level for triggering continuous development in the following warm spring. While it worked reasonable well in most cases, some processes like mortality from cold stress could capitalize on this additional cue to make dormant plants less vulnerable to cold damage, for instance. Soil water availability would be another important cue in terms of assessing irrigation requirement under future climate conditions given that garlic plots are often irrigated to prevent water deficiency during reproductive stage.

4.4.2 Yield Projection

Gosan

Jeju, including Gosan, is a region where southern-type garlic cultivars like Namdo (ND) has been grown at commercial scale thanks to warm climate. Northern regions in Korean peninsula often have colder winter which prevents growing southern-type cultivars. Growers instead choose northern-type cultivars for cold hardiness. As southern cultivars have advantage of higher yield and shorter growing season, whether they could be adapted to northern regions has been an important question to many growers and stakeholders. According to our simulation results using a process-based model, ND cultivar would continue growing well with a slightly higher yield (Figure 4.8). The optimal planting date in early September estimated for the current climate condition was indeed close to the current practice held in Jeju. This practice is, however, expected to be delayed in the near future if growers keep trying to maximize yield under both climate scenarios (Figure 4.9). The amount of planting date delay depends on the scenarios and the model estimated that RCP4.5 scenario could see a shift less than a month while RCP8.5 scenario could potentially result in two months of late planting. Note that although optimal planting dates were seemingly changed drastically, yield estimation curve versus planting date was actually getting more flattened and the difference between maximum and minimum yield became smaller in warmer climate conditions. Such changes imply that growers would have more options to choose planting date better suits their own needs. For example, October planting in the future would still promise a yield level close to potential maximum while taking a relatively shorter growing season to help reducing overall cost of labor and resources. High yield does not necessarily lead to high profitability when longer growing season increases overall water demand entailed by higher irrigation cost for compensation [Lobell, 2014]. Looking further in distant future, it was more clear to expect a shift in optimal planting to later dates although yield difference to earlier planting dates was not significant.

Chuncheon

Chuncheon is located in the middle of Korean peninsula and its continental climate frequently experiences below freezing temperature during winter season. Hence only northern-type cultivar adapted to cold climate have been grown in this region. Our simulation results confirmed expected yield for the current climate was almost non-existent as most plants subject to mortality (M) could not survive after episodes of extreme cold. By contrast, future climate conditions were projected to become more favorable in both scenarios so that expecting some tangible yields would be at least feasible (Figure 4.10). Generally early planting dates were favored in terms of optimal yield as similar in the current growing region like Jeju (Figure 4.9). Although the level of estimated yield was still lower when compared to the yield currently obtainable in other established regions, growers may be able to take advantage of this new opportunity for expanding crop portfolio during winter season.

4.4.3 Climate Adaptation

It is important to tease apart an effect of adaptation introduced by planting date shift in the future from an impact of planting date shift in the current condition [Lobell, 2014, Challinor et al., 2018]. According to the result from Gosan, planting date shift in established growing region has little effect on adaptation as evidenced by a similar or smaller range between maximum and minimum yield when comparing current and future climate scenarios (Figure 4.8). Higher estimated yield was a result of increased productivity under more favorable condition primarily due to higher temperature and elevated CO_2, but not from potential phenological changes occurred by planting date shift. In non-established regions like Chuncheon, however, an effect of adaptation increased virtually from zero to a substantial amount when transitioning to new climate condition as evidenced by a rising slope of yield estimation curve (Figure 4.10). In other words, the importance of planting date as a climate adaptation strategy depends on how crops are adapted to the local condition.

Underlying uncertainties of crop models often hinder model driven assessment of climate change adaptation [Rosenzweig et al., 2014, Holzkämper et al., 2015, Corbeels et al., 2018]. We adopted a process-based model with coupled gas-exchange to minimize uncertainties in physiological responses to temperature and CO_2, but there still remain many processes that can use improvements. For instance, water stress response was solely dependent on leaf water potential disconnected with soil water status albeit a less practical implication when garlic plants are generally irrigated to meet high water demand during reproductive stage. Nitrogen response is another important factor that the model currently does not take into account and instead assume non-limiting due to extensive use of fertilizers in practice, but will be critical for assessing an exact cost of production in finding optimal yield.

BIBLIOGRAPHY

Mohamed M A Abdalla, M H Aboul-Nasr, and A K Metwaly. Growth and yield of fifteen garlic ecotypes. *Assiut Journal of Agricultural Sciences*, 36(5):52–65, 2011.

Andrew J. Challinor, Christoph Müller, Senthold Asseng, Chetan Deva, Kathryn Jane Nicklin, Daniel Wallach, Eline Vanuytrecht, Stephen Whitfield, Julian Ramirez-Villegas, and Ann-Kristin Koehler. Improving the use of crop models for risk assessment and climate change adaptation. *Agricultural Systems*, 159:296–306, 2018.

Sungchun Choi and Jangsun Baek. Garlic yields estimation using climate data. *Journal of the Korean Data and Information Science Society*, 27(4):969–977, 2016.

Marc Corbeels, David Berre, Leonard Rusinamhodzi, and Santiago Lopez-Ridaura. Can we use crop modelling for identifying climate change adaptation options? *Agricultural and Forest Meteorology*, 256:46–52, 2018.

Cropbox.jl. `https://github.com/cropbox/Cropbox.jl`.

FAO. FAOSTAT, 2020. URL `http://www.fao.org/faostat/`.

C. Giménez, C.O. Stöckle, E.M. Suárez-Rey, and M. Gallardo. Crop yields and n losses tradeoffs in a garlic–wheat rotation in southern spain. *European Journal of Agronomy*, 73:160–169, 2016.

Diego Gómez, Pablo Salvador, Julia Sanz, and José Luis Casanova. Regional estimation of garlic yield using crop, satellite and climate data in mexico. *Computers and Electronics in Agriculture*, 181:105943, 2021.

Inhye Heo, Won-Tae Kwon, Youngmoon Chun, and Seungho Lee. The impact of temperature rising on the distribution of plant-in case of bamboos and garlics. *Journal of Environmental Impact Assessment*, 15(1):67–78, 2006.

A. Holzkämper, P. Calanca, M. Honti, and J. Fuhrer. Projecting climate change impacts on grain maize based on three different crop model approaches. *Agricultural and Forest Meteorology*, 214:219–230, 2015.

Jennifer Hsiao, Kyungdahm Yun, Kyung Hwan Moon, and Soo-Hyung Kim. A process-based model for leaf development and growth in hardneck garlic (*Allium sativum*). *Annals of Botany*, 124(7):1143–1160, 2019.

IPCC. Climate change 2013: The physical science basis. contribution of working group i to the fifth assessment report of the intergovernmental panel on climate change. Technical report, 2013.

IPCC. Climate change 2014: Synthesis report. contribution of working groups i, ii and iii to the fifth assessment report of the intergovernmental panel on climate change. Technical report, 2014.

Rina Kamenetsky. *Garlic: Botany and Horticulture*, chapter 2, pages 123–172. John Wiley & Sons, Ltd, 2007.

Chun-Hwan Kim, Ki-Cheol Seong, Jin-Soo Lee, Kyung-Hee Kang, Yeong-Cheol Um, and Hyo-Duk Suh. Production of seed garlic by sawing bulbils of southern type garlic in jeju island. *Protected Horticulture and Plant Factory*, 18(1):74–80, 2009.

Soo-Hyung Kim, Jig Han Jeong, and Lloyd L Nackley. Photosynthetic and transpiration responses to light, CO_2, temperature, and leaf senescence in garlic: Analysis and modeling. *Journal of the American Society for Horticultural Science*, 138(2):149–156, 2013.

Ji-Wan Lee, Geun-Ae Park, Hyung-Kyung Joh, Kyo-Ho Lee, Sang-Il Na, Jong-Hwa Park, and Seong-Joon Kim. Analysis of relationship between vegetation indices and crop yield using kompsat (koreamulti-purpose satellite)-2 imagery and field investigation data. *Journal of The Korean Society of Agricultural Engineers*, 53(3):75–82, 2011.

David B. Lobell. Climate change adaptation in crop production: Beware of illusions. *Global Food Security*, 3(2):72–76, 2014.

L.F.M Marcelis, E Heuvelink, and J Goudriaan. Modelling biomass production and yield of horticultural crops: a review. *Scientia Horticulturae*, 74(1):83–111, 1998.

KH Moon, HH Seo, M Shin, EY Song, and S Oh. Generation of hourly weather data using daily data. In *Proceedings of The Korean Society of Agricultural and Forest Meteorology Conference*, pages 195–196, 2019.

Lloyd L Nackley, Jig Han Jeong, Lorence R Oki, and Soo-Hyung Kim. Photosynthetic acclimation, biomass allocation, and water use efficiency of garlic in response to carbon dioxide enrichment and nitrogen fertilization. *Journal of the American Society for Horticultural Science*, 141(4):373–380, 2016.

P Põldma, A Merivee, A Pae, and K Justus. Influence of planting time on the development, yield and quality of garlic (*Allium sativum* l.) in estonia. *Acta Horticulturae*, (688):333–338, 2005.

José Antonio Portela, B Sidoti, G Reybet, C Bellaccomo, and R Astorquizaga. Yield stability of ten garlic (*Allium sativum*) clonal cultivars in northern patagonia, argentina. In *VI International Symposium on Edible Alliaceae 969*, pages 107–112, 2012.

RDA. AgClimate data portal. URL `https://agclimate.epinet.kr`.

R.H. Rizzalli, F.J. Villalobos, and F. Orgaz. Radiation interception, radiation-use efficiency and dry matter partitioning in garlic (*Allium sativum* l.). *European Journal of Agronomy*, 18(1-2):33–43, 2002.

Cynthia Rosenzweig, Joshua Elliott, Delphine Deryng, Alex C. Ruane, Christoph Müller, Almut Arneth, Kenneth J. Boote, Christian Folberth, Michael Glotter, Nikolay Khabarov, Kathleen Neumann, Franziska Piontek, Thomas A. M. Pugh, Erwin Schmid, Elke Stehfest, Hong Yang, and James W. Jones. Assessing agricultural risks of climate change in the 21st century in a global gridded crop model intercomparison. *Proceedings of the National Academy of Sciences*, 111(9):3268–3273, 2014.

Hideaki Takagi. *Onions and allied crops*, volume 3, chapter Garlic *Allium sativum* L., pages 109–157. CRC Press, 1989.

F.J Villalobos, L Testi, R Rizzalli, and F Orgaz. Evapotranspiration and crop coefficients of irrigated garlic (*Allium sativum* l.) in a semi-arid climate. *Agricultural Water Management*, 64(3):233–249, 2004.

Kyungdahm Yun, Dennis Timlin, and Soo-Hyung Kim. Coupled gas-exchange model for c_4 leaves comparing stomatal conductance models. *Plants*, 9(10):1358, 2020.